

**CREEP RESISTANCE AND STRAIN-RATE SENSITIVITY OF  
NANOCRYSTALLINE MATERIALS**

by

PALLAB BARAI

A Thesis submitted to the

Graduate School-New Brunswick

Rutgers, The State University of New Jersey

in partial fulfillment of the requirements

for the degree of

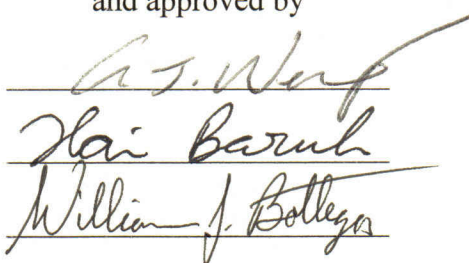
Master of Science

Graduate Program in Mechanical and Aerospace Engineering

written under the direction of

Prof. George J. Weng

and approved by



New Brunswick, New Jersey

[May, 2008]

ABSTRACT OF THE THESIS

CREEP RESISTANCE AND STRAIN-RATE SENSITIVITY OF  
NANOCRYSTALLINE MATERIALS

By PALLAB BARAI

Thesis Director:  
Prof. George J. Weng

A micromechanics-based continuum model is developed to determine the creep resistance and strain-rate sensitivity of the nanocrystalline materials. The solid is idealized as a two (or three) phase composite, where the grains were treated as spherical inclusions, the grain boundary as the matrix and the pores/voids as the third phase (if present in the solid) of the composite. The strain of an individual phase is taken to be the sum of elastic and creep/viscoplastic components. Within the elastic context the homogenization scheme is developed based on the Eshelby-Mori-Tanaka approach. The Laplace transform was used to convert the linear elastic homogenization method to a linear viscoelastic one, and then to convert the viscoelastic response to viscoplastic one, during which the Maxwell viscosity of the viscoelastic phases is replaced by the secant viscosity of the viscoplastic phases. A nonlinear-rate dependent constitutive equation is assumed for both the grain interior and grain boundary to calculate the secant viscosity of the individual phase at a given stage of deformation. The drag stress of the grain interior is assumed to follow the Hall-Petch effect, but that of the grain boundary phase is taken to be size-independent. By using the field-fluctuation method, the effective stress (or effective strain rate) of the constitutive

phase is derived in terms of the applied stress (or applied strain rate). The change in porosity under different loading conditions is also incorporated within the model.

The validity of the model was verified by comparing the predicted stress-strain results with the experimental data of Sanders et al. [42], Wang et al. [43] and Wang et al. [44] for the creep response, and Khan et al. [48] and Khan and Zhang [49] for the constant strain-rate loading. The model is capable of capturing both hardening and softening of material as grain size decreases from coarse grain to the nanometer range. The latter characteristic is also known as the inverse Hall-Petch effect and this occurs in both creep and constant strain-rate response. As a result, the critical grain size at which the solid has maximum strength can be estimated using this method. With the presence of porosity, the developed model is also able to capture the nonlinearity in the stress-strain plot under hydrostatic loading.

## ACKNOWLEDGEMENT

First I would like to acknowledge my advisor Professor George Weng for all his support and collaboration during my research work. I am extremely lucky and feel highly honored to have him as my advisor. He is always willing to give time to his students. I would like to thank him for not only providing the academic advice but also for the financial support that he gave throughout the last two years during my stay at Rutgers.

Next I would like to thank our graduate director Professor Haim Baruh for his dedication to help every international graduate student in any possible way. I also acknowledge him as well as Professor William Bottega for being a member of my M.S dissertation committee and reviewing my work.

Finally, I would like to thank all the faculty, staff, graduate as well as undergraduate students in Mechanical and Aerospace Engineering at Rutgers University for all their collaboration during the past two years.

This investigation was supported by the National Science Foundation, Division of Civil, Mechanical and Manufacturing Innovation (CMMI), Mechanics and Structures of Materials program, under grant CMS 0510409, to study the mechanics of nanocrystalline material.

## DEDICATION

To my parents Jharna Barai and Parimal Barai and my sister Paramita Barai.

## TABLE OF CONTENTS

|   |    |
|---|----|
| Abstract .....  | ii |
| Acknowledgements .....  | iv |
| Dedication .....  | v  |
| Table of contents .....   | vi |
| List of tables .....  | ix |
| List of figures .....   | x  |
| 1. Introduction .....   | 1  |
| 1.1 What is meant by “Nanocrystalline Materials”? .....   | 1  |
| 1.2 Motivation .....  | 3  |
| 1.3 Thesis Outline .....  | 4  |
| 2. Literature review .....  | 6  |
| 2.1 Literature on micromechanics of solids .....  | 6  |
| 2.2 Literature dedicated to nanocrystalline materials .....                                       | 9  |
| 3. Morphology .....   | 14 |
| 3.1 Morphology without porosity .....   | 14 |
| 3.2 Morphology including porosity .....   | 15 |
| 4. Creep response .....   | 18 |
| 4.1 Mechanisms of creep .....   | 19 |
| 4.2 Constitutive equations of the high-temperature creep for the grain interior and<br>GBAZ ..... | 20 |
| 4.3 A homogenization scheme for the time dependent creep of nanocrystalline solids<br>.....       | 24 |

|       |   |    |
|-------|---|----|
| 4.3.1 | The initial elastic state .....   | 24 |
| 4.3.2 | Transition to the viscoelastic state in the Laplace transformed domain                                      | 25 |
| 4.3.3 | From the viscoelastic to the nonlinear state .....  | 27 |
| 4.4   | A field-fluctuation method to find the secant-viscosity of the constituent phases<br>.....                  | 28 |
| 4.5   | Computational procedure to solve the creep problem .....  | 29 |
| 4.6   | Application to nanocrystalline copper, NiP alloy and nickel .....   | 30 |
| 5.    | Strain-rate sensitivity .....   | 43 |
| 5.1   | Mechanism of Hall-Petch effect, inverse Hall-Petch effect and strain-rate<br>hardening .....                | 43 |
| 5.2   | Rate-dependent constitutive relations of the grain interior and GBAZ .....                                  | 47 |
| 5.3   | A homogenization scheme for the viscoplastic response of the 3-phase model                                  | 49 |
| 5.3.1 | The initial elastic state .....   | 50 |
| 5.3.2 | Transition to the viscoelastic state in the Laplace transformed domain                                      | 51 |
| 5.3.3 | Replacement of the Maxwell viscosity by the secant viscosity for the<br>viscoplastic response .....         | 53 |
| 5.4   | A field-fluctuation method to find the secant viscosity of the constituent phases<br>.....                  | 53 |
| 5.5   | Porosity change and the incremental scheme .....  | 55 |
| 5.6   | Application to the rate-dependent behavior of porous nanocrystalline iron, and<br>iron-copper mixture ..... | 57 |
| 6.    | Conclusion and future work .....  | 74 |
| 6.1   | Conclusion .....  | 74 |

|                       |    |
|-----------------------|----|
| 6.2 Future work ..... | 76 |
| Appendix .....        | 78 |
| References .....      | 94 |
| Vita .....            | 99 |

## LIST OF TABLES

|     |   |    |
|-----|---|----|
| 4.1 | Material parameters used in calculation for Cu .....  | 40 |
| 4.2 | Material parameters used in calculation for NiP alloy .....                                   | 41 |
| 4.3 | Material properties for nanocrystalline Ni .....  | 42 |
| 5.1 | Material parameters used in calculations for iron .....                                       | 72 |
| 5.2 | Material parameters used in calculations for Fe <sub>80</sub> Cu <sub>20</sub> material ..... | 73 |

## LIST OF FIGURES

|     |  |    |
|-----|--|----|
| 2.1 | (a) Grain size hardening in the coarse grain and (b) softening in the nanograin range. Note the fourfold increase from the coarse to nanograin size .....  | 9  |
| 3.1 | (a) Morphology of a nanocrystalline metal by molecular dynamic simulation [21].<br>(b) The plastically harder grain interior and the plastically softer GBAZ. (c) The two phase composite model with the grain interior and the GBAZ. .... | 15 |
| 3.2 | The three phase composite model with the grain interior, GBAZ and pores. ...   | 16 |
| 3.3 | Volume fraction of the grain interior and the GBAZ (a) without porosity, (b) with different values of the porosity. ....   | 16 |
| 4.1 | Schematic diagram of a case when creep can occur. ....   | 18 |
| 4.2 | (a) Stress-strain plot in a creep problem, (b) Strain-time plot in a creep problem.  | 18 |
| 4.3 | Comparison between the developed theory and the test data of Sanders et al [40]  | 31 |
| 4.4 | Comparison between the developed theory and the test data of Wang et al. [41]  | 32 |
| 4.5 | Comparison between the developed theory and the test data of Wang et al. [42]  | 32 |
| 4.6 | Grain size hardening and softening of a nanocrystalline copper. ....   | 33 |
| 4.7 | (a) Creep strain and (b) creep resistance of Cu versus the square root of the reciprocal of the grain size at various temperature. ....  | 34 |
| 4.8 | Creep resistance of NiP alloy versus the square root of the reciprocal of the grain size at various temperature. Note that the grain size softening starts at around 35nm for 373K and at around 60 nm for 573K. ....                      | 35 |
| 4.9 | Contributions of the grain interior and GBAZ toward the total strain of the nanocrystalline solid at four grain sizes: (a) larger than $d_c$ , (b) smaller than $d_c$ , (c) one with about equal contributions, and (d) at $d_c$ . ....    | 36 |

|      |   |    |
|------|---|----|
| 4.10 | Dilatational creep of a nanocrystalline solid as a function of (a) elastic property ratio, and (b) grain size strength ratio between the grain interior and GB <sub>AZ</sub> . .....  | 38 |
| 5.1  | Schematic stress-strain plot at (a) constant grain size but different strain rate (b) constant strain rate but different grain size. ....   | 43 |
| 5.2  | Comparison between the experimental and theoretically obtained true stress strain relations under uniaxial compressive loading for nanocrystalline iron with a grain size of 71nm, porosity (f) 3.3% and three different strain rates of 0.0001/s, 0.01/s and 1/s. ....   | 58 |
| 5.3  | Change of the effective secant viscosity and its rate in the course of deformation. The right scale for the viscosity rate is numerically identical to the left one. ....   | 59 |
| 5.4  | Comparison between the experimental and theoretically obtained true stress strain relations under uniaxial compressive loading for nanocrystalline iron at a particular strain rate of 0.001/s with a grain size of 71nm and 96nm along with porosity (f) of 7% and 3.5% respectively. ....   | 60 |
| 5.5  | Comparison between the experimental and theoretically obtained true stress strain relations under uniaxial compressive loading for nanocrystalline Fe <sub>80</sub> Cu <sub>20</sub> with a grain size of 35nm and three different strain rate of 0.0001/s, 0.01/s and 1/s along with different porosity (f) of 11%, 9.6% and 10% respectively. ....                | 61 |
| 5.6  | Change of porosity with strain for the Fe <sub>80</sub> Cu <sub>20</sub> alloy at different strain rates and different initial porosities but a constant grain size. ....   | 62 |
| 5.7  | Comparison between the stress-strain plot of Fe <sub>80</sub> Cu <sub>20</sub> alloy with constant porosity and variable porosity. The plot with variable porosity shows a little bit of strain hardening even after reaching the saturation strength. But the constant porosity curve does not show any strain hardening after reaching the saturation level. .... | 62 |
| 5.8  | (a) Plot of true dilatational stress vs. strain under dilatational constant strain rate (0.01/s) loading for nanocrystalline Fe <sub>80</sub> Cu <sub>20</sub> with a constant grain size of 35nm and different porosities. (b) Plot of true dilatational stress vs. true dilatational strain for Fe <sub>80</sub> Cu <sub>20</sub> alloy                           |    |

|      |  |    |
|------|--|----|
|      | with different elastic modulus for grain interior and GBAZ for a 35nm grain size and 0.01/s strain rate but no porosity. ....  | 64 |
| 5.9  | True stress-strain plot of nanocrystalline Fe <sub>80</sub> Cu <sub>20</sub> under compressive constant strain rate loading of 0.0001/s with a porosity of 5% at different grain size (diameter, d) to demonstrate its potential softening at very small grain size due to increased contribution from the GBAZ. ....  | 65 |
| 5.10 | Hall-Petch plot of nanocrystalline Fe <sub>80</sub> Cu <sub>20</sub> at a constant strain rate loading of 0.0001/s with different porosities of 4%, 5%, 7% and 9%. ....  | 66 |
| 5.11 | Hall-Petch plot for Fe <sub>80</sub> Cu <sub>20</sub> alloy with different elastic modulus for grain interior and GBAZ. Here $E_0$ signifies the Young's modulus of the GBAZ and $E_1$ signifies the Young's modulus of the grain interior region. From the plot it is very clear that the grain size at which the reverse Hall-Petch effect start depends on the difference in the elastic modulus of grain interior and the GBAZ. .... | 67 |
| 5.12 | Three corresponding plots to Fig. 5.2, 5.4, and 5.5 with zero porosity. ....   | 68 |
| 5.13 | Competition between the grain size and porosity for a Fe <sub>80</sub> Cu <sub>20</sub> alloy at a strain rate of 0.01/s. ....   | 69 |
| 5.14 | Competition between the grain size and porosity for iron at a strain rate of 0.01/s. ...   | 69 |
| 5.15 | Reduction in elastic moduli with increasing porosity. A comparison with the experimental data of Fe compacts (Spitzig et. al. [50]) and Fe <sub>80</sub> Cu <sub>20</sub> (Khan and Zhang, [47]). ....   | 70 |
| 5.16 | Comparison of the two theories for a grain size of 71nm without porosity under different strain rates. ....  | 71 |

# Chapter 1

## Introduction

### 1.1 What is meant by “nanocrystalline materials”?

One of the most important and worldwide appreciated insight of the physics and chemistry of solids is that most properties of the solid materials depend on the microstructure (chemical composition and atomic structure) and the size of the solid in any of the three dimensions. A very common example is the difference in hardness of diamond and graphite due to change in the atomic structure of carbon. Comparable changes in the properties of the solids occur when the atomic structure of the solid deviates far from equilibrium or if the size of the solid reduces to a few inter-atomic spacing in one, two or three dimensions. These kind of materials for which the characteristic length of the microstructure is on the order of a few nanometers are characterized as Nanostructured Materials. Based on the microstructural dimensions and properties of nanostructured materials, they can be classified into three categories.

Materials which have particles, fibers or wires, with size in the nanometer range, which are suspended or embedded in a substrate, comprise the first category. The methods used to fabricate these kinds of materials are inert gas condensation, various aerosol techniques, precipitation from vapor and supersaturated liquids or solids. Catalysts, semiconductor devices utilizing single or multi-layer quantum well structures are some examples of nanostructured materials of the first kind.

The second category is comprised of materials and/or devices where the nanometer sized microstructure is embedded on a thin (thickness in nanometer range) surface region of the bulk material. Physical Vapor Deposition (PVD), Chemical Vapor Deposition (CVD), ion implantation and laser beam treatments are some of the common manufacturing techniques for

the modification of the surface of this kind of materials. Examples are surfaces with enhanced corrosion resistance, hardness, wear resistance or protective coatings (such as diamond).

The third category includes bulk solids that have microstructure (atomic arrangement, crystallites or atomic/molecular groups) varying in a length scale of a few nanometers throughout the bulk. This type of material can be divided into two subcategories. The first part consists of materials for which the atomic structure or the chemical composition varies continuously throughout the solid on an atomic scale. Glasses, gels, supersaturated solid solutions fall under this subcategory.

Research about the materials associated with second subcategory of the third category has started in the last two decades only. These materials are assembled of nanometer sized building blocks, mostly crystallites. The atomic structure, crystallography and chemical composition can vary for these building blocks. For crystallite type of building blocks the interfaces can be coherent or incoherent. This means that these kinds of materials are microstructurally heterogeneous, consisting of the building blocks (crystallites or grains) and the inter block region (grain boundaries). It is this inherently heterogeneous structure on a nanometer scale that distinguishes them from glasses and gels and also causes significant deviation in mechanical and thermal properties from the conventional solids. Ball milling and hot processing, powder compaction and electro-deposition are several techniques to fabricate these kinds of nanostructured materials. As these materials have crystallites or grains with size in the nanometer range, they are also known as Nanocrystalline Materials. Now nanocrystalline materials generally refer to the class of materials whose grain sizes are less than 100 nm.

There are several characteristics that can affect the properties of the nanocrystalline materials. If the size of the building blocks (crystallites or grains) is reduced by such an amount so that it is comparable with the critical length scale of physical phenomena (such as the mean free paths of

the electrons or the photons), then the material could show significantly improved mechanical and optical properties. Changes in the atomic structure or other lattice defects (such as dislocations, vacancies) cause a high density of constrained interface, which results in modification of some mechanical properties, even with the same chemical composition. This happens when the diameter of the crystallites or grains become comparable with the thickness of the interface. During the alloying process, sometime the solute atoms segregate in the grain boundary (interface) region to achieve a lower energy level. This can again cause constrained grain boundary regions to modify some of the physical properties.

## 1.2 Motivation

Several experiments with nanocrystalline materials in the last two decades show that they have some superior mechanical properties as compared to conventional materials (grain size in the micrometer range or coarse grained materials). The yield strength of nanocrystalline materials has been observed to be 4-5 times greater than their coarse grained counterpart. As the grain size decreases from coarse grain (diameter in micrometer range) to ultrafine grain (diameter  $> 100nm$ ) and then to fine-grained nanocrystalline materials (diameter  $< 100nm$ ), the yield strength initially increases in proportion to the inverse of the square root of the diameter  $d$  of the grain. This phenomenon is known as the Hall-Petch effect which first appeared in the papers by Hall [18] and Petch [19] in the form as given below,

$$\sigma_y = \sigma_0 + kd^{-\frac{1}{2}} \quad (1.1)$$

where,  $\sigma_0$  and  $k$  are the Hall-Petch constants. Experimental observations as well as Molecular Dynamic Simulations, however, have revealed that as the grain size reduces to very small values (diameter  $< 20nm$ ), the Hall-Petch relation does not hold any more. There exists a critical grain

size ( $d_{crit}$ ) beyond which (diameter  $< d_{crit}$ ), a drop in the yield strength is observed with decreasing grain size and it is known as Inverse Hall Petch effect.

Similarly, nanocrystalline materials can provide better creep resistance than coarse grained ones. Considering the inverse of creep strain to be the creep resistance, a plot similar to Hall-Petch relation can be constructed. In the course of this study it was found that for creep there also exists a critical grain size ( $d_{crit}^{creep}$ ) at which the nanocrystalline material provides maximum creep resistance. It has also been observed that creep can cause more damage to the material at temperatures higher than room temperature. The effect of temperature on the critical grain size ( $d_{crit}^{creep}$ ) at which the maximum creep resistance occurs, has not been investigated yet.

Recently it has been revealed that several processing techniques for nanocrystalline materials like ball milling and hot processing or powder compaction often result in the presence of voids in the final product. Porosity always reduces the elastic stiffness and plastic strength of the nanocrystalline solid. As a result it becomes very important to realize the effect of grain size and porosity on the yield strength of the nanocrystalline material and how they compete with each other. A micromechanics-based continuum model is necessary to clearly understand the effect of both of these parameters (temperature and porosity) on the creep resistance and yield strength of nanocrystalline materials.

### **1.3 Thesis outline**

The first chapter of this thesis is dedicated to the definition of nanocrystalline materials and the motivation behind choosing this topic for research. In Chapter 2 we describe the base of micromechanics and how it eventually evolved to the position where it is today, and some of the works done with nanocrystalline materials previously. Chapter 3 deals with the morphology of the nanocrystalline material. In chapter 4 we study the creep response of the material at different

grain sizes and temperature. The strain-rate response of the nanocrystalline material at different grain sizes and porosity will be discussed in Chapter 5. The last chapter summarizes the work described in this thesis and gives a brief overview of the future research possibilities in this field of nanocrystalline materials.

## Chapter 2

### Literature Review

Being a very new topic of research (approximately two decades old), not many books are available on the mechanics of nanocrystalline materials. Most of the available literature is in the form of journal articles. One of the best review articles dealing with the basic definition and classification of nanostructured and nanocrystalline materials is “Nanostructured Materials: Basic Concepts and Microstructure” by Gleiter [1].

#### 2.1 Literature on micromechanics of solids

To solve the problems at hand the microstructure of the nanocrystalline material has been investigated and a continuum theory has been developed based on the micromechanics of materials. To get acquainted with the micromechanics of solids the book “Micromechanics of Defects in Solids” by Mura [2] is considered to be a very good reference. Complete development of the theory of micromechanics has been discussed there from the very basic definitions to the analysis of crack and dislocations. “Micromechanics: Overall Properties of Heterogeneous Materials”, by Nemat-Nasser and Hori [3], and “Fundamentals of Micromechanics of Solids” by Qu and Cherkaoui [4] are two other additions that deal with the basic aspects of micromechanics of solids.

The review of the literature devoted to micromechanics of solids would always remain incomplete without the mention of Eshelby [5, 6]. His paper “The determination of the elastic field of an ellipsoidal inclusion, and related problems” is considered to be the basis of micromechanics. It is also the most cited paper of the last century in the field of solid mechanics (over 4000 citations). It talks about the elastic field inside an inclusion embedded in an infinite matrix under the condition that, if the surrounding material were absent, the inclusion would have some prescribed homogeneous deformation. The resulting elastic field is obtained by a varied

sequence of imaginary cutting, straining and welding operations. If the inclusion is ellipsoidal in shape the strain inside it is found to be uniform. The second part of the same paper deals with an ellipsoidal region in an infinite medium which has elastic constants different from those of the rest of the material and its effect on the stress field inside the ellipsoidal region under an applied stress at a large distance. The latter one extends the solution obtained in the first one. Determination of the elastic field outside the ellipsoidal inclusion was the main concern in another of his papers [6]. A general method of calculating the biharmonic potential was also described in this article. Eshelby's work was later extended by Hill [7] to nonlinear behavior, by an incremental process, where the internal inhomogeneities of stress and strain in an arbitrarily deformed aggregate of elasto-plastic crystals were evaluated theoretically. The mechanical properties of the aggregate as a whole were estimated using a self-consistent model. This work was continued by Hill [8] where he conducted a rigorous general study of the essential features of heterogeneous elasto-plastic systems. Hashin [9] made a significant amount of contributions in the study of macroscopic mechanical behavior of heterogeneous viscoelastic media. These heterogeneous materials were considered to be mechanical mixtures of several discrete linear viscoelastic phases whose stress-strain relations are assumed to be known. In that article it was also assumed that the specimens of such heterogeneous materials which are significantly larger than the phase regions are statistically homogeneous and isotropic. In 1984 Weng [10], based on Mori Tanaka's concept of average stress in the matrix and Eshelby's solutions of an ellipsoidal inclusion, developed an approximate theory to determine the stress and strain state of constituent phases, stress concentration at the interface, and an elastic energy and overall moduli of the composite. Initially the theory was developed for a general multiphase, anisotropic solid with arbitrarily oriented anisotropic inclusions. Then the explicit solutions were provided for a suspension of uniformly distributed multiphase isotropic spheres in an isotropic matrix.

The main aim of this thesis is to model the nonlinear creep and strain-rate sensitivity of nanocrystalline solids. Here, a review of the work done in these fields, but for coarse grained

materials, is very much appropriate at this position. Talbot and Willis [11] came up with the idea of variational principles of inhomogeneous nonlinear media. They generalized the linear approach developed by Hashin and Shtrikman [12] to a nonlinear one. From a primal problem (corresponding to the minimum energy principle), a dual problem (corresponding to the complementary energy) was derived. The bounds on the elastic moduli that the various problems generated were also discussed. This theory of variational principles was then developed into various versions to study the rate independent composite plasticity by Tandon and Weng [13] and Qiu and Weng [14]. The first one describes an approximate theory to determine the elasto-plastic behavior of particle-reinforced materials where the elastic spherical particles were considered to be uniformly dispersed in the ductile, work-hardening matrix. The concept of secant moduli of the matrix was introduced to characterize Hill's discovery of a decreasing constraint power of the matrix in polycrystal plasticity. The theory was established for both traction and displacement-prescribed boundary conditions, under which, the average stress and strain of the constituents and the effective secant moduli of the composite were explicitly given in terms of the secant moduli of the matrix and the volume fraction of particles. Qiu and Weng [14] introduced an energy criterion to define the effective stress of the ductile matrix. They modified the theory developed by Tandon and Weng [13] to apply it to porous materials which can account for the influence of pore shape as well. This theory possesses the feature of plastic volume expansion under a pure hydrostatic tension. The rate-dependent viscoplastic response was first developed by Li and Weng [15 – 17]. In [15] an approach introducing a linear viscoelastic comparison composite in conjunction with the secant viscosity is proposed for the estimation of the time dependent creep behavior of a two phase viscoplastic composite. The method makes use of a Maxwell matrix in the viscoelastic composite, and sets its shear viscosity equal to the secant viscosity of the viscoplastic matrix at every stage of deformation. The property of the viscoelastic composite is in turn determined from its elastic comparison composite. According to this theory the particles in the composite were taken to be elastic throughout the course of deformation and the effective

stress of the matrix was calculated by the energy approach developed in Qiu and Weng [14]. In [16] a field-fluctuation method was introduced into the secant-viscosity framework to evaluate the homogenized effective stress of the heterogeneously deformed elastic-viscoplastic matrix in an isotropic composite. A theory to incorporate the elastic-viscoplastic behavior of the particles into the overall creep response of the composite material was described in [17]. The theory was based upon the linkage from elasticity to viscoelasticity through the correspondence principle, and then from viscoelasticity to viscoplasticity by means of the concept of secant viscosity and an energy approach. The influence of particle concentration, elastic stiffness, and applied strain-rate on the overall dilatational and deviatoric stress-strain behaviors were examined in detail.

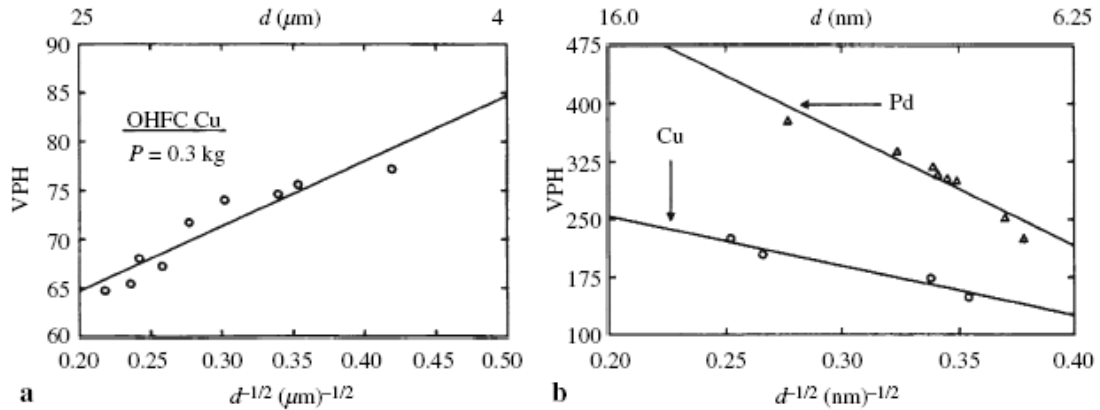


Fig 2.1: (a) Grain size hardening in the coarse grain and (b) softening in the nano-grain range. Note the fourfold increase from the coarse to nano grain size.

## 2.2 Literature dedicated to nanocrystalline materials

The increase in the yield strength (or hardness) of material with decreasing grain size was first discussed by Hall [18] and Petch [19]. An explanation for the variation in the lower yield point of mild steel, with grain size is proposed by Hall [18] in terms of a grain boundary theory. It was also shown that strain-ageing involves two processes: a healing of the grain boundary films, coupled with a hardening in the grains themselves. In continuation to the work of Hall [18], a relationship between cleavage strength and the grain size of the material is developed by Petch [19]. The theory characterizes the dependence of yielding and cleavage on the stress

concentration generated by a slip band across a grain blocked by the grain boundary. In the Hall-Petch plot, that is, the strength versus  $d^{-1/2}$ , the inverse of the square root of grain size, the yield strength tends to scale up linearly in the coarse and ultrafine grain range. But according to Chokshi et al. [20], as the grain size of the solid goes to the lower values in the nanometer scale ( $d < 25\text{nm}$ ), the yield strength starts to decrease at the ambient temperature. Figures 2.1(a) and 2.1(b) show such an increase and decrease of the hardness for Cu and Pd in the coarse and nano-grain range, respectively. Nanocrystalline specimen of Cu and Pd were generated by the inert gas condensation method. The average grain size and their distribution were obtained by transmission electron microscopy, and small angle neutron and X-ray scattering for the nanocrystalline materials. Their hardness was measured by using a Leitz microhardness tester. As the processing technique for the nanocrystalline material was not flawless, the decrease in the hardness at very low grain size was partially attributed to the presence of pores within the material. Later on in the late nineties Sanders et al. [21] developed some sophisticated manufacturing technique to produce flawless nanocrystalline material. Tests in compression of these high density nanocrystalline metals showed high hardness and yield strength values compatible with extrapolation of coarse grained Hall-Petch data to the nanocrystalline regime. Nanocrystalline samples with grain size of 10-110nm and densities of greater than 98% of theoretical value were produced by inert gas condensation and warm compaction by Sanders et al. [22]. They found that the yield strength of the nanocrystalline Cu and Pd was 10-15 times that of annealed, coarse grained metal. Hardness measurements followed the predictions of the Hall-Petch relationship for the coarse grained copper down to 15nm and then plateaued. The tensile strength was also observed to increase with decreasing porosity.

Molecular dynamic simulation of nanocrystalline copper by Schiotz et al. [23] shows a softening with grain size (a reverse Hall-Petch effect) for the smallest grain sizes (3-7nm). Most of the plastic deformation is attributed to a large number of small “sliding” events of atomic

planes at the grain boundaries, with only a minor part being caused by dislocation activity in the grains. The softening at small grain sizes was due to the larger fraction of atoms at the grain boundaries. This softening ultimately imposes a limit on the maximum strength of the nanocrystalline metal. Using their molecular simulation on nanocrystalline nickel, Lund et al. [24] investigated the effect of loading state on mechanical response. At very small grain sizes close to the amorphous limit (2-4nm) a clear strength asymmetry was observed. Specimens turned out to be stronger under uniaxial compression than under uniaxial tension. The simulations also revealed a monotonic trend towards larger strength asymmetry at larger grain sizes, suggesting the existence of a maximum asymmetry in strength at some finite grain sizes.

Idealization of a nanocrystalline material as a composite was first used by Carsley et al. [25]. They presented a model for the strength of nanophase metals which assumes that polycrystalline metals consist of the “bulk” intragranular regions and the grain boundaries. The strength of the boundary phase was taken to be equal to that of the amorphous metal. The crystalline phase was assumed to follow the Hall-Petch relation for the grain size dependence of the strength. The material was treated as a composite with the rule of mixture approach. The theory was able to capture the Hall-Petch hardening for larger grain sizes as well as the grain size softening at very small grain diameter ( $d < 5nm$ ). Wang et al. [26] reviewed the possibility of dislocation mechanism in the deformation process of nanocrystalline materials. They took into account the anisotropic characteristic of crystallographic symmetry and different choices of critical shear strength to obtain a reasonable limit in grain size for applying dislocation pile-up theory to nanocrystalline materials. The deviation from the Hall-Petch relationship was attributed to the small number of dislocation pile-up mechanism. A composite model was used to characterize the strength of the nanocrystalline material. In Carsley et al. [25] and Wang et al. [26] the treatment of two phase composite was based on the mixture rule, that is, they all assumed a uniform stress distribution over the entire continuum. This is clearly not desirable as the grain interior and the

grain boundary zone have different structures and properties, and thus their stress state can not be identical.

In 2003 Jiang and Weng [27 – 29], for the first time, considered the stress strain heterogeneity among the two distinct phases of the composite. In the first one of the three ([27]), a micromechanics-based composite model is developed to calculate the transition of yield stress as the grain size decreases from the coarse grain to the nano grain regime. A generalized self-consistent scheme in conjunction with the secant moduli of the constituent phases and a field-fluctuation approach was used in the development of the theory. The Hall-Petch and the inverse Hall-Petch effect with decreasing grain size were well captured using this theory for high density nanocrystalline copper. To predict the compressive yield strength of nano-grained ceramics, as the grain size decreases from the coarse grained to the nanometer scale, a theory is developed in [28] by using the micromechanics based composite model. The effect of porosity was also considered in this derivation. A direct self-consistent approach was used to determine the strain of the pores. The effect of porosity in the determination of the compressive yield stress was also investigated. In [29] a linear comparison composite is used to determine the nonlinear behavior of a nanocrystalline polycrystal through the concept of secant moduli. The plastic flow of each grain is calculated from its crystallographic slips, but the plastic behavior of the grain-boundary phase is modeled as that of an amorphous material. The presence of a critical grain size at which the material attains maximum yield strength was again verified by the application of this theory.

The work of Jiang and Weng was continued by Capolungo et al. [30] where they developed a self consistent scheme to describe the behavior of nanocrystalline F.C.C materials. The material was approximated as a two phase composite with the inclusion phase representing the grain cores and the matrix representing both grain boundaries and triple junctions. The dislocation glide mechanism was incorporated in the constitutive law of the inclusion phase while a thermally activated mechanism accounting for the penetration of dislocations in the grain boundaries were incorporated in the constitutive law of the matrix phase. The stress strain relation predicted by

this theory was compared with various experimental data. A homogenization scheme was developed by Capolungo et al. [31] for modeling the breakdown of the Hall-Petch plot for nanocrystalline materials. The solid was modeled as a composite as done by Jiang and Weng. The deformation of the inclusion phase was assumed to have a viscoplastic component to take into account the effect of dislocation glide mechanism and Coble creep. The boundary phase was modeled as an amorphous material with perfect elastic-plastic behavior. Results predicted by this theory were compared with some experimental data as well.

Most of the work discussed till now used a rate-independent constitutive relation for the analysis of the plastic behavior of the composite. Later on Li and Weng [32] came up with a secant viscosity composite model to address the strain rate sensitivity of the nanocrystalline solids. A rate dependent constitutive relation was developed to obtain the secant viscosity of the constituent phases along with a field-fluctuation approach. The drag stress of the grain interior (inclusion) was assumed to follow the Hall-Petch relation, but that of the grain boundary affected zone (GBAZ) was taken to be independent of the grain size. The stress-strain results under different strain-rate conditions predicted by this theory were compared with the experimental data of nanocrystalline nickel.

## Chapter 3

### Morphology

#### 3.1 Morphology without porosity

While the molecular dynamic simulation has given the morphology of Fig 3.1(a) [23], the image of scanning transmission electron microscopy has led to a model depicted in Fig 3.1(b) [33]. This model has a grain boundary affected zone (GBAZ) that penetrates into the crystalline grain interior for about 7-10 atomic spacing, and thus is wider than the grain boundary thickness alone. The characteristic of the GBAZ is that, as compared to the grain interior, it is plastically softer. This region can now be interpreted as a combination of the more disordered grain boundary and the penetrated portion of the grain and thus itself is a composite. We shall adopt this broader view and treat GBAZ simply as one phase (with a smeared property of the two), and the grain interior as another. To develop an analytical model for the nanocrystalline solid this composite is conceptually represented in Fig 3.1(c), where the plastically softer GBAZ is taken to be the matrix and the plastically harder grain interior as inclusions. These two phases will be denoted as phase 0 and phase 1, respectively with the volume concentrations  $c_0$  and  $c_1$ . The isotropic phase 1 now stands for the averaged behavior of the anisotropic grains depicted in Fig 3.1(a). At a given grain size  $d$  and GBAZ thickness  $t$ , the volume concentration of the grain interior and the GBAZ can be approximated by,

$$c_1 = \left( \frac{d-t}{d} \right)^3, \quad \text{and} \quad c_0 = 1 - c_1. \quad (3.1)$$

This formula has been derived by analyzing the geometry and taking the ratio of the volume of the spherical grain and the grain with GBAZ region.

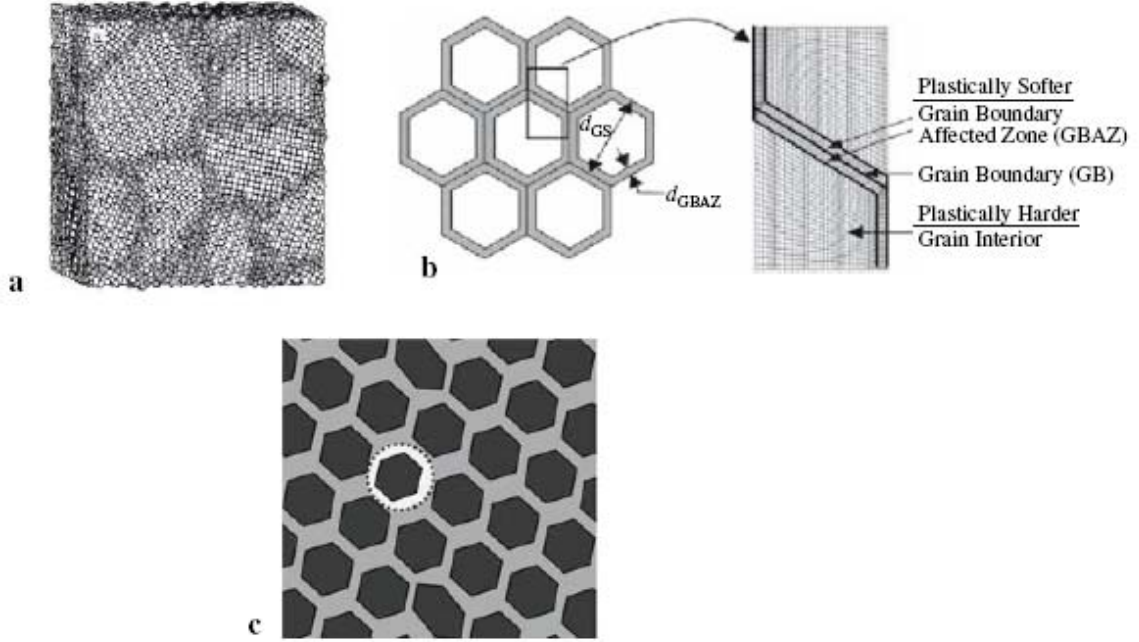


Fig 3.1: (a) Morphology of a nanocrystalline metal by molecular dynamic simulation [21]. (b) The plastically harder grain interior and the plastically softer GBAZ [31]. (c) The two phase composite model with the grain interior and the GBAZ.

### 3.2 Morphology including porosity

When porosity is included within the composite, the conceptual three phase composite model as depicted in Fig 3.2 is considered. The matrix phase, to be denoted as phase 0, represents the plastically softer GBAZ, the dark inclusions, to be denoted as phase 1, represents the plastically harder grain interior, and the small white open regions, to be denoted as phase 2 represent voids. Similar to the case without porosity the isotropic phase 1 stands for the collected or averaged behavior of the anisotropic grains. Since most voids tend to exist at the triple junction points, it is appropriate to consider them to be embedded in the GBAZ as well. This arrangement allows us to invoke some well established homogenization theory to treat this heterogeneous problem. At a given grain size  $d$ , GBAZ thickness  $t$ , and porosity  $c_2$ , the volume concentration of the grain interior and the GBAZ will be calculated respectively from,

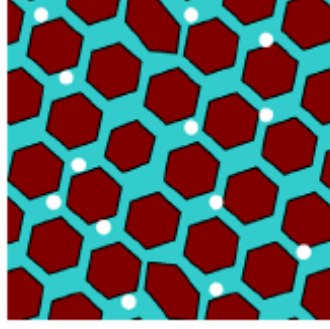


Fig 3.2: The three phase composite model with the grain interior, GBAZ and pores.

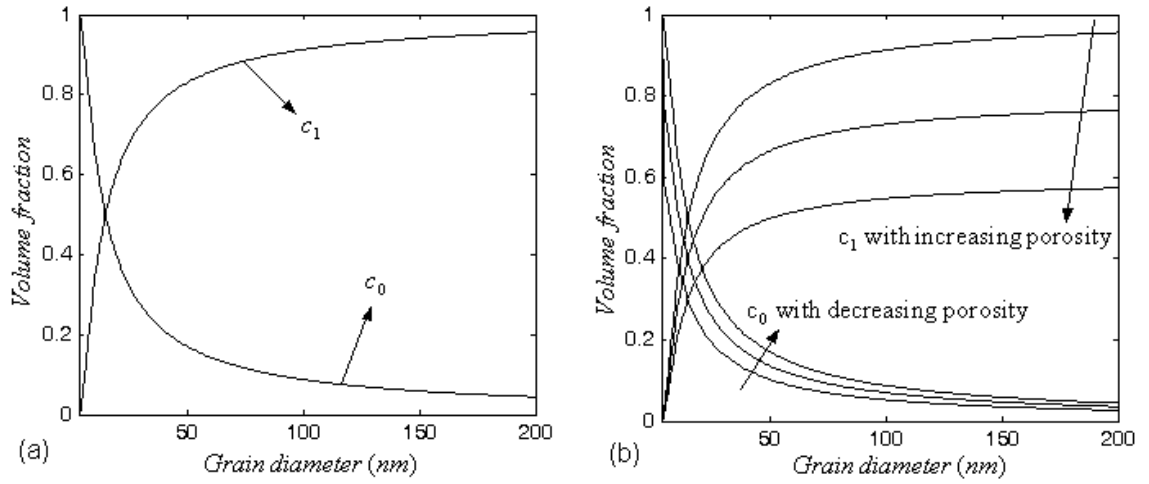


Fig 3.3: Volume fraction of the grain interior and the GBAZ (a) without porosity, (b) with different values of the porosity.

$$c_1 = \left( \frac{d-t}{d} \right)^3 (1 - c_2), \text{ and } c_0 = 1 - c_1 - c_2. \quad (3.2)$$

The derivation of this equation is almost similar to that of equation (3.1), but the effect of porosity is incorporated within this one.

For nickel, the grain-boundary affected zone was observed to span over 7-10 lattice parameters from the atomically sharp grain boundary [33]. With a lattice constant of 0.352 nm, the thickness  $t$  is about 2.5 to 3.5 nm. For the case without porosity, taking  $t = 3$  nm and grain size

of  $d = 30$  nm, the volume concentration of GBZ is about 27%. Including the porosity, considering  $t = 3$  nm, grain size of  $d = 30$  nm, and porosity of 5% into calculation, the volume concentration of GBZ is about 25%. Fig 3.3(a) and 3.3(b) describes how the volume fraction varies with changing grain diameter without and with the presence of porosity, respectively.

In the nanocrystalline regime, all three phases have non-negligible volume concentration, and since both pores and GBZ are softer than the grain interior, their presence is expected to have a significant impact on the overall response of the porous, nanocrystalline material. It is also evident that, without as well as with porosity, in a microcrystalline material, say  $d = 10\mu m$ , the GBZ is negligible. But in an ultrafine crystalline material, say  $d = 300nm$ , it still occupies 3% of the total concentration (without porosity). Since GBZ is a plastically softer phase and it serves as the matrix, such a low concentration can still have a non-negligible effect on the overall response.

## Chapter 4

### Creep Response

Creep is described as the tendency of solid materials to deform slowly but permanently to relieve stresses. It occurs when a solid material is exposed to some stress for a long time even though the stress is below the yield strength of that material. Creep deformation can cause material failure at high temperature (close to the melting point of the material). This kind of creep deformation has been observed in metals, ceramics, glasses and polymers. Mathematically creep occurs when the boundary condition is specified by constant stress,  $\sigma = \text{const.}$  Fig 4.1 shows a typical case where creep can occur, even though  $\sigma < \sigma_{\text{yield}}$ . A typical stress vs. strain ( $\sigma - \varepsilon$ ) and strain vs. time ( $\varepsilon - t$ ) plot is given in Fig 4.2(a) and 4.2(b).

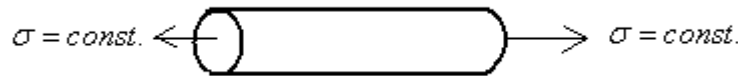


Fig 4.1: Schematic diagram of a case when creep can occur.

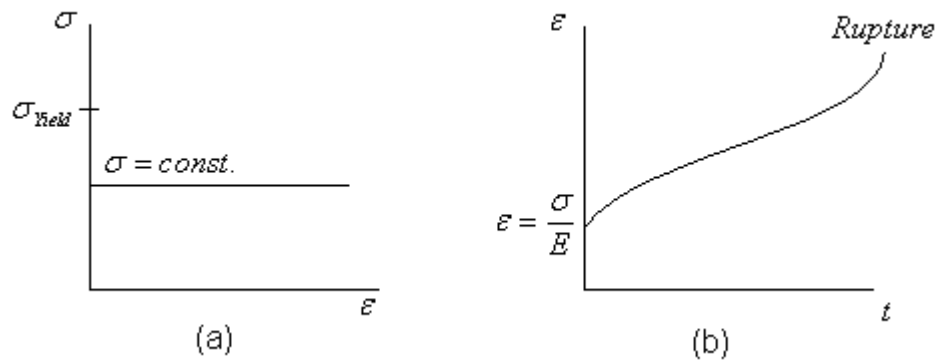


Fig 4.2 (a) Stress-strain plot in a creep problem, (b) Strain-time plot in a creep problem.

#### 4.1 Mechanisms of creep

There are several mechanisms that govern the creep of metals. At high stress level the movements of dislocations play a major roll in the creep deformation of the solid. The defects and disorders that are usually present in the crystals act as an obstacle to the movement of dislocations. But at high temperature (close to the melting point of the material) or high stress level (above some threshold value) the vacancies in the crystal can diffuse to the position of dislocations and cause the dislocation to move to the adjacent slip plane. By climbing to adjacent slip planes the dislocations can overcome the obstacles to their motion which results in further creep deformation of the material. This is known as dislocation creep and it has a very high dependence on the applied stress and temperature. In this study we are concerned with creep deformation of metals under high stress for structural applications, and the major creep mechanism is this one.

There are two other mechanisms of creep which are controlled by diffusion of atoms at low stress level. One of them is the diffusion of atoms within the crystal (or grain). This Nabarro-Herring creep has weak stress dependence and a moderate dependence on the grain size. But this creep mechanism becomes extremely dominant at very high temperature (close to the melting point of the material). Because, at higher temperature, the atoms gain more energy to move from one lattice to the available vacancy at the neighboring lattice. Also the possibility of having a vacancy at the neighboring lattice increases with increasing temperature.

The other diffusion controlled creep mechanism is known as Coble creep. It occurs due to the diffusion of atoms in the grain boundary region. It has low dependence on the applied stress and very high dependence on the grain size. So for nanocrystalline material Coble creep is expected to dominate the creep mechanism at low stress and low temperature. With increasing temperature the grain boundary diffusion increases, but the vacancies at the GB remain almost constant. So

this creep mechanics has less dependence on increasing temperature as compared to the Nabarro-Herring creep mechanism.

#### 4.2 Constitutive equations of high-temperature creep for the grain interior and GBAZ

The creep property of a solid is measured by the amount of creep strain that it generates under a given stress and temperature. This is a time-dependent process and, for a nanocrystalline material, the overall strain is contributed by both the grain interior and GBAZ. Due to the plastically softer response of the GBAZ and the harder one of grain interior, there is a continuous exchange of stress distribution, but their weighted mean must give rise to the externally applied one. Since the elastic moduli of both phases are not necessarily equal, the overall inelastic strain cannot be calculated by the simple weighted mean of those of the constituent phases. This is part of the essential structures that was disclosed by Hill [8]. Instead, it is the total strain, which contains both the elastic and creep components, that is given by the weighted mean. But before we proceed to evaluate the development of the overall strain, it is necessary to specify the constitutive equations for both phases so that their creep rate at a given level of stress and temperature, and creep strain (due to strain hardening) can be evaluated. Then, if under a given external stress,  $\bar{\sigma}_{ij}$  (an overbar signifies that it is a volume averaged quantity), the internal stresses,  $\bar{\sigma}_{ij}^{(1)}$  and  $\bar{\sigma}_{ij}^{(0)}$ , of the grain interior and GBAZ can be determined, the creep rates of both phases will follow.

Within the small strain range we assume the total strain rate to be the sum of the elastic and creep rates for each phase, as well as for the overall composite. It follows that, for the GBAZ and grain interior

$$\dot{\epsilon}_{ij}^{(r)} = \dot{\epsilon}_{ij}^{e(r)} + \dot{\epsilon}_{ij}^{c(r)}, \quad r = 0, 1, \quad (4.1)$$

and for the overall nanocrystalline solid

$$\dot{\bar{\epsilon}}_{ij} = \dot{\bar{\epsilon}}_{ij}^e + \dot{\bar{\epsilon}}_{ij}^c. \quad (4.2)$$

Since  $\dot{\bar{\epsilon}}_{ij} = c_1 \dot{\bar{\epsilon}}_{ij}^{(1)} + c_0 \dot{\bar{\epsilon}}_{ij}^{(0)}$  and  $\bar{\sigma}_{ij} = c_1 \bar{\sigma}_{ij}^{(1)} + c_0 \bar{\sigma}_{ij}^{(0)}$ , it is easy to see that  $\dot{\bar{\epsilon}}_{ij}^c = c_1 \dot{\bar{\epsilon}}_{ij}^{c(1)} + c_0 \dot{\bar{\epsilon}}_{ij}^{c(0)}$  holds only when both constituent phases have identical elastic moduli. The overall time-dependent strain therefore must be calculated from the weighted mean of the total constituent strains.

For each constituent phase the elastic part depends on its stress through the usual isotropic relations, whereas the creep rate is taken to follow the power law and Arrhenius function. The effective creep rate  $\dot{\epsilon}_e^c$  then can be written in terms of the effective stress  $\sigma_e$  and temperature  $T$ , as

$$\dot{\epsilon}_e^c = \dot{\epsilon}_0^c \cdot \left( \frac{\sigma_e}{s} \right)^n \cdot \exp(-Q/RT). \quad (4.3)$$

Here  $\dot{\epsilon}_0^c$  is a reference creep rate that can be set arbitrarily (it will be set as  $5 \cdot 10^{-4} / s$  in later calculations),  $s$  is the drag stress that represents the current state of hardening, and  $n$  the stress exponent which generally lies between 3 to 5 for the dislocation climb-plus-glide mechanism [34]. In addition,  $Q$  is the activation energy and  $R$  the universal gas constant. The effective stress and creep strain rate are defined as usual by

$$\sigma_e = \left( \frac{3}{2} \sigma'_{ij} \sigma'_{ij} \right)^{1/2}, \quad \dot{\epsilon}_e^c = \left( \frac{2}{3} \dot{\epsilon}_{ij}^c \dot{\epsilon}_{ij}^c \right)^{1/2}, \quad (4.4)$$

in terms of the deviatoric stress  $\sigma'_{ij}$ , and their components are governed by the Prandtl-Reuss relation

$$\dot{\epsilon}_{ij}^c = \frac{3}{2} \frac{\dot{\epsilon}_e^c}{\sigma_e} \sigma'_{ij}. \quad (4.5)$$

Due to strain hardening the drag stress will increase in the course of deformation. Its rate is controlled by both strain hardening and dynamic recovery and can be set in the form

$$\dot{s} = h \cdot \left(1 - \frac{s}{s_*}\right) \dot{\epsilon}_e^c, \quad (4.6)$$

so that, upon integration, it yields

$$s = s_* - (s_* - s_0) e^{-\frac{\epsilon_e^c}{s_*/h}}. \quad (4.7)$$

Here parameter  $s_0$  represents the initial hardening state and  $s_*$  the final saturation state. So there are five key material constants for each phase: the stress exponent  $n$ , the hardening coefficient  $h$ , the initial strength  $s_0$ , the saturation strength  $s_*$ , and the activation energy  $Q$ .

The strength of grain interior is grain-size dependent. When dislocation mechanisms operate inside the grains, such dependence can be described by the Hall-Petch relation [18, 19]. This relation is often attributed to the existence of both statistically stored dislocations and geometrically necessary ones [35], as well as to dislocation pile-ups [36]. Thus for phase 1, the grain interior, we may write

$$s_0^{(1)} = s_0^\infty + kd^{-1/2}, \quad s_*^{(1)} = a s_0^{(1)}. \quad (4.8)$$

So it's two constants  $s_0^{(1)}$  and  $s_*^{(1)}$  are now replaced by the three,  $s_0^\infty$ ,  $k$  and  $a$ , to reflect its grain-size dependence. But if the grain size decreases to some critical value, dislocation mechanisms will cease to operate and there would be no more strain-hardening. Such critical grain sizes were found to be about 8.2 nm for copper and 11.6 nm for palladium [26]. In our calculations we will take  $s_0^{(1)}$  and  $s_*^{(1)}$  to continue to increase with decreasing  $d$  before such a critical grain size is reached (which will be taken to be 10 nm), and then set them to remain constant with further

decrease of  $d$ . For GBAZ, its initial and saturation strength are grain-size independent and can be simply denoted as  $s_0^{(0)}$  and  $s_*^{(0)}$ .

To make connection with the concept of secant viscosity that we will later use, it is useful to write eq. (4.3) in terms of the secant viscosity  $\eta_r^s$  for the  $r$ -th phase, as

$$\dot{\epsilon}_{ij}^{c(r)} = \frac{1}{2\eta_r^s} \sigma_{ij}'^{(r)}, \text{ or } \dot{\epsilon}_e^{c(r)} = \frac{1}{3\eta_r^s} \sigma_e^{(r)}. \quad (4.9)$$

It follows that, for the grain interior and GBAZ, we have

$$\eta_1^s = \frac{s^{(g)}}{3\dot{\epsilon}_0^c} \cdot \left( \frac{s^{(g)}}{\sigma_e^{(g)}} \right)^{n-1} \cdot \exp(Q^{(g)} / RT), \quad (4.10a)$$

$$\eta_0^s = \frac{s^{(gb)}}{3\dot{\epsilon}_0^c} \cdot \left( \frac{s^{(gb)}}{\sigma_e^{(gb)}} \right)^{n-1} \cdot \exp(Q^{(gb)} / RT), \quad (4.10b)$$

respectively. Since the drag stress  $s$  increases with creep strain, the secant viscosity will continue to increase during the creep process. Moreover, as  $s$  scales with  $d^{-1/2}$  for the grain interior a smaller grain size will also result in a higher viscosity. A higher temperature on the other hand will lower the viscosity. Most of the constitutive relations shown in this section are previously derived which are available in any text book related to plasticity. Equations (4.10a and b) were derived using eqs. (4.3), (4.5) and (4.9).

The above constitutive equations govern the deviatoric response of the constituent phases. Their dilatational response is taken to be incompressible and thus solely governed by the elastic bulk modulus. It must be kept in mind that, even though both phases are incompressible, the nanocrystalline solid as a whole can still be compressible, that is, it can still undergo a time-dependent creep under a pure hydrostatic stress.

### 4.3 A homogenization scheme for the time-dependent creep of nanocrystalline solids

Creep behavior of grain and GBAZ are time-dependent and nonlinear. A homogenization procedure is described to calculate the development of creep strain of the nanocrystalline solid. The objective is to develop an explicit, analytical model that can account for the contributions from both phases, and their interactions. To keep the model explicit and analytical, the analysis of this time-dependent, nonlinear viscosity problem is performed first and with the aid of a time-dependent, linear viscosity problem with a Maxwell-type phase, and then with the Maxwell viscosity replaced by the secant viscosity of the grain interior and GBAZ. The linear viscosity problem, in retrospect, follows from the elastic one through the correspondence principle [9].

This is an approach based on the concept of a linear comparison composite for the study of a nonlinear one. Since its inception by Talbot and Willis [11], this approach has been developed into various versions to study the rate-independent composite plasticity [13, 14]. For the rate-dependent viscoplastic response it was first developed by Li and Weng [15 – 17] through the concept of secant viscosity. This procedure starts with the selection of an elastic model which has an identical microgeometry to the problem at hand. As the evaluation of the four partial derivatives in the field-fluctuation method is rather involved (see eq. (4.27), on page 29), it is imperative that the elastic model be simple and explicit. For the inclusion/matrix microgeometry as sketched in Fig.3.1(c), both the Mori-Tanaka (M-T) method and the generalized self-consistent scheme [37] can be called upon, but the latter would lead to a substantially more complicated state for the four partial derivatives. For this reason the M-T model is selected here.

#### 4.3.1 The initial elastic state

In the 2-phase composite the elastic bulk and shear moduli of the  $r$ -th phase will be denoted by  $\kappa_r$  and  $\mu_r$ , respectively, and its volume concentration by  $c_r$ . The effective bulk and shear moduli of the composite are given by [10].

$$\kappa = \kappa_0 \left[ 1 + \frac{c_1(\kappa_1 - \kappa_0)}{c_0\alpha_0(\kappa_1 - \kappa_0) + \kappa_0} \right], \quad \mu = \mu_0 \left[ 1 + \frac{c_1(\mu_1 - \mu_0)}{c_0\beta_0(\mu_1 - \mu_0) + \mu_0} \right], \quad (4.11)$$

where,

$$\alpha_0 = \frac{(1 + \nu_0)}{3(1 - \nu_0)} = \frac{3\kappa_0}{3\kappa_0 + 4\mu_0}, \quad \beta_0 = \frac{2(4 - 5\nu_0)}{15(1 - \nu_0)} = \frac{6}{5} \frac{\kappa_0 + 2\mu_0}{3\kappa_0 + 4\mu_0}, \quad (4.12)$$

and  $\nu_0$  is the Poisson's ratio of the matrix (GBAZ). For later calculation of the initial elastic response and evaluation of the constituent strains it is useful to record the average hydrostatic and deviatoric stresses of the constituent phases in terms of the applied stress  $\bar{\sigma}_{ij}$ , as

$$\begin{aligned} \sigma_{kk}^{(1)} &= \frac{\kappa_1}{(c_1 + c_0\alpha_0)(\kappa_1 - \kappa_0) + \kappa_0} \bar{\sigma}_{kk}, \quad \sigma_{ij}^{'(1)} = \frac{\mu_1}{(c_1 + c_0\beta_0)(\mu_1 - \mu_0) + \mu_0} \bar{\sigma}_{ij}'; \\ \sigma_{kk}^{(0)} &= \frac{\alpha_0(\kappa_1 - \kappa_0) + \kappa_0}{(c_1 + c_0\alpha_0)(\kappa_1 - \kappa_0) + \kappa_0} \bar{\sigma}_{kk}, \quad \sigma_{ij}^{'(0)} = \frac{\beta_0(\mu_1 - \mu_0) + \mu_0}{(c_1 + c_0\beta_0)(\mu_1 - \mu_0) + \mu_0} \bar{\sigma}_{ij}'. \end{aligned} \quad (4.13)$$

The corresponding elastic strains follow directly from these stresses through their respective elastic moduli.

#### 4.3.2 Transition to the viscoelastic state in the Laplace transformed domain

The linear viscoelastic behavior of a constituent phase can be written in terms of its stress and strain relation in the Laplace, transformed domain. Denoting such fields by a hat (^), and the corresponding moduli with the superscripts “TD”, we have

$$\hat{\sigma}_{kk}^{(r)} = 3\kappa_r^{TD} \hat{\varepsilon}_{kk}^{(r)}, \quad \hat{\sigma}_{ij}^{'(r)} = 2\mu_r^{TD} \hat{\varepsilon}_{ij}^{'(r)}, \quad r = 0, 1. \quad (4.14)$$

Likewise for the composite, we write

$$\hat{\bar{\sigma}}_{kk} = 3\kappa^{TD} \hat{\bar{\varepsilon}}_{kk}, \quad \hat{\bar{\sigma}}_{ij}' = 2\mu^{TD} \hat{\bar{\varepsilon}}_{ij}'. \quad (4.15)$$

Then by analogy to eq. (4.11), and taking  $\kappa_r^{TD} = \kappa_r$  due to plastic incompressibility, we have

$$\kappa^{TD} = \kappa_0 \left[ 1 + \frac{c_1(\kappa_1 - \kappa_0)}{c_0 \alpha_0^{TD} (\kappa_1 - \kappa_0) + \kappa_0} \right], \quad \mu^{TD} = \mu_0^{TD} \left[ 1 + \frac{c_1(\mu_1 - \mu_0^{TD})}{c_0 \beta_0^{TD} (\mu_1 - \mu_0^{TD}) + \mu_0^{TD}} \right], \quad (4.16)$$

where  $\alpha_0^{TD}$  and  $\beta_0^{TD}$  follow from eq. (4.12)

$$\alpha_0^{TD} = \frac{3\kappa_0}{3\kappa_0 + 4\mu_0^{TD}}, \quad \beta_0^{TD} = \frac{6}{5} \frac{\kappa_0 + 2\mu_0^{TD}}{3\kappa_0 + 4\mu_0^{TD}}. \quad (4.17)$$

In view of the decomposition of strain rate in eq. (4.1), the simplest linear model is the Maxwell element, with a shear viscosity  $\eta_r$  for the  $r$ -th phase. It follows that

$$\mu_r^{TD} = \frac{\mu_r s}{s + T_r}, \quad \text{with} \quad T_r = \frac{\mu_r}{\eta_r}, r = 0, 1. \quad (4.18)$$

For creep under a constant stress,  $\hat{\bar{\sigma}}_{ij} = \bar{\sigma}_{ij} / s$ , where  $s$  is the Laplace parameter (this  $s$  is used as the Laplace parameter in this section only and it should not be confused with the drag stress which is also denoted by  $s$  in other sections). The creep strain  $\bar{\varepsilon}_{ij}(t)$  then can be derived from the Laplace inverse of  $\hat{\bar{\varepsilon}}_{ij}$ , which follows from eqs. (4.15) and (4.16). After some lengthy algebra, we arrive at the overall dilatational and deviatoric strains

$$\bar{\varepsilon}_{kk}(t) = \frac{1}{3\kappa_0} \cdot \frac{y_3}{y_1} \left[ 1 + A + \frac{B}{y_1} \exp\left(-\frac{y_2}{y_1} t\right) \right] \bar{\sigma}_{kk}, \quad (4.19a)$$

$$\bar{\varepsilon}_{ij}'(t) = \frac{1}{2\mu_0} \left[ C + D \cdot t + p \exp(-rt) \left( \cos(wt) + \frac{q-r}{w} \sin(wt) \right) \right] \bar{\sigma}_{ij}'. \quad (4.19b)$$

Here,  $A = y_1 y_4 / y_2 y_3 - 1$ ,  $B = y_1 A$ ,  $C = (d_3 d_7 - d_4 d_6) / d_7^2$ , and  $D = d_4 / d_7$ , and constants

$y_1, y_2, y_3, \dots$  are listed in Appendix A1. They all depend on the viscosities  $\eta_1$  and  $\eta_0$ .

#### 4.3.3. From the linear viscoelastic to the nonlinear state

Due to the continuous change of secant viscosity, an incremental scheme needs to be adopted. The extension from the creep of a linear viscoelastic composite to the nonlinear, time-dependent, one can then be carried out with the constant replacement of Maxwell viscosities,  $\eta_1$  and  $\eta_0$ , by the corresponding secant viscosities  $\eta_1^s$  and  $\eta_0^s$  in eq. (4.10). To this end eqs. (4.19a) and (4.19b) are recast in the rate form, as

$$\dot{\bar{\epsilon}}_{kk} = \frac{1}{3\kappa_0} \cdot \frac{y_3 b_1}{y_1^2} \cdot \exp\left(-\frac{y_2}{y_1} t\right) \bar{\sigma}_{kk}, \quad (4.20a)$$

$$\dot{\bar{\epsilon}}_{ij}' = \frac{1}{2\mu_0} \left[ D + p(-r) \exp(-rt) \left( \cos(wt) + \frac{q-r}{w} \sin(wt) \right) + \right. \\ \left. + p \exp(-rt) \{ -w \sin(wt) + (q-r) \cos(wt) \} \right] \bar{\sigma}_{ij}'. \quad (4.20b)$$

This rate equation in turn introduces the effective secant bulk and shear viscosities of the composite  $\eta_\kappa^s$  and  $\eta_\mu^s$ , through

$$\bar{\sigma}_{kk}(t) = 3\eta_\kappa^s(t) \dot{\bar{\epsilon}}_{kk}, \quad \bar{\sigma}_{ij}'(t) = 2\eta_\mu^s(t) \dot{\bar{\epsilon}}_{ij}', \quad (4.21)$$

such that

$$\frac{1}{\eta_\kappa^s(t)} = \frac{1}{\kappa_0} \cdot \frac{y_3 b_1}{y_1^2} \left[ \exp\left(-\frac{y_2}{y_1} t\right) \right], \quad (4.22a)$$

$$\frac{1}{\eta_\mu^s(t)} = \frac{1}{\mu_0} \left[ D + p(-r) \exp(-rt) \left( \cos(wt) + \frac{q-r}{w} \sin(wt) \right) + \right. \\ \left. + p \exp(-rt) \{ -w \sin(wt) + (q-r) \cos(wt) \} \right]. \quad (4.22b)$$

Once these effective secant viscosities are known, the overall creep rate would follow, and evolution of the creep strain of the nanocrystalline solid can be determined incrementally.

The secant viscosities  $\eta_r^s$  that enter into the constants in eqs. (4.22a) and (4.22b), however, are yet unknown. The issue now is the determination of these viscosities. To this end we turn to a field-fluctuation approach.

#### 4.4 A field-fluctuation method to find the secant viscosity of the constituent phases

In view of eqs. (4.10a) and (4.10b), the secant viscosities  $\eta_1^s$  and  $\eta_0^s$  are seen to depend on the effective stress  $\sigma_e$  and the drag stress  $s$ , which further depend on the effective creep strain  $\varepsilon_e^c$  that comes from the integration of creep rate  $\dot{\varepsilon}_e^c$  which, in retrospect, is a function of  $\sigma_e$ . The task boils down to the determination of  $\sigma_e$  for both the grain interior and GBAZ. This can be best achieved by the application of the field-fluctuation method.

This method has a wide range of applicability in the study of heterogeneous materials. Its novelty lies in the fact that, under the same boundary condition, a change in a material constant of a particular phase will result in a change of the overall energy that is solely dependent on this particular change. This approach was first proposed by Bobeth and Diener [38] and Kreher and Pompe [39] for an elastic composite, and later it has been extended to a rate-independent elastoplastic problem by Suquet [40] and Hu [41]. For a rate-dependent problem it was first outlined by Li and Weng [16].

For the present problem the relevant energy term is the overall work rate, which can be expressed as

$$\dot{U} = \bar{\sigma}_{ij} \dot{\varepsilon}_{ij} = \frac{1}{9\eta_\kappa^s} (\bar{\sigma}_{kk})^2 + \frac{1}{3\eta_\mu^s} \bar{\sigma}_e^2. \quad (4.23)$$

On the other it can also be considered as the sum of the work rates of the grain interior and GBAZ, as

$$\dot{U} = c_1(\dot{U}_1^e + \dot{U}_1^c) + c_0(\dot{U}_0^e + \dot{U}_0^c), \quad (4.24)$$

where the superscripts “e” and “c” stand for the elastic and creep components, respectively. The elastic component for each phase can be written readily through its elastic moduli, whereas the creep term is defined through its secant viscosity, as

$$\dot{U}_1^c = \frac{1}{3\eta_1^s} \cdot (\sigma_e^{(1)})^2, \quad \dot{U}_0^c = \frac{1}{3\eta_0^s} \cdot (\sigma_e^{(0)})^2. \quad (4.25)$$

Now setting eq. (4.23) equal to eq. (4.24), we have the identity

$$c_1[\dot{U}_1^e + \frac{1}{3\eta_1^s} \cdot (\sigma_e^{(1)})^2] + c_0[\dot{U}_0^e + \frac{1}{3\eta_0^s} \cdot (\sigma_e^{(0)})^2] = \frac{1}{9\eta_\kappa^s} (\bar{\sigma}_{kk})^2 + \frac{1}{3\eta_\mu^s} \bar{\sigma}_e^2. \quad (4.26)$$

This setting has the desired feature that the sought-after  $\sigma_e^{(1)}$  and  $\sigma_e^{(0)}$  appear side-by-side with the corresponding viscosities  $\eta_1^s$  and  $\eta_0^s$ . A partial derivative with respect to  $\eta_1^s$  and  $\eta_0^s$  (better yet, with respect to  $1/\eta_1^s$  and  $1/\eta_0^s$ ) will then result in the expression of  $\sigma_e^{(1)}$  and  $\sigma_e^{(0)}$ . After carrying out such a derivative, and noting that  $1/\eta_r^s = T_r / \mu_r$ , we arrive at

$$\sigma_e^{(r)2} = \frac{\mu_r}{c_r} \left[ \frac{\partial}{\partial T_r} \left( \frac{1}{\eta_\mu^s} \right) \cdot \bar{\sigma}_e^2 + \frac{\partial}{\partial T_r} \left( \frac{1}{\eta_\kappa^s} \right) \cdot \frac{\bar{\sigma}_{kk}^2}{3} \right], \quad r = 0, 1. \quad (4.27)$$

There are four partial derivatives here. Their explicit evaluations are given in Appendix A2.

These effective stresses serve to determine the secant viscosities  $\eta_1^s$  and  $\eta_0^s$  by eq. (4.10a) and (4.10b) and other related constitutive equations. This completes the development of the theory.

#### 4.5 Computational procedure to solve the creep problem

Description of the incremental computational procedure is provided here. At time  $t = 0$ , the elastic response gives a step jump in the value of total strain. The creep strain is considered to be

zero at that moment. For the first step the effective creep strain rate is calculated from eq. (4.3). Here the effective stress is taken from eq. (4.4) and the drag stress is taken to be the initial value,  $s_0^{(r)}$ . The secant viscosities of the individual phases are also computed from eqs. (4.10a) and (4.10b) using the same value of drag stress. Then the increment in strain follows from eqs. (4.20a) and (4.20b), and the evolution of overall strain after the time increment  $\Delta t$  is computed as

$$\bar{\varepsilon}_{ij}(t + \Delta t) = \bar{\varepsilon}_{ij}(t) + \dot{\bar{\varepsilon}}_{ij}(t) \cdot \Delta t. \quad (4.28)$$

For the subsequent steps, the effective stresses of individual phases are obtained from eq. (4.27). Here the required secant viscosities of the individual phases are taken from the previous step. The drag stress for the current time step is obtained from eq. (4.7) which uses the value of creep strain obtained until the previous step. Then the creep strain rate is again calculated from eq. (4.3) to give the creep strain at the current time step which can be used in the subsequent steps. The secant viscosities for individual phases are computed from eqs. (4.10a) and (4.10b). Then these values are again used in eqs. (4.20a) and (4.20b) to find the strain rate for the current time step. Equation (4.28) provides the true strain at the present time step. This procedure is continued until the entire creep curve is obtained.

#### **4.6 Application to nanocrystalline copper, NiP alloy and nickel**

In order to place the developed theory in proper perspective, it is applied to study the creep resistance of nanocrystalline Cu, NiP alloy, and Ni. These three materials have been tested by Sanders et al. [42], Wang et al. [43], and Wang et al. [44], respectively. The material constants used in the computation are listed in Tables 4.1, 4.2 and 4.3 (given at the end of the chapter). Based on the observation that GBAZ spans over about 7-10 atomic spacing, we take the thickness of GBAZ to be  $t = 3$  nm (the lattice constant of Ni is 0.352 nm and that of Cu is 0.361 nm). The reduction of Young's modulus with increasing temperature is taken to follow,

$$E(T) = E_{RT} [1 - \alpha_T (T - T_{RT})], \quad (4.29)$$

for each phase, where the subscripts “ $RT$ ” stand for room temperature, and  $\alpha_T$  is the reduction coefficient which is also listed in the tables 4.1, 4.2 and 4.3 given at the end of this chapter.

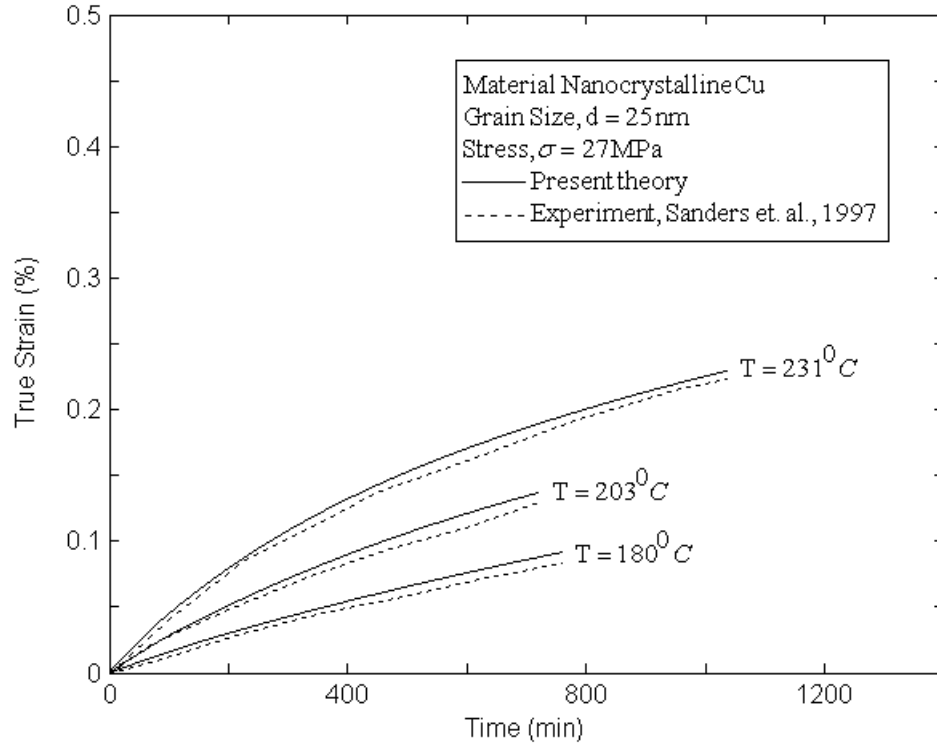


Fig 4.3: Comparison between the developed theory and the test data of Sanders et. al. [42].

The calculated creep curves along with the test data of Cu are shown in Fig. 4.3 at the grain size of  $d = 25$  nm. It is apparent that its creep deformation is greatly enhanced by temperature. For the NiP alloy, the creep curves at  $T = 573$  K are given in Fig. 4.4, for the grain sizes of  $d = 257$  nm and 28 nm. It suggests that there is a grain-size softening when  $d$  reduces from 257 nm to 28 nm. Fig. 4.5 shows the comparison between the theory and experiment of Ni at three stress levels for  $d = 20$  nm. The overall close agreement displayed in these three figures suggests that the developed micro continuum model could capture the essential features of the temperature,

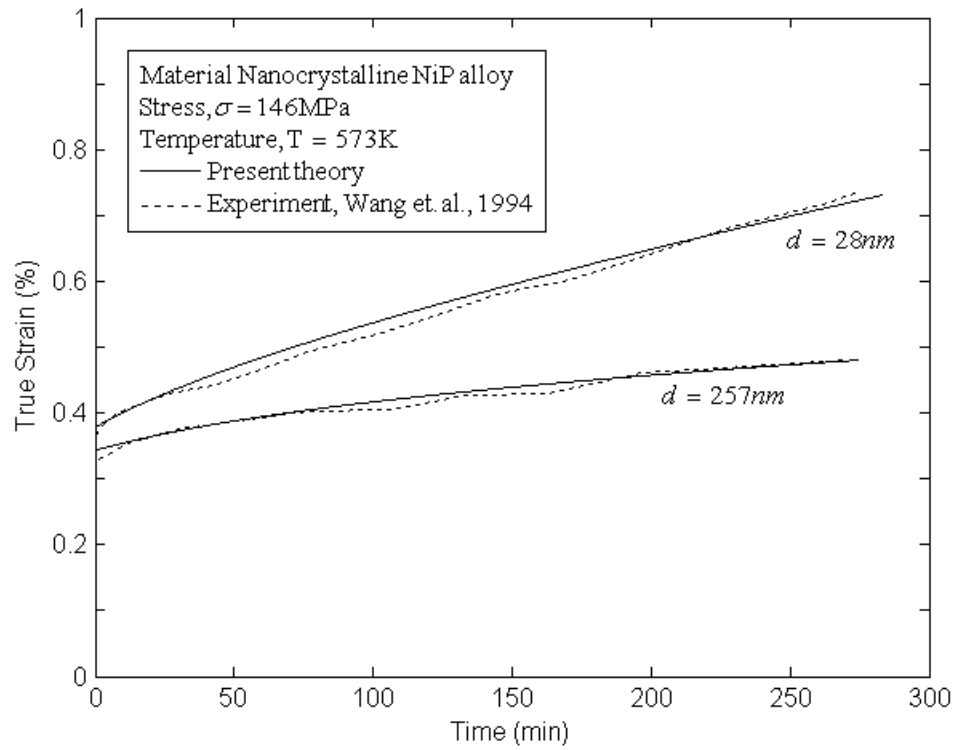


Fig. 4.4: Comparison between the developed theory and the test data of Wang et al. [43].

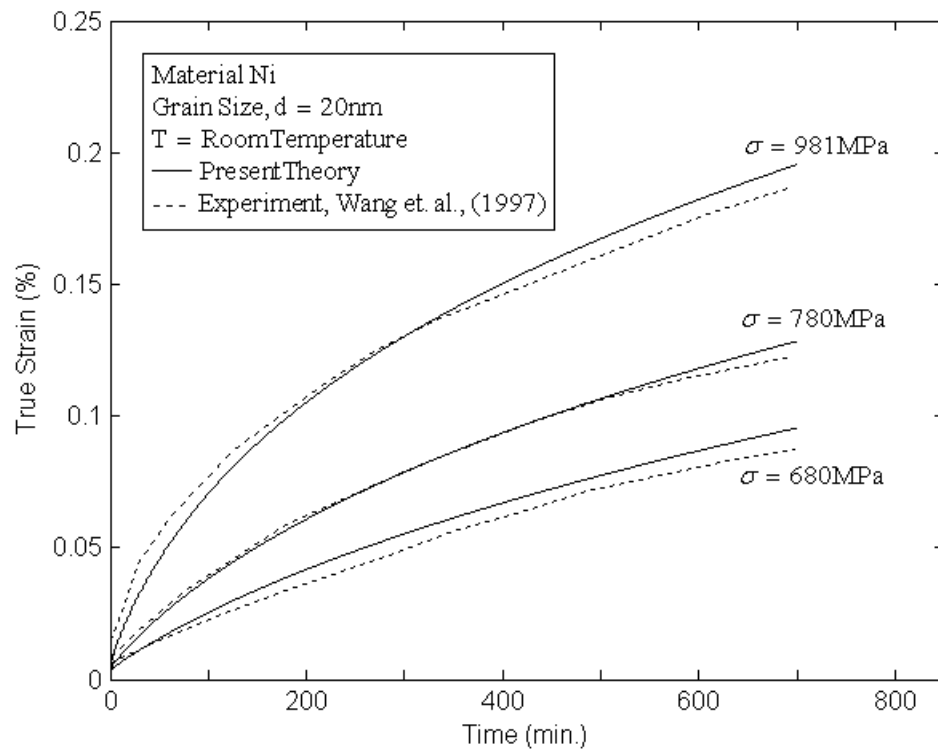


Fig. 4.5: Comparison between the developed theory and the test data of Wang et al. [44].

grain size, and stress dependence in the time-dependent creep of nanocrystalline solids.

Now in order to provide deeper insights into the grain-size dependence of the overall creep, we applied the developed model to examine the potential grain size hardening and softening of nanocrystalline Cu. The results are displayed in Fig. 4.6. As the grain size decreases from 50 nm to 35 nm, and further down to 25 nm, the generated creep strain is seen to continue to decrease. This is a phenomenon of grain size hardening in creep. But as it further decreases to 10 nm, the generated creep strain conspicuously increases, and this gives rise to the grain size softening.

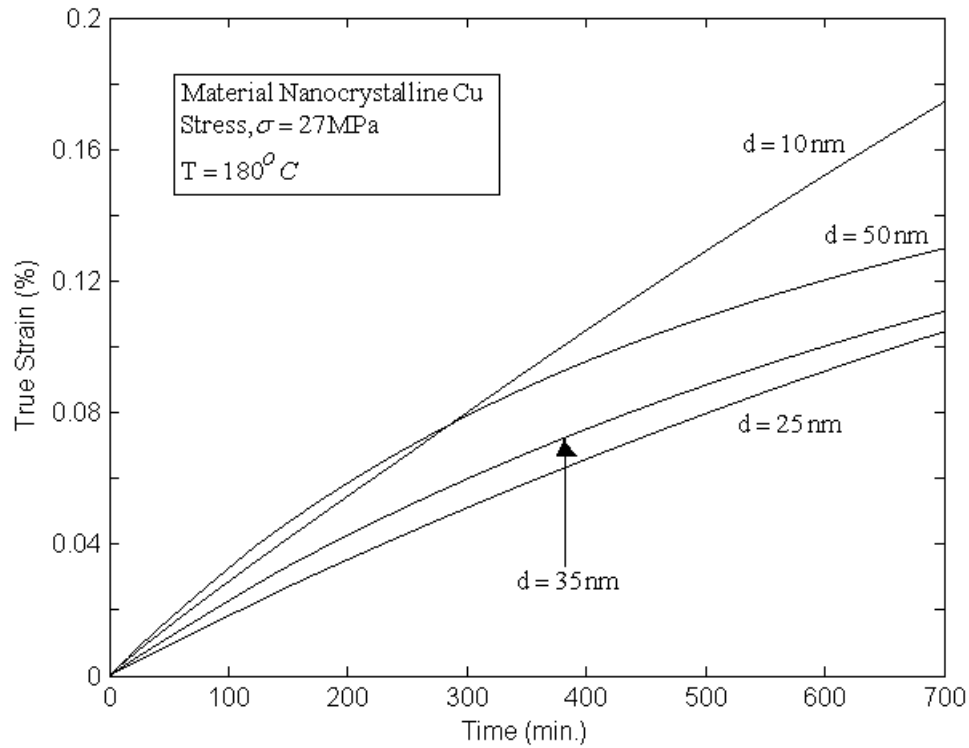


Fig 4.6: Grain size hardening and softening of a nanocrystalline copper.

To pave way for the study of creep resistance, we have made several more calculations so that continuous variations of creep strain versus the inverse of grain size,  $d^{-1/2}$ , can be visualized.

Fig. 4.7(a) shows such a variation at four selected temperature. The existence of a minimum at a

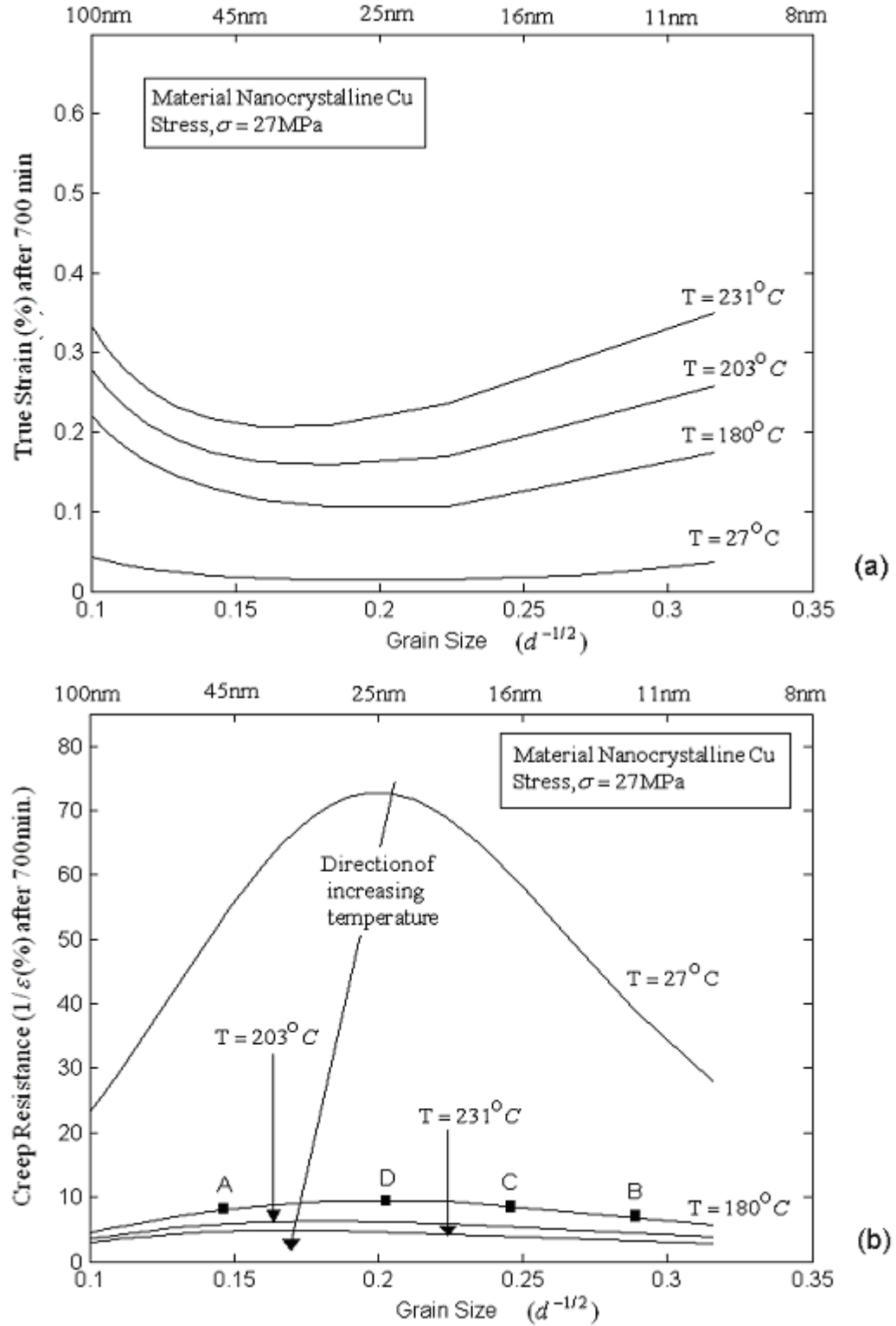


Fig 4.7 (a) Creep strain and (b) creep resistance of Cu versus the square root of the reciprocal of the grain size at various temperature.

given temperature indicates that there exists a grain size that marks the minimum creep strain. To put creep resistance of a material in a setting that resembles that of hardness or yield strength, we take it to be represented by the *inverse* of creep strain generated at a given time. Based on such a representation, the variation of creep resistance versus  $d^{-1/2}$  is plotted in Fig. 4.7(b), at the same four different levels of temperature. This plot is similar to the Hall-Petch plot shown in Fig. 2.1(a) and 2.1(b); initially it shows a positive slope, then reaching a maximum at a critical grain size,  $d_{crit}$ , and finally a negative slope.

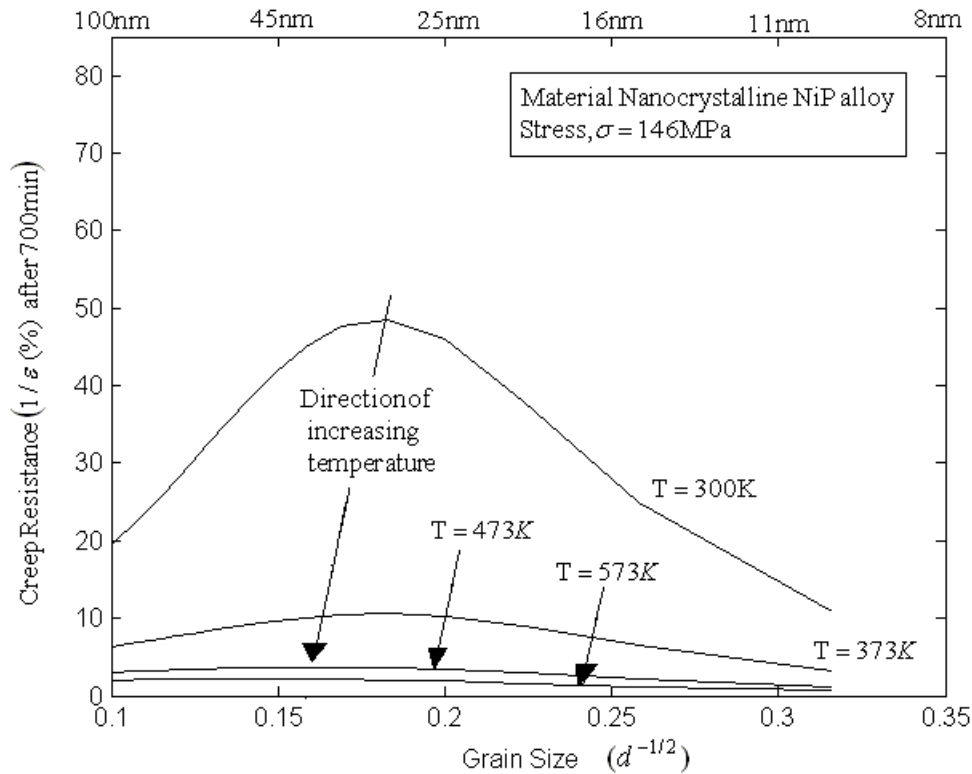


Fig 4.8: Creep resistance of NiP alloy versus the square root of the reciprocal of the grain size at various temperature. Note that the grain size softening starts at around 35nm for 373K and at around 60 nm for 573K.

Creep resistance curves for NiP alloy are plotted in Fig 4.8. These results show a similar trend. Both figures indicate that there exists a critical grain size,  $d_{crit}$ , at which maximum creep resistance occurs. This critical grain size tends to shift to the left as temperature increases. The

major reason for such a left shift is that, at a higher temperature, the increased contribution from the softer GBAZ would compensate for a lower volume concentration of its own as compared to the condition at a lower temperature, and a lower volume concentration of GBAZ means a larger grain size. Most important of all, this critical grain size occurs at the nanometer scale. So to maximize the creep resistance of a material it is critical to produce it with a grain size that is in the nanometer range. The precise value of this size, however, needs to be calculated.

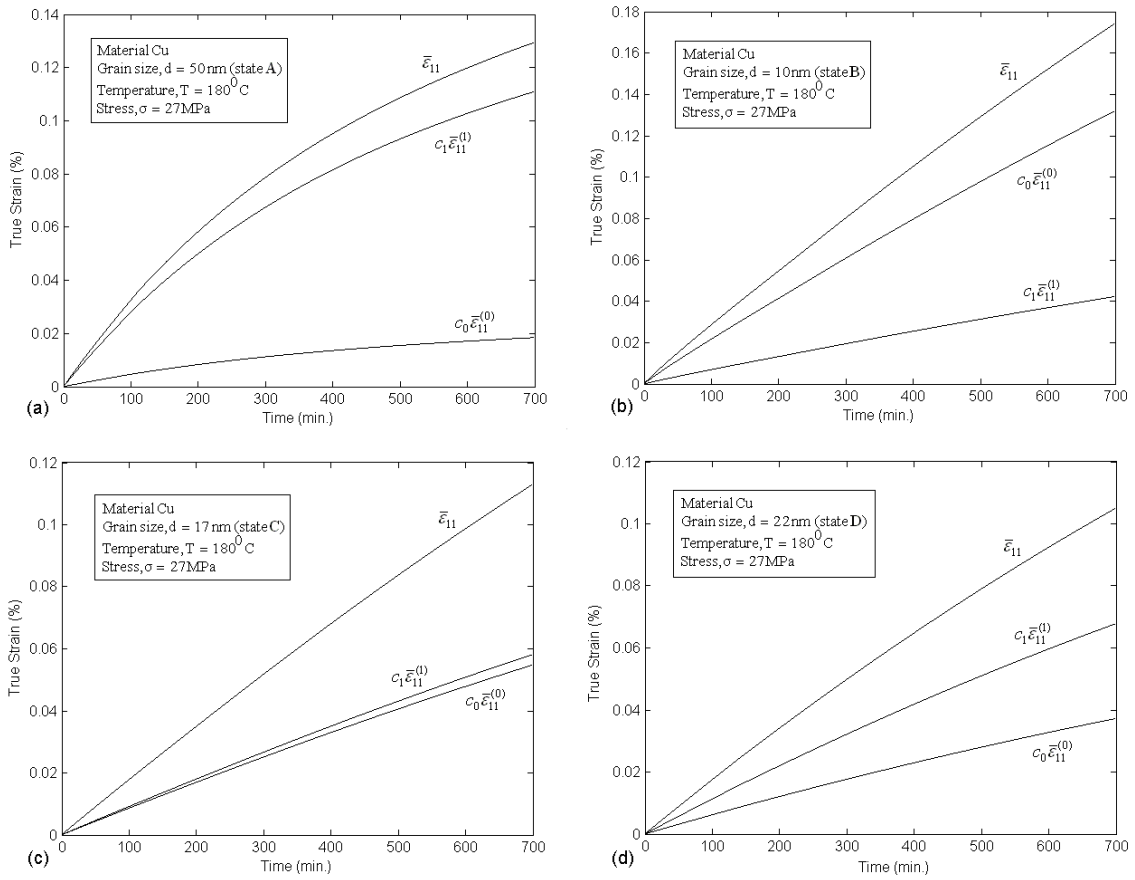


Fig 4.9: Contributions of the grain interior and GBAZ toward the total strain of the nanocrystalline solid at four grain sizes: (a) larger than  $d_c$ , (b) smaller than  $d_c$ , (c) one with about equal contributions, and (d) at  $d_c$ .

The marked points A, B, C, and D on the 180°C curve in Fig. 4.7 (b), carry some important meaning. Point A represents a generic state on the left branch of the curve where the creep

resistance *versus*  $d^{-1/2}$  plot has a positive slope, whereas point B on the right branch is a similar one where the plot has a negative slope. These two points can be considered to be representative of the two states lying in Fig. 2.1(a) and 2.1(b), respectively, of the indentation test. Since we have conjectured that the left branch is controlled by the grain interior and the right one by the GBAZ, it is necessary to show their relative contributions at these two states. The results are plotted in Figs. 4.9(a) and 4.9(b), respectively. These two curves, which have been multiplied by their respective volume concentrations  $c_1$  and  $c_0$ , give their contributions to the overall creep. It is apparent that, at state A, the grain interior dominates the deformation whereas at state B, the GBAZ makes the major contribution. It is then interesting to locate the state of grain size at which the grain interior and GBAZ make about equal contributions to the overall creep. This point is located at point C, and the corresponding contributions are shown in Fig. 4.9(c). This point is seen to lie on the early descending part of the right branch. At point D, the maximum, the material has the highest creep resistance. At this critical grain size, as shown in Fig. 4.9(d), the grain interior is seen to still make more contribution to the overall creep of the nanocrystalline solid. The formula used to calculate the evolution of the strain,  $\bar{\varepsilon}_{ij}^{(1)}(t)$ , in these plots is derived in Appendix A3.

Before closing the chapter a brief remark on the issue of creep compressibility of nanocrystalline solids should be given. Even though both the grain interior and GBAZ are plastically incompressible, the nanocrystalline material is in general compressible. This is due to the fact that the creep strain of a dual-phase material is not a direct, weighted mean of its constituent creep strains unless both phases have identical elastic moduli. To see such an effect, the dilatational creep strain of the dual-phase material under a dilatational loading by varying the Young's modulus of the grain interior (keeping other constants unchanged) is plotted in Fig. 4.10(a). It is evident that creep compressibility is quite pronounced if the grain interior is softer than the GBAZ, and it still remains significant even if the interior is harder. Only when both

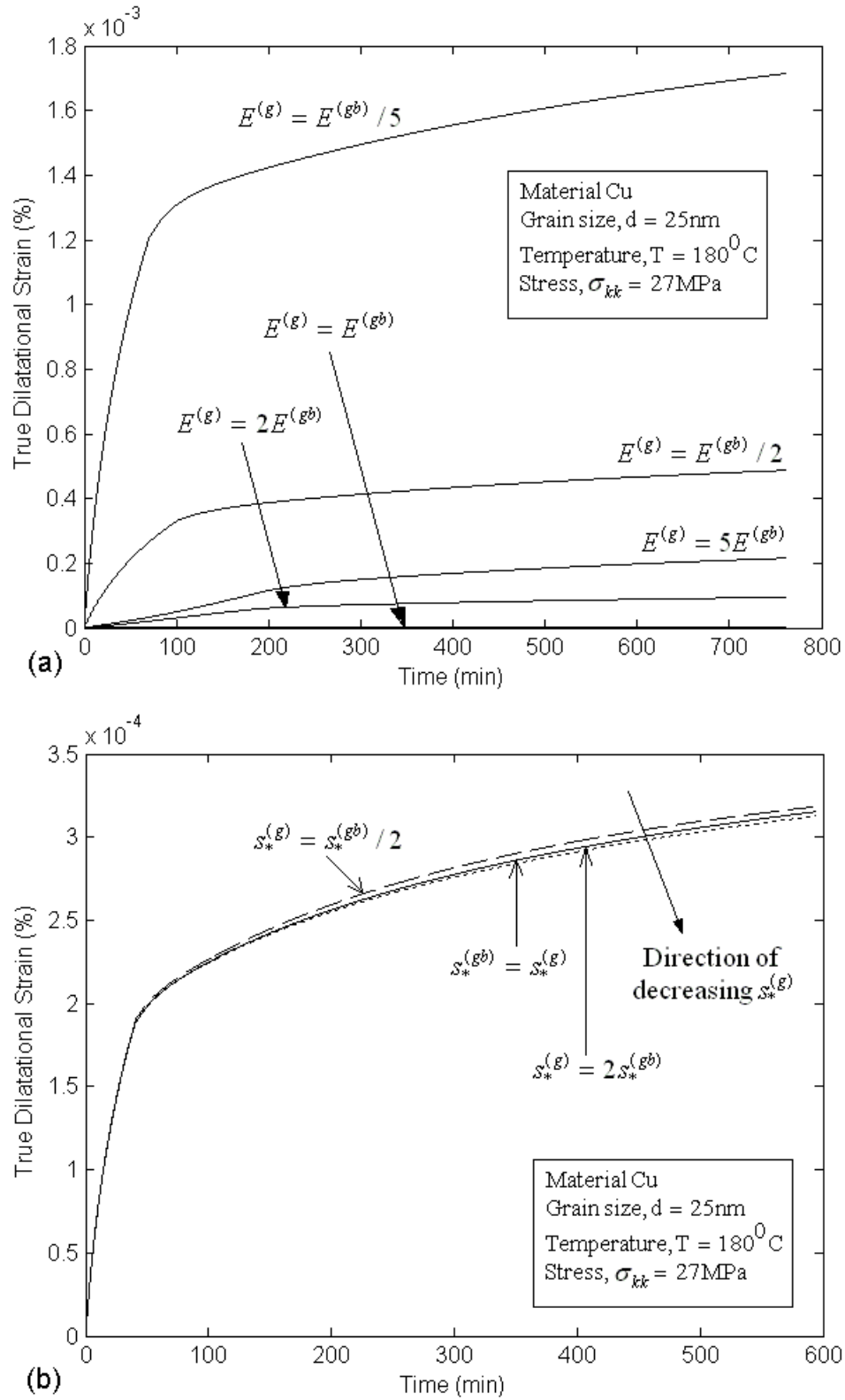


Fig. 4.10 Dilatational creep of a nanocrystalline solid as a function of (a) elastic property ratio, and (b) grain size strength ratio between the grain interior and GBAZ.

phases have identical elastic moduli that the material is incompressible, and this, of course, is expected. On the other hand with the change of the saturation strength of the grain interior  $s_*^{(g)}$  alone, it was found that, as shown in Fig. 4.10(b), it does not alter the amount of compressibility in any significant way. It can be concluded that the elastic bulk modulus of the inclusion phase plays the dominant role in deciding the extent of overall compressibility.

The values of some of the parameters given in tables 4.1, 4.2 and 4.3 are extracted from the journal articles where these experimental results were published. Such as the values of the Young's modulus ( $E_{RT}$ ) and the activation energy ( $Q$ ) were assumed to be the one given in Sanders et al. [42], Wang et al. [43] and Wang et al. [44]. The values of the other parameters have been obtained by inverse simulation of the test data.

**Table 4.1 Material parameters used in calculation for Cu**

| Material Property      | Grain Interior | GBAZ   |
|------------------------|----------------|--------|
|                        |                |        |
| $E_{RT}$ (GPa)         | 120            | 120    |
| $\alpha_T$             | 0.0009         | 0.0007 |
| $\nu$                  | 0.31           | 0.3    |
| $s_0$ (MPa)            | --             | 130    |
| $s_*$ (MPa)            | --             | 400    |
| $n$                    | 3.8            | 3.5    |
| $s_0^{(\infty)}$ (MPa) | 5.5            | --     |
| $k$ (MPa $\sqrt{nm}$ ) | 1500           | --     |
| $a$                    | 1.3            | --     |
| $h$ (MPa)              | 20000          | 10000  |
| $Q$ (J / M)            | 17000          | 7000   |

**Table 4.2 Material parameters used in calculation for NiP alloy**

| Material Property      | Grain Interior | GBAZ   |
|------------------------|----------------|--------|
|                        |                |        |
| $E_{RT}$ (GPa)         | 50             | 50     |
| $\alpha_T$             | 0.0005         | 0.0015 |
| $\nu$                  | 0.26           | 0.28   |
| $s_0$ (MPa)            | --             | 120    |
| $s_*$ (MPa)            | --             | 350    |
| $n$                    | 4              | 3.5    |
| $s_0^{(\infty)}$ (MPa) | 5.5            | --     |
| $k$ (MPa $\sqrt{nm}$ ) | 2200           | --     |
| $a$                    | 8.2            | --     |
| $h$ (MPa)              | 60000          | 1000   |
| $Q$ (J / M)            | 39000          | 2000   |

**Table 4.3 Material Properties for nanocrystalline Ni**

| Material Property      | Grain Interior | GBAZ   |
|------------------------|----------------|--------|
|                        |                |        |
| $E_{RT}$ (GPa)         | 210            | 200    |
| $\alpha_T$             | 0.0002         | 0.0002 |
| $\nu$                  | 0.312          | 0.3    |
| $s_0$ (MPa)            | --             | 220    |
| $s_*$ (MPa)            | --             | 600    |
| $n$                    | 4.7            | 3.5    |
| $s_0^{(\infty)}$ (MPa) | 5.5            | --     |
| $k$ (MPa $\sqrt{nm}$ ) | 1200           | --     |
| $a$                    | 2.4            | --     |
| $h$ (MPa)              | 5000           | 200    |
| $Q$ (J / M)            | 24000          | 22000  |

## Chapter 5

### Strain-Rate Sensitivity

It was discussed earlier that with decreasing grain size the yield stress of a material increases and for nanocrystalline materials it is observed to be 4-5 times higher than their coarse grained counterpart. The relation between linear increments of the yield stress with the reciprocal of the square root of the grain diameter is known as the Hall-Petch effect. Change in yield strength with decreasing grain size is best observed in constant strain rate tests. The stress-strain relation of a typical constant strain rate test at different grain size and varying strain rate with constant grain size is given as follows,

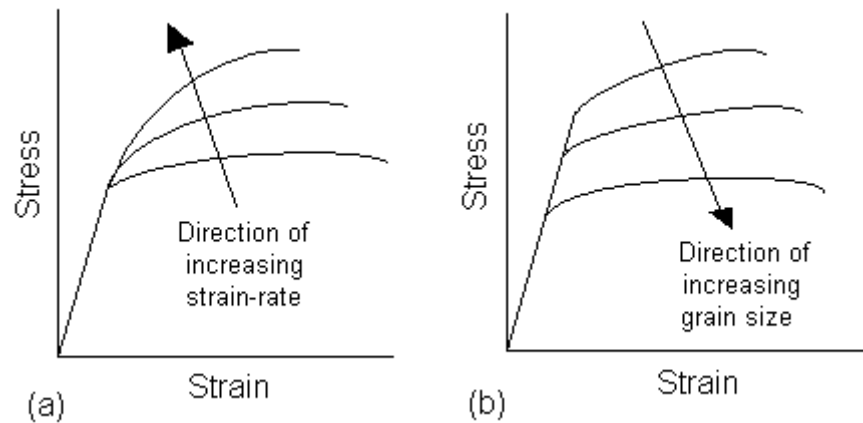


Fig 5.1: Schematic stress-strain plot at (a) constant grain size but different strain rate (b) constant strain rate but different grain size.

#### 5.1 Mechanism for Hall-Petch effect, inverse Hall-Petch effect and strain-rate hardening

The reason behind the increase in yield strength with decreasing grain size has been the literature of discussion in several works. The most accepted idea that there is dislocation pile up at the grain boundaries. Since the lattice structures of adjacent grains differ in orientation, it

requires more energy for a dislocation to change direction and move into the adjacent grain. The grain boundary region itself is more disordered than the grain interior and so it is difficult for the dislocations to move through this region. Thus the grain boundary exerts a hindrance to the movement of the dislocation which delays the onset of plastic deformation and the yield strength of the material increase.

Under some particular applied stress, all the dislocations come and accumulate around the grain boundary region. This accumulation of a cluster of dislocations at the grain boundary region is known as dislocation 'pile up'. As dislocations generate repulsive stress fields, each successive dislocation in the 'pile up' will apply a repulsive force incident with the grain boundary. These repulsive forces act as a driving force to reduce the energy barrier for diffusion across the grain boundary. Thus additional pile up causes dislocation diffusion across the grain boundary, allowing further deformation in the material. For this reason, materials with very high grain size (in the  $\mu m$  range) have large possibility of dislocation pile up to occur which would eventually help in the plastic deformation of solid.

With the decrease in grain size, the grain boundary region increases which results in the decrease of the possibility of dislocation pile up at the grain boundary region. So, a greater amount of stress has to be applied to the material to make the dislocation move across the grain boundary. This in turn would increase the yield strength of the material. Thus we have an increment in yield strength with decreasing grain size. The Hall-Petch relation was derived by Hall [18] and Petch [19] which is given as,

$$\sigma_y = \sigma_0 + kd^{-1/2} \quad (5.1)$$

where,  $\sigma_y$  is the yield stress of the material,  $\sigma_0$  is the resistance of the lattice to the dislocation motion,  $d$  is the grain diameter and  $k$  is the strengthening coefficient.

But the yield strength of the material cannot increase infinitely as the grain size goes to zero. This is because with zero grain size, the solid is left with only the grain boundary region which is more disordered and amorphous than the grain. As amorphous material has lower yield strength than crystalline materials, the solid with zero grain size will be softer than the crystalline one. The Hall-Petch mechanism ceases to work below the grain size of  $d = 25nm$ . For such small grains only one or two dislocations can fit inside them. This scheme prohibits dislocation pile up and never results in grain boundary diffusion. In reality the stress required for the grain boundary diffusion to occur is so high that, before it is reached, other deformation mechanisms based on dislocation, diffusion of atoms or grain boundary sliding causes the material to flow and gives rise to the Inverse Hall-Petch Effect by reducing the yield strength of the material.

The inverse Hall-Petch effect has been observed in several experiments as well as molecular dynamic simulations. But discussion on the mechanism of this grain size softening is still going on. Four different kinds of mechanism could be found in Carlton and Ferreira [45]. One of them suggests that the dislocation mechanism inside the grain becomes different when the grain size goes below some threshold value. The energy required for movement of dislocations in nanocrystalline solids is lower than that in coarse grained materials. These dislocations at the lower energy lead to grain size softening. Another dislocation based mechanism is deformation twinning in the grains that might cause the inverse Hall-Petch effect.

Some studies suggest that the diffusion of atoms in the grain boundary at low temperatures is the cause for grain size softening. This is something similar to the Coble creep mechanism. Grain boundary sliding has also been mentioned as the reason for inverse Hall-Petch effect. Some molecular dynamic simulations and analytical models support this idea. According to this theory, grain boundary shearing/sliding begins to dominate the dislocation motion as the primary means of deformation at very low grain sizes.

The last mechanism considers the nanocrystalline material as a composite where the plastically strong grains are embedded within the continuous as well as softer grain boundary region. This is similar to the idea that conventional materials can be strengthened by precipitates. As the grain size becomes smaller, the volume fraction of the grains decreases and the grain boundary region increases. In the nanocrystalline range, beyond a critical grain size, the volume fraction of the grains becomes so small that the maximum stress is carried by the plastically softer grain boundary region. As a result, the yield stress of the entire material decreases. As the grain size is reduced, more stress is carried by the grain boundary region which results in even more decrease in yield strength and this gives rise to the inverse Hall-Petch effect. A similar model has been considered here.

It has been observed in several experiments, as well as in analytical and molecular dynamic simulations, that as the strain rate is increased the yield strength of the material also increases, but the ductility decreases. The plastic deformation of materials is governed by the movement of the dislocations inside the grain as well as in the grain boundary regions. There are lots of obstacles to the motion of the dislocation. So it takes some time to overcome the hindrance and establish a path to move. As a result, under some applied stress, the dislocations start to move at different instants and it is not an instantaneous process. When the strain rate is increased, the dislocations try to move in less amount of time which needs more external stress. So, to obtain a particular displacement, the applied stress is higher at higher strain rates. This explains the reason for increased yield strength at high strain rate loadings. For a given material, the total energy it can sustain before failure is constant. Energy is given by the area under the stress-strain curve. At lower strain rates the yield is reached at a low level of stress. So it is possible for the solid to have more plastic deformation. On the other hand, for the high strain rate case, where the yield stress is higher, a large amount of plastic deformation is not supported due to the limitation in the total energy before failure. For this reason solids under high strain rates behave as brittle materials.

## 5.2 Rate-dependent constitutive relations of the grain interior and the GBAZ

The stress strain behavior of a nanocrystalline material, under constant strain rate loading, will be captured by a rate dependent viscoplastic model. The rate-dependent viscoplastic behavior of the grain interior and GBAZ will be modeled by a set of unified constitutive equations. The total strain-rate in each phase is taken to be the sum of the elastic and viscoplastic counterparts, as

$$\dot{\epsilon}_{ij} = \dot{\epsilon}_{ij}^e + \dot{\epsilon}_{ij}^{vp}. \quad (5.2)$$

The elastic part depends on stress through the usual isotropic connection, whereas the viscoplastic one follows from the Prandtl-Reuss relation

$$\dot{\epsilon}_{ij}^{vp} = \frac{3}{2} \frac{\dot{\epsilon}_e^{vp}}{\sigma_e} \sigma_{ij}', \quad (5.3)$$

where  $\sigma_e$  is the effective stress and  $\dot{\epsilon}_e^{vp}$  the effective viscoplastic strain rate defined as

$$\sigma_e = \left( \frac{3}{2} \sigma_{ij}' \sigma_{ij}' \right)^{1/2}, \quad \dot{\epsilon}_e^{vp} = \left( \frac{2}{3} \dot{\epsilon}_{ij}^{vp} \dot{\epsilon}_{ij}^{vp} \right)^{1/2}, \quad (5.4)$$

in terms of the deviatoric stress  $\sigma_{ij}'$  and viscoplastic strain rate  $\dot{\epsilon}_{ij}^{vp}$ .

The unified constitutive relation is cast in the usual power-law form, as

$$\dot{\epsilon}_e^{vp} = \dot{\epsilon}_0^{vp} \cdot \left( \frac{\sigma_e}{s} \right)^n, \quad (5.5)$$

where  $n$  is the stress exponent, and  $s$  is the drag stress. The reference strain rate  $\dot{\epsilon}_0^{vp}$  is a scaling factor and can be set arbitrarily. The drag stress increases with deformation, and can be taken to be controlled by the competition between strain hardening and recovery in the form

$$\dot{s} = h \cdot \left( 1 - \frac{s}{s_*} \right) \dot{\epsilon}_e^{vp}, \quad (5.6)$$

so that, upon integration, it depends on the current strain as

$$s = s_* - (s_* - s_0) e^{-\frac{\epsilon_e^{vp}}{s_* / h}}, \quad (5.7)$$

where  $s_0$  represents the initial hardening state and  $s_*$  the final saturation state. So there are three key material constants for each phase: the power  $n$ , the initial strength  $s_0$ , and the saturation strength  $s_*$ .

This set of constitutive relations applies to both the grain and GBAZ, but each has its own constants. To make the symbols more indicative, we shall use the subscript  $(g)$  to stand for the grain interior and  $(gb)$  for the GBAZ. Since the drag stress represents the hardening state of the phase, it is taken to follow the Hall-Petch equation for the grain interior, as given by Weng [46],

$$s_0^{(g)} = s_0^\infty + kd^{-1/2}, \quad s_*^{(g)} = a s_0^{(g)}. \quad (5.8)$$

But those of the GBAZ are grain-size independent and can be written simply as  $s_0^{(gb)}$  and  $s_*^{(gb)}$ . Constants  $s_0^\infty$  and  $k$  in eq. (5.8) are the Hall-Petch constants, and  $a$  relates the saturation strength to the initial strength of the grain interior. This set of constitutive equations was also adopted by Li and Weng [32].

For such an elastic-viscoplastic phase, say phase  $r$ , its secant viscosity  $\eta_r^s$  is defined through

$$\dot{\epsilon}_{ij}^{vp(r)} = \frac{1}{2\eta_r^s} \sigma_{ij}^{(r)}, \text{ or } \dot{\epsilon}_e^{vp(r)} = \frac{1}{3\eta_r^s} \sigma_e^{(r)}. \quad (5.9)$$

In view of eq. (5.5), it can be written specifically for the grain interior (phase 1) and GBAZ (phase 0), as

$$\eta_1^s = \frac{s^{(g)}}{3\dot{\epsilon}_e^{vp}} \cdot \left( \frac{\dot{\epsilon}_e^{vp}}{\dot{\epsilon}_0^{vp}} \right)^{1/n^{(g)}}, \quad \eta_0^s = \frac{s^{(gb)}}{3\dot{\epsilon}_e^{vp}} \cdot \left( \frac{\dot{\epsilon}_e^{vp}}{\dot{\epsilon}_0^{vp}} \right)^{1/n^{(gb)}}. \quad (5.10)$$

These secant viscosities thus continue to change during plastic deformation. The dilatational behavior of each phase is taken to be plastically incompressible and is characterized solely by its elastic bulk modulus. As mentioned before in the previous chapter, most of the constitutive relations shown in this section are available in any text book related to plasticity. Equation (5.10) was derived using eq. (5.3), (5.5) and (5.9).

### 5.3 A homogenization scheme for the viscoplastic response of the 3-phase model

In order to develop a nonlinear, rate-dependent, multi-phase homogenization model that remains explicit and is also capable of capturing plastic compressibility under a pure hydrostatic loading, Laplace transform is used at first to convert a linear elastic homogenization method to a linear viscoelastic one. The Maxwell viscosity of the viscoelastic phases is then replaced by the secant viscosity of the viscoplastic phases. A field-fluctuation method is also introduced to find the connections between the micro strain rates and the applied, macro strain rate. To a great extent this homogenization method is an extension of the concept of a linear comparison composite. The history in the development of the nonlinear homogenization method by use of the linear one with an identical microgeometry was discussed in the previous chapter of “Creep Response”. For the method to remain explicit, and to make the partial derivatives involved in the field fluctuation method manageable [see Eq. (5.27)], the starting point has been taken to be the Mori-Tanaka (M-T) approach for the linear elastic composite, and then, through the Laplace transform, the results are extended to a linear viscoelastic composite comprised of two Maxwell phases to mimic the grain interior and GBAZ, in addition to the pores. The Maxwell viscosity will then be replaced by the secant viscosity to study the rate-dependent, nonlinear problem. Christensen and Lo’s [37] generalized self-consistent approach can also be extended to a three-phase composite as the starting point, but it would greatly add complexities in the expression of

the effective properties and the evaluation of the partial derivatives. The advantage of using the M-T approach was also recognized by Tan et al. [47] in their study on the effect of nonlinear interface debonding.

### 5.3.1 The initial elastic state

For a general 3-phase composite containing two types of spherical inclusions, the effective bulk and shear moduli of the composite are given by (Weng [10])

$$\frac{\kappa}{\kappa_0} = 1 + \frac{(c_1 + c_2)\alpha_0(\kappa_1 - \kappa_0)(\kappa_2 - \kappa_0) + c_1\kappa_0(\kappa_1 - \kappa_0) + c_2\kappa_0(\kappa_2 - \kappa_0)}{\kappa_0^2 + (1 - c_2)\alpha_0\kappa_0(\kappa_2 - \kappa_0) + (1 - c_1)\alpha_0\kappa_0(\kappa_1 - \kappa_0) + [1 - (c_1 + c_2)]\alpha_0^2(\kappa_1 - \kappa_0)(\kappa_2 - \kappa_0)} \quad (5.11a)$$

$$\frac{\mu}{\mu_0} = 1 + \frac{(c_1 + c_2)\beta_0(\mu_1 - \mu_0)(\mu_2 - \mu_0) + c_1\mu_0(\mu_1 - \mu_0) + c_2\mu_0(\mu_2 - \mu_0)}{\mu_0^2 + (1 - c_2)\beta_0\mu_0(\mu_2 - \mu_0) + (1 - c_1)\beta_0\mu_0(\mu_1 - \mu_0) + [1 - (c_1 + c_2)]\mu_0^2(\mu_1 - \mu_0)(\mu_2 - \mu_0)} \quad (5.11b)$$

where

$$\alpha_0 = \frac{3\kappa_0}{3\kappa_0 + 4\mu_0}, \quad \beta_0 = \frac{6}{5} \frac{\kappa_0 + 2\mu_0}{3\kappa_0 + 4\mu_0}, \quad (5.12)$$

and  $\kappa_2 = \mu_2 = 0$  for voids.

Since the initial response of the composite under a constant strain-rate loading is elastic, it is helpful to write the hydrostatic and deviatoric stresses of the constituent phases (say, the  $r$ -th phase) in terms of that of the composite  $\bar{\sigma}_{ij}$

$$\bar{\sigma}_{kk}^{(r)} = \frac{\kappa_r}{[\alpha_0(\kappa_r - \kappa_0) + \kappa_0][1 + (1 - \alpha_0)a]} \bar{\sigma}_{kk}, \quad (5.13a)$$

$$\bar{\sigma}_{ij}^{'(r)} = \frac{\mu_r}{[\beta_0(\mu_r - \mu_0) + \mu_0][1 + (1 - \beta_0)b]} \bar{\sigma}_{ij}', \quad (5.13b)$$

where,

$$a = \frac{c_1(\kappa_1 - \kappa_0)}{\alpha_0(\kappa_1 - \kappa_0) + \kappa_0} - \frac{c_2}{(1 - \alpha_0)}, \quad b = \frac{c_1(\mu_1 - \mu_0)}{\beta_0(\mu_1 - \mu_0) + \mu_0} - \frac{c_2}{(1 - \beta_0)}. \quad (5.14a \text{ and } b)$$

### 5.3.2 Transition to the viscoelastic state in the Laplace transformed domain

To pave the way for the study of the viscoplastic response, the basic relations for a linear viscoelastic comparison composite whose microgeometry is identical to Fig. 3.2, is established. Since the problem involves two viscoplastic phases, the most suitable viscoelastic comparison composite is one involving two Maxwell solids. In this way the Maxwell viscosity can be later converted into the secant viscosity for each constituent phase.

The shear behavior of the  $r$ -th viscoelastic phase is marked by its shear modulus  $\mu_r$  and shear viscosity  $\eta_r$ . In the Laplace, transformed domain (TD), its shear modulus can be written as

$$\mu_r^{TD} = \frac{\mu_r s}{s + T_r}, \quad \text{with} \quad T_r = \frac{\mu_r}{\eta_r}, \quad (5.15)$$

where  $s$  is the usual Laplace parameter (similar to section 4.3.2,  $s$  is used as the Laplace parameter in this section only and it should not be confused with the drag stress which is also denoted by  $s$  and it appears in other sections). The dilatational behavior is simply marked by its bulk modulus  $\kappa_r$  (i.e.  $\kappa_r^{TD} = \kappa_r$ ) due to plastic incompressibility. Then by means of the correspondence principle (Hashin [9]), the viscoelastic behavior of the composite can be determined from the elastic one with the same microgeometry. The stress and strain in the transformed domain is denoted by a hat  $\hat{\cdot}$ , so that, for the  $r$ -th phase,

$$\hat{\sigma}_{kk}^{(r)} = 3\kappa_r \hat{\varepsilon}_{kk}^{(r)}, \quad \hat{\sigma}_{ij}^{(r)} = 2\mu_r^{TD} \hat{\varepsilon}_{ij}^{(r)}, \quad (5.16)$$

and for the composite,

$$\hat{\sigma}_{kk} = 3\kappa^{TD} \hat{\varepsilon}_{kk}, \quad \hat{\sigma}_{ij} = 2\mu^{TD} \hat{\varepsilon}_{ij}. \quad (5.17)$$

Then the effective  $\kappa^{TD}$  and  $\mu^{TD}$  of the 3-phase composite in the transformed domain follow from eq. (5.11), with  $\mu_r$  now replaced by  $\mu_r^{TD}$ . Using such a relation for the 3-phase porous medium, the effective moduli in the transformed domain can be cast into

$$\begin{aligned}\kappa^{TD} &= \kappa_0 \left\{ 1 + \frac{[(c_1 + c_2)\alpha_0^{TD} - c_1](\kappa_1 - \kappa_0) + c_2\kappa_0}{[(1 - c_2)\alpha_0^{TD} - 1]\kappa_0 + (\kappa_1 - \kappa_0)[c_0(\alpha_0^{TD})^2 - (1 - c_1)\alpha_0^{TD}]} \right\}, \\ \mu^{TD} &= \mu_0^{TD} \left\{ 1 + \frac{[(c_1 + c_2)\beta_0^{TD} - c_1](\mu_1^{TD} - \mu_0^{TD}) + c_2\mu_0^{TD}}{[(1 - c_2)\beta_0^{TD} - 1]\mu_0^{TD} + (\mu_1^{TD} - \mu_0^{TD})[c_0(\beta_0^{TD})^2 - (1 - c_1)\beta_0^{TD}]} \right\},\end{aligned}\tag{5.18a and b}$$

where,

$$\alpha_0^{TD} = \frac{3\kappa_0}{3\kappa_0 + 4\mu_0^{TD}}, \quad \beta_0^{TD} = \frac{6}{5} \frac{\kappa_0 + 2\mu_0^{TD}}{3\kappa_0 + 4\mu_0^{TD}}.\tag{5.19a and b}$$

Making use of eq. (5.17), and noting that, under a constant strain-rate loading  $\hat{\varepsilon}_{ij} = (1/s^2) \cdot \dot{\varepsilon}_{ij}$ , it can be written that,

$$\bar{\sigma}_{kk}(t) = 3\eta_{\kappa}(t)\dot{\varepsilon}_{kk}, \quad \bar{\sigma}_{ij}'(t) = 2\eta_{\mu}\dot{\varepsilon}_{ij}',\tag{5.20}$$

where  $\eta_{\kappa} = \mathcal{L}^{-1}(\kappa^{TD}/s^2)$ ,  $\eta_{\mu} = \mathcal{L}^{-1}(\mu^{TD}/s^2)$ , with the symbol  $\mathcal{L}^{-1}$  standing for the inverse Laplace operator. After some lengthy algebra, it was found that,

$$\eta_{\kappa}(t) = \kappa_0 \left\{ A + pe^{-rt} \left[ \cos(wt) + \frac{q-r}{w} \sin(wt) \right] \right\},\tag{5.21a}$$

$$\eta_{\mu}(t) = \left( 1 + \frac{x_4}{x_8} \right) \eta_0 - (\eta_0 - \delta) e^{-T_0 t} + E \left\{ F_1 e^{\lambda_1 t} + e^{a_1 t} [(F_2 + F_3) \cos(b_1 t) + (F_2 - F_3) \sin(b_1 t)] \right\}.$$

$$(5.21b)$$

in terms of time  $t$ . The entire procedure and the constants involved here can be found in Appendix A4. It is evident from the expression of  $\eta_\kappa$  that this approach will deliver a nonlinear response under a pure dilatational loading.

### 5.3.3 Replacement of the Maxwell viscosity by the secant viscosity for the viscoplastic response

In the extension from linear elasticity to nonlinear, rate-independent plasticity, the elastic moduli of the constituent phases are replaced by their corresponding secant moduli. Likewise, the extension from linear viscoelasticity to the nonlinear, rate-dependent viscoplasticity can be carried out with the replacement of Maxwell viscosities,  $\eta_1$  and  $\eta_0$ , by the secant viscosities  $\eta_1^s$  and  $\eta_0^s$  calculated from eq. (5.10). These secant viscosities then enter into the parameters involved. Equation (5.20) is then replaced by

$$\bar{\sigma}_{kk}(t) = 3\eta_\kappa^s(t)\dot{\varepsilon}_{kk}, \quad \bar{\sigma}_{ij}^s(t) = 2\eta_\mu^s(t)\dot{\varepsilon}_{ij}^s. \quad (5.22)$$

The two functions  $(\eta_\kappa^s, \eta_\mu^s)$  now carry the notions of overall secant viscosities of the composite.

The uniaxial counterpart of eq. (5.22) can be written as  $\bar{\sigma}_{11}(t) = \eta_E^s(t)\dot{\varepsilon}_{11}^s$ . Under a constant strain-rate loading the nanocrystalline solid behaves essentially like a non-Newtonian fluid.

## 5.4 A field-fluctuation method to find the secant viscosity of the constituent phases

A critical step in this process is to find  $\eta_1^s$  and  $\eta_0^s$  that enter into the parameters involved in eq. (5.21) for the application of eq. (5.22). Since the secant viscosity depends on the drag stress  $s$  and the effective strain rate  $\dot{\varepsilon}_e^{vp}$  through eq. (5.10), and  $s$  further depends on  $\varepsilon_e^{vp}$  through eq. (5.6) and eq. (5.7), the task boils down to the determination of the effective rate  $\dot{\varepsilon}_e^{vp}$  for both the grain interior and GBAZ. It was found that this could be most conveniently achieved through the application of field fluctuation method. It is similar to the field fluctuation method applied in the

previous chapter to obtain the effective stress in the individual phases in terms of the external applied stress.

It has the same advantage that, under the same boundary condition, a change in the material parameter of a constituent phase will result in a field fluctuation that gives rise to a new overall energy. Thus by taking a partial derivative of this energy with respect to such a material parameter, a universal relation will follow. For the present rate-dependent viscoplastic problem with a linear viscoelastic comparison composite, the pertinent energy term is the overall work rate, and the material parameters at issue are the secant viscosities  $\eta_1^s$  and  $\eta_0^s$ . This approach is now used to establish the connection between the effective strain rates,  $\dot{\bar{\epsilon}}_e^{vp(1)}$  and  $\dot{\bar{\epsilon}}_e^{vp(0)}$ , respectively of the grain interior and GBAZ, and the overall applied strain rate,  $\dot{\bar{\epsilon}}_{ij}$ .

With the above  $\eta_\kappa^s$  and  $\eta_\mu^s$ , the overall work rate of the composite under a constant strain-rate loading,  $\dot{\bar{\epsilon}}_{ij} = \text{const.}$ , can be written as

$$\dot{U} = \bar{\sigma}_{ij} \dot{\bar{\epsilon}}_{ij} = \eta_\kappa^s (\dot{\bar{\epsilon}}_{kk})^2 + 2\eta_\mu^s \dot{\bar{\epsilon}}_{ij}' \dot{\bar{\epsilon}}_{ij}'. \quad (5.23)$$

On the other hand, it can be considered as the sum of the elastic and viscoplastic components of the constituent phases, as

$$\dot{U} = c_1 (\dot{U}_1^e + \dot{U}_1^{vp}) + c_0 (\dot{U}_0^e + \dot{U}_0^{vp}), \quad (5.24)$$

noting that pores make no contribution to it. The elastic term for each phase can be written readily through its elastic moduli, whereas the viscoplastic terms are defined through its secant viscosity, as

$$\dot{U}_1^{vp} = 3\eta_1^s \cdot (\dot{\bar{\epsilon}}_e^{vp(1)})^2, \quad \dot{U}_0^{vp} = 3\eta_0^s \cdot (\dot{\bar{\epsilon}}_e^{vp(0)})^2. \quad (5.25)$$

Now setting eq. (5.23) equal to eq. (5.24), we have the work-rate equality

$$c_1[\dot{U}_1^e + 3\eta_1^s \cdot (\dot{\mathcal{E}}_e^{vp(1)})^2] + c_0[\dot{U}_0^e + 3\eta_0^s \cdot (\dot{\mathcal{E}}_e^{vp(0)})^2] = \eta_\kappa^s (\dot{\mathcal{E}}_{kk})^2 + 2\eta_\mu^s \dot{\mathcal{E}}_{ij}^s \dot{\mathcal{E}}_{ij}^s. \quad (5.26)$$

Since this equality holds for any  $\dot{\mathcal{E}}_{ij}^s$ ,  $\kappa_r$ ,  $\mu_r$ ,  $\eta_1^s$  and  $\eta_0^s$ , the boundary condition and the elastic constants can be kept fixed and only one of the secant viscosities can be varied. Taking derivative with respect to  $\eta_1^s$  and  $\eta_0^s$  separately, the effective viscoplastic strain rate of the constituent phases in terms of the applied strain rate can be obtained as

$$\dot{\mathcal{E}}_e^{vp(1)} = \left[ \frac{1}{c_1} \left( \frac{1}{3} \frac{\partial \eta_\kappa^s}{\partial \eta_1^s} (\dot{\mathcal{E}}_{kk})^2 + \frac{\partial \eta_\mu^s}{\partial \eta_1^s} \dot{\mathcal{E}}_e^2 \right) \right]^{1/2}, \quad (5.27a)$$

$$\dot{\mathcal{E}}_e^{vp(0)} = \left[ \frac{1}{c_0} \left( \frac{1}{3} \frac{\partial \eta_\kappa^s}{\partial \eta_0^s} (\dot{\mathcal{E}}_{kk})^2 + \frac{\partial \eta_\mu^s}{\partial \eta_0^s} \dot{\mathcal{E}}_e^2 \right) \right]^{1/2}, \quad (5.27b)$$

where,  $\dot{\mathcal{E}}_e^2 = (2/3) \dot{\mathcal{E}}_{ij}^s \dot{\mathcal{E}}_{ij}^s$ . These effective rates serve to determine the secant viscosities  $\eta_1^s$  and  $\eta_0^s$  by eq. (5.10). A detailed derivation for the four partial derivatives in eqs. (5.27a) and (5.27b) is given in Appendix A5.

## 5.5 Porosity change and the incremental scheme

The porosity will continue to evolve during plastic flow. The change of porosity, or  $\dot{c}_2$ , is related to the difference between its dilatational strain-rate and the overall applied dilatational rate. Denoting the volume of voids by  $V_2$  and that of the overall composite by  $V$ , it is given by

$$c_2 = \frac{V_2}{V}, \text{ or } \dot{c}_2 = \frac{\dot{V}_2}{V} - \frac{V_2 \dot{V}}{V^2} = c_2 (\dot{\mathcal{E}}_{kk}^{(2)} - \dot{\mathcal{E}}_{kk}), \quad (5.28)$$

where the dilatational rate of the voids,  $\dot{\mathcal{E}}_{kk}^{(2)}$ , is found to be,

$$\dot{\bar{\epsilon}}_{kk}^{(2)} = \left\{ B - pre^{-rt} \left[ \cos wt + \frac{q-r}{w} \sin wt \right] + pe^{-rt} [-w \sin wt + (q-r) \cos wt] \right\} \dot{\bar{\epsilon}}_{kk}. \quad (5.29)$$

The derivation and constants  $B, p, r, q$  and  $w$  are given in Appendix A6.

Due to the continuous change of porosity and secant viscosity of the constituent phases, an incremental scheme should be used for computation. That is, in general,

$$\bar{\sigma}_{kk}(t + \Delta t) = \bar{\sigma}_{kk}(t) + \dot{\bar{\sigma}}_{kk} \Delta t, \quad \bar{\sigma}_{ij}(t + \Delta t) = \bar{\sigma}_{ij}(t) + \dot{\bar{\sigma}}_{ij} \Delta t. \quad (5.30)$$

The stress rates can be calculated from eq. (5.22), as

$$\dot{\bar{\sigma}}_{kk}(t) = 3\dot{\eta}_{\kappa}^s(t) \dot{\bar{\epsilon}}_{kk}, \quad \dot{\bar{\sigma}}_{ij}(t) = 2\dot{\eta}_{\mu}^s(t) \dot{\bar{\epsilon}}_{ij}, \quad (5.31)$$

with the effective secant-viscosity rates

$$\dot{\eta}_{\kappa}^s = \kappa_0 \left\{ -pre^{-rt} [\cos(wt) + \frac{q-r}{w} \sin(wt)] + pe^{-rt} [-w \sin(wt) + (q-r) \cos(wt)] \right\}, \quad (5.32a)$$

$$\begin{aligned} \dot{\eta}_{\mu}^s = & T_0(\eta_0 - \delta)e^{-T_0 t} + E\{F_1 \lambda_1 e^{\lambda_1 t} + a_1 e^{a_1 t} [(F_2 + F_3) \cos(b_1 t) + (F_2 - F_3) \sin(b_1 t)] \\ & + e^{a_1 t} [-(F_2 + F_3)b_1 \sin(b_1 t) + (F_2 - F_3)b_1 \cos(b_1 t)]\} \end{aligned} \quad (5.32b)$$

The values of  $\delta, E, F_1, F_2, F_3, \lambda_1, a_1$  and  $b_1$  are also listed in Appendix A6.

At  $t=0$ , the response is elastic, and the initial rates  $(3\dot{\eta}_{\kappa}^s, 2\dot{\eta}_{\mu}^s)$  are exactly equal to the effective bulk and shear moduli  $(3\kappa, 2\mu)$  of the composite given by eq. (5.11). Using this, the incremental stress  $\Delta \bar{\sigma}_{ij}$  is calculated from the incremental strain  $(\Delta \bar{\epsilon}_{ij} = \dot{\bar{\epsilon}}_{ij} \Delta t)$  for the first time increment, and then eq. (5.13) is used to obtain the initial stress redistribution among the constituent phases. The unified constitutive equations then provide the effective viscoplastic strain rates  $\dot{\epsilon}_e^{vp(r)}$  from eq. (5.5), and the secant viscosities from eq. (5.10). For the subsequent steps, the main aim is to calculate the stress rates from eq. (5.31), in conjunction with eq. (5.32).

The parameters  $p, q, r, \dots$  etc., involve the term  $T_r$  ( $T_r = \mu_r / \eta_r^s$ ) which requires the value of  $\eta_r^s$  at the current time level. Equation (5.10) is used to find  $\eta_r^s$  at the present time step. The values of  $\dot{\varepsilon}_e^{vp(r)}$  needed in eq. (5.10) are calculated from the field fluctuation theory [eq. (5.27)]. In the calculation of the four partial derivatives, the value of  $\eta_r^s$  is taken from the previous time step. Once the stress at the next time level and the values of  $\eta_r^s$  for the current time step are obtained, the calculation for the next time level, with the porosity also updated, can proceed in the same way. This procedure is repeated until the entire stress-strain curve is determined.

### **5.6 Application to the rate-dependent behavior of porous nanocrystalline iron, and iron-copper mixture**

The developed incremental model is applied to investigate the competition of grain size and porosity in the viscoplastic behavior of nanocrystalline iron, and iron-copper mixture. Khan et al. [48], Khan and Zhang [49], and Khan et al. [50] have conducted a series of experiments to uncover the strain-rate sensitivity of these materials. Their processing technique involves the high energy ball milling and high temperature sintering. Certain amounts of porosity are found in Fe and Fe80Cu20 (wt %). The lattice constant of iron is 0.287 nm, and assuming that the GBAZ spans over about 10 atomic spacing, we take  $t = 3$  nm, as was done for nickel by Li and Weng [32]. The viscoplastic material constants of iron, and iron-copper mixture used in the calculations for the grain interior and the GBAZ of iron and iron-copper mixture have been obtained by inverse simulation of the test data and are listed in Tables 5.1 and 5.2 (provided at the end of the chapter), respectively. Following Schwaiger et. al. [33], the elastic properties of GBAZ and grain interior were taken to be identical. This choice was, in part, prompted from observation of a high resolution image by scanning transmission electron microscopy (STEM), which disclosed that crystallinity of the grain in Ni was maintained right up to the grain boundary (Kumar et al. [51]). The thickness of GBAZ spans over the outer region of the grain and includes only a very thin

portion – perhaps about 2-3 atomic spacing – of the grain boundary. But since the elastic property of the grain boundary may be harder or softer than the grain, the moduli of GBAZ and grain interior are not strictly equal. Such elastic heterogeneity can be accommodated in eq. (5.11).

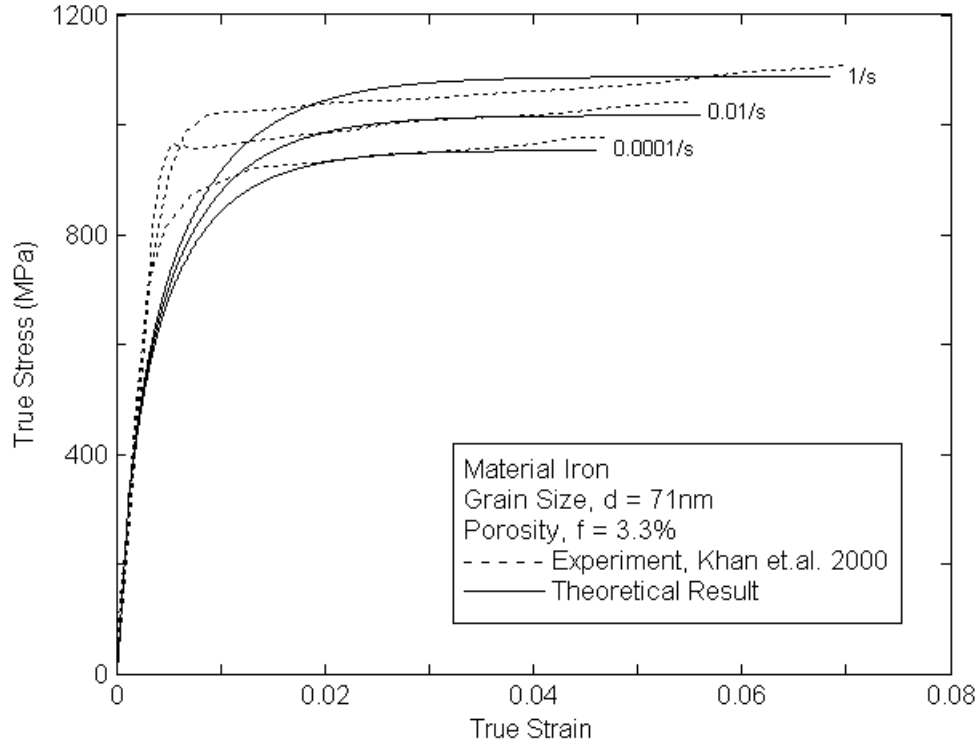


Fig 5.2: Comparison between the experimental and theoretically obtained true stress strain relations under uniaxial compressive loading for nanocrystalline iron with a grain size of 71nm, porosity ( $f$ ) 3.3% and three different strain rates of 0.0001/s, 0.01/s and 1/s.

At first the strain-rate sensitivity of a nanocrystalline, porous iron is calculated. The initial porosity of iron tested was found to span over about 3-7%. Their experimental data at the grain size of  $d = 71\text{ nm}$  under the constant strain rates of  $\dot{\epsilon}_{11} = 0.0001/\text{s}$ ,  $0.01/\text{s}$ , and  $1/\text{s}$ , are reproduced in Fig. 5.2 (from Fig. 6 of Khan et al. [48]). Within the allowable porosity range, we chose  $c_2 = 0.033$  in the calculation. The calculated curves based on the 3-phase composite model are depicted as solid lines here. Both experiments and theoretical results indicate a clear strain-rate sensitivity of the nanocrystalline iron. A direct comparison between the two sets of curves

indicates a noticeable discrepancy in the early stage of plastic deformation, but the final saturation state is in good overall agreement. This initial discrepancy was caused by the *power-law* form of the unified constitutive equations, which is not as stiff as Khan's experimental data. Better agreement is possible if a stiffer form of constitutive equation, such as an exponential one, is adopted.

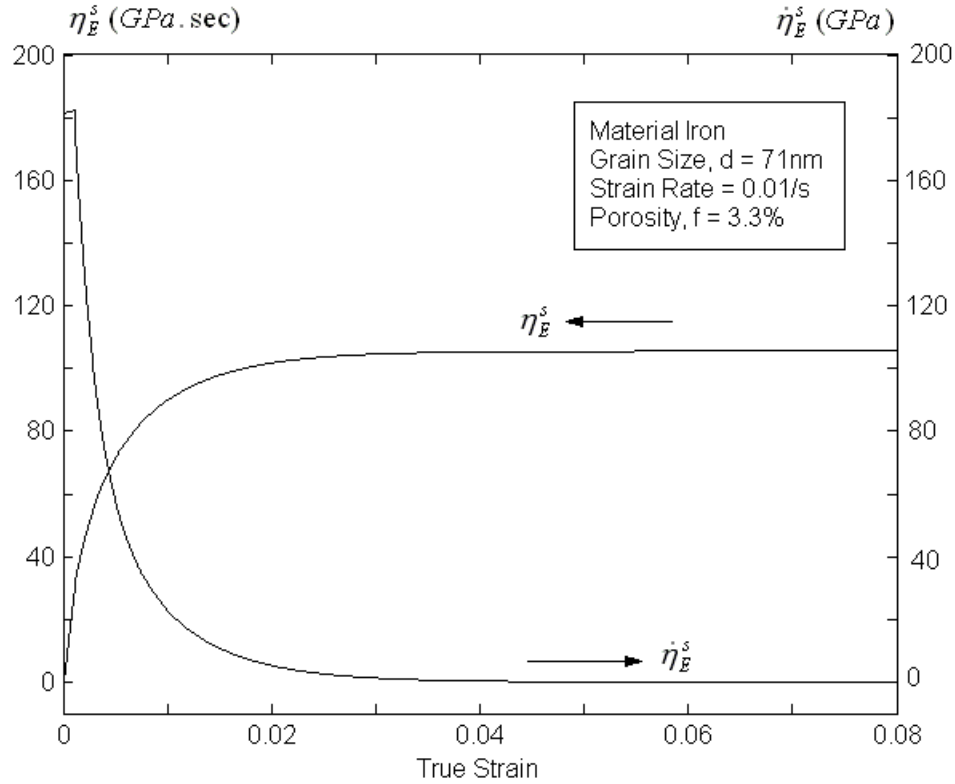


Fig. 5.3 Change of the effective secant viscosity and its rate in the course of deformation. The right scale for the viscosity rate is numerically identical to the left one.

The non-Newtonian nature of viscoplastic flow under a constant strain-rate loading is reflected through the change of effective secant viscosities ( $\eta_\kappa^s, \eta_\mu^s$ ) in eq. (5.22), or their rates ( $\dot{\eta}_\kappa^s, \dot{\eta}_\mu^s$ ) in eqs. (5.32a and b). To illustrate such changes, the functions  $\eta_E^s$  and  $\dot{\eta}_E^s$  for the uniaxial loading are shown in Fig. 5.3, for the strain rate of 0.01/s, in the above case. The effective secant viscosity  $\eta_E^s$  essentially is the true stress scaled by the applied strain rate and, just like the stress itself, it

starts from zero, then increases rapidly, and eventually reaches a saturation value. The effective viscosity rate  $\dot{\eta}_E^s$  on the other hand represents the tangent modulus of the stress-strain curve; it starts from the effective Young's modulus  $E$  of the 3-phase composite, then decreases rapidly, and eventually approaches zero at saturation.

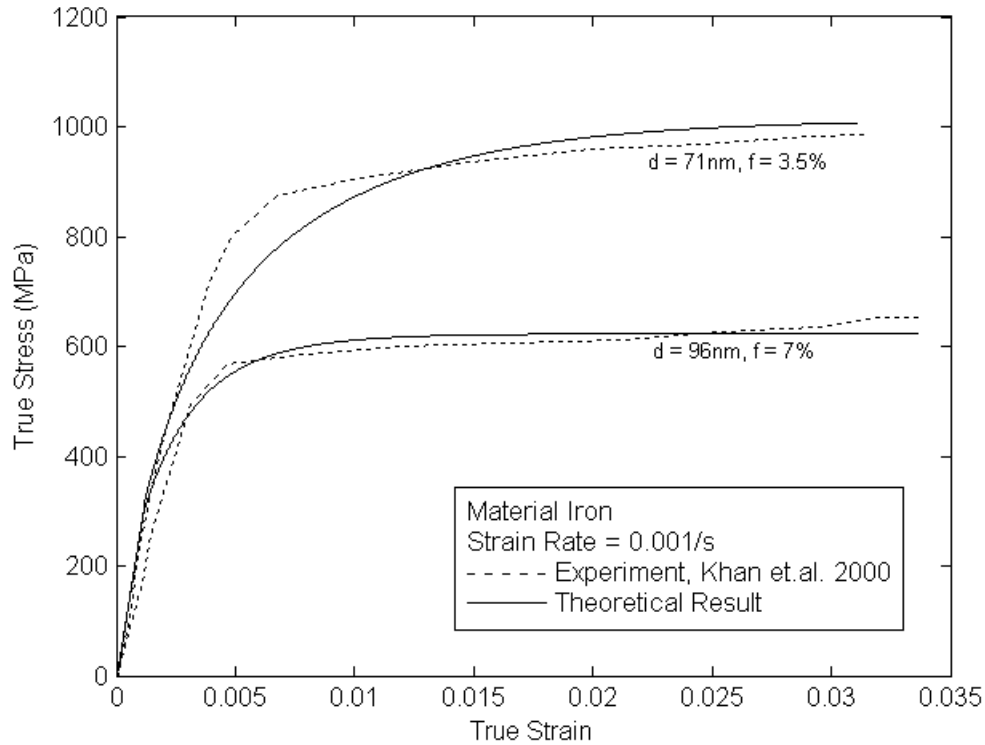


Fig 5.4: Comparison between the experimental and theoretically obtained true stress strain relations under uniaxial compressive loading for nanocrystalline iron at a particular strain rate of 0.001/s with a grain size of 71nm and 96nm along with porosity ( $f$ ) of 7% and 3.5% respectively.

Khan et al. [48] have also conducted a dynamic test at the high rate of 3,500/s. The adiabatic condition involved would lead to a significant temperature increase and thermal softening. As incorporation of such thermal effects was not the main concern in this development it was not attempted to make a comparison there.

We then examined the effect of grain size as it decreases from 96 nm to 71 nm in Fig. 5.4, which corresponds to a strain-rate test of 0.001/s. The experimental data is reproduced from Fig.

8 of Khan et al. [48], whereas the calculated curves are shown in solid lines, using the initial porosity of 7% and 3.5%, respectively. There is a clear strengthening effect as the grain size decreases in this nano-meter range.

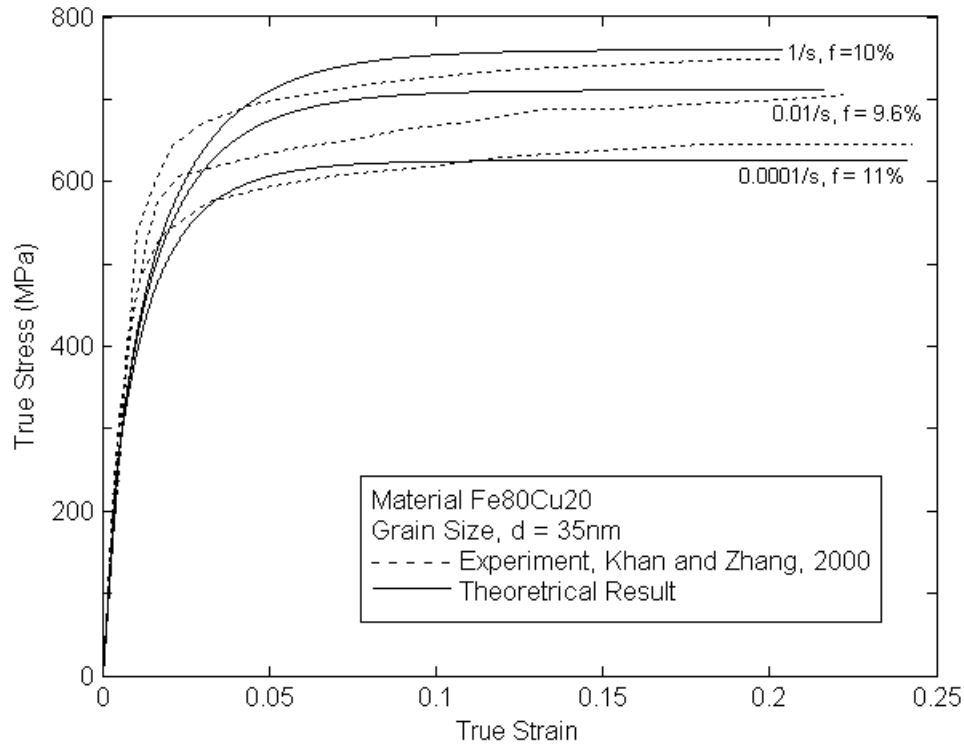


Fig. 5.5 Comparison between the experimental and theoretically obtained true stress strain relations under uniaxial compressive loading for nanocrystalline Fe<sub>80</sub>Cu<sub>20</sub> with a grain size of 35nm and three different strain rate of 0.0001/s, 0.01/s and 1/s along with different porosity ( $f$ ) of 11%, 9.6% and 10% respectively.

The condition of simultaneous change of porosity and strain-rate was tested by Khan and Zhang [49] for a nanocrystalline Fe<sub>80</sub>Cu<sub>20</sub> mixture, with the average grain size of 35 nm. The test data, reproduced from Fig. 3 (of ref. [49]), is shown in Fig. 5.5 as dashed lines. This data covers the strain rates of 0.0001/s, 0.01/s, and 1/s, with the initial porosities of 11%, 9.6%, and 10%, respectively. The calculated results are shown as solid lines. Overall agreement seems to be reasonable. But agreement at large strain, say beyond 10%, must be read with caution as our theory is based on infinitesimal strain.

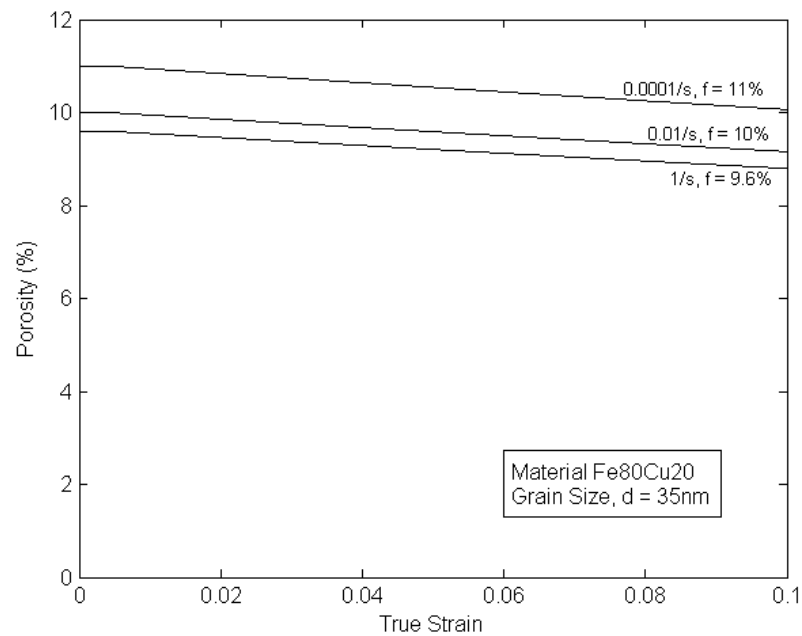


Fig 5.6: Change of porosity with strain for the Fe80Cu20 alloy at different strain rates and different initial porosities but a constant grain size.

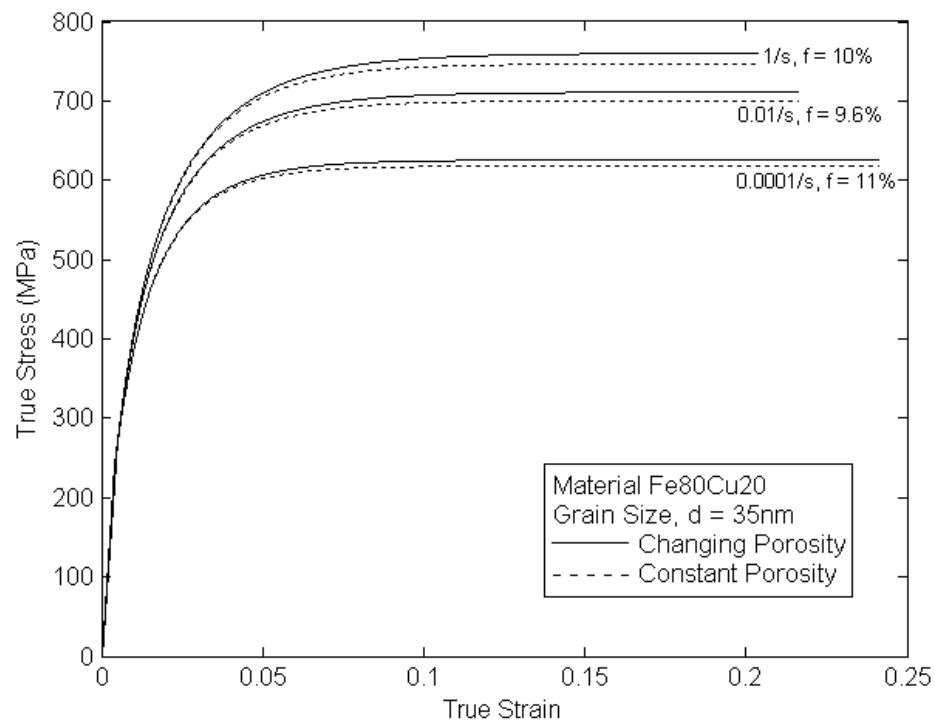


Fig 5.7: Comparison between the stress-strain plot of Fe80Cu20 alloy with constant porosity and variable porosity. The plot with variable porosity shows a little bit of strain hardening even after reaching the saturation strength. But the constant porosity curve does not show any strain hardening after reaching the saturation level.

The preceding results have all been calculated with an evolving porosity. Since the initial porosities in Fig. 5.5 are much higher than those in Figs. 5.2 and 5.4, it is instructive to show how the porosity changes in this case. Fig. 5.6 illustrates the decrease of porosity under compression. At the end of 10% strain, the normalized porosities have decreased to about 0.92 in all three cases. This compares well with the value of 0.91 in the compression test of Spitzig et al. [52] on iron compacts. It is also interesting to see the difference of predictions if the porosity change is ignored altogether; this is illustrated in Fig. 5.7. Clearly the decrease of porosity under compression has led to a harder response.

In order to demonstrate that the model can deliver the nonlinear dilatational response of the porous nanocrystalline solid even if  $E_1 = E_0$ , calculations have been done using the properties of Fe80Cu20 with the grain size of 35 nm as porosity increases from 0% to 10%. The results are shown in Fig. 5.8(a), under the constant dilatational rate of  $\dot{\bar{\epsilon}}_{kk} = 0.01/\text{s}$ . The  $\bar{\sigma}_{kk}$  versus  $\bar{\epsilon}_{kk}$  curve is seen to be linear in the absence of porosity, but becomes increasingly nonlinear as porosity increases. Even without porosity, this model can also deliver the nonlinear dilatational behavior under a constant dilatational rate. This is demonstrated in Fig. 5.8(b), based on the properties of Fe80Cu20 but varying its  $E_1$ . The nonlinearity is seen to increase progressively as the elastic stiffness of inclusions decreases. This trend is consistent with the exact analysis of Qiu and Weng [14] for the rate-independent plasticity.

Many molecular dynamic simulations, such as Schiotz et al. [23], Lund and Schuh [24], have revealed that, as the grain size decreases to a very small nano-meter range, nanocrystalline metals could become softer. While the experiments of Khan et al. [48], Khan and Zhang [49], and Khan et al. [50] did not go down to such a small grain size, the developed model was used to make a speculative calculation, to see how the properties of the porous, nanocrystalline solids would change within such a range of grain size. Fig. 5.9 displays the calculated stress-strain curves of

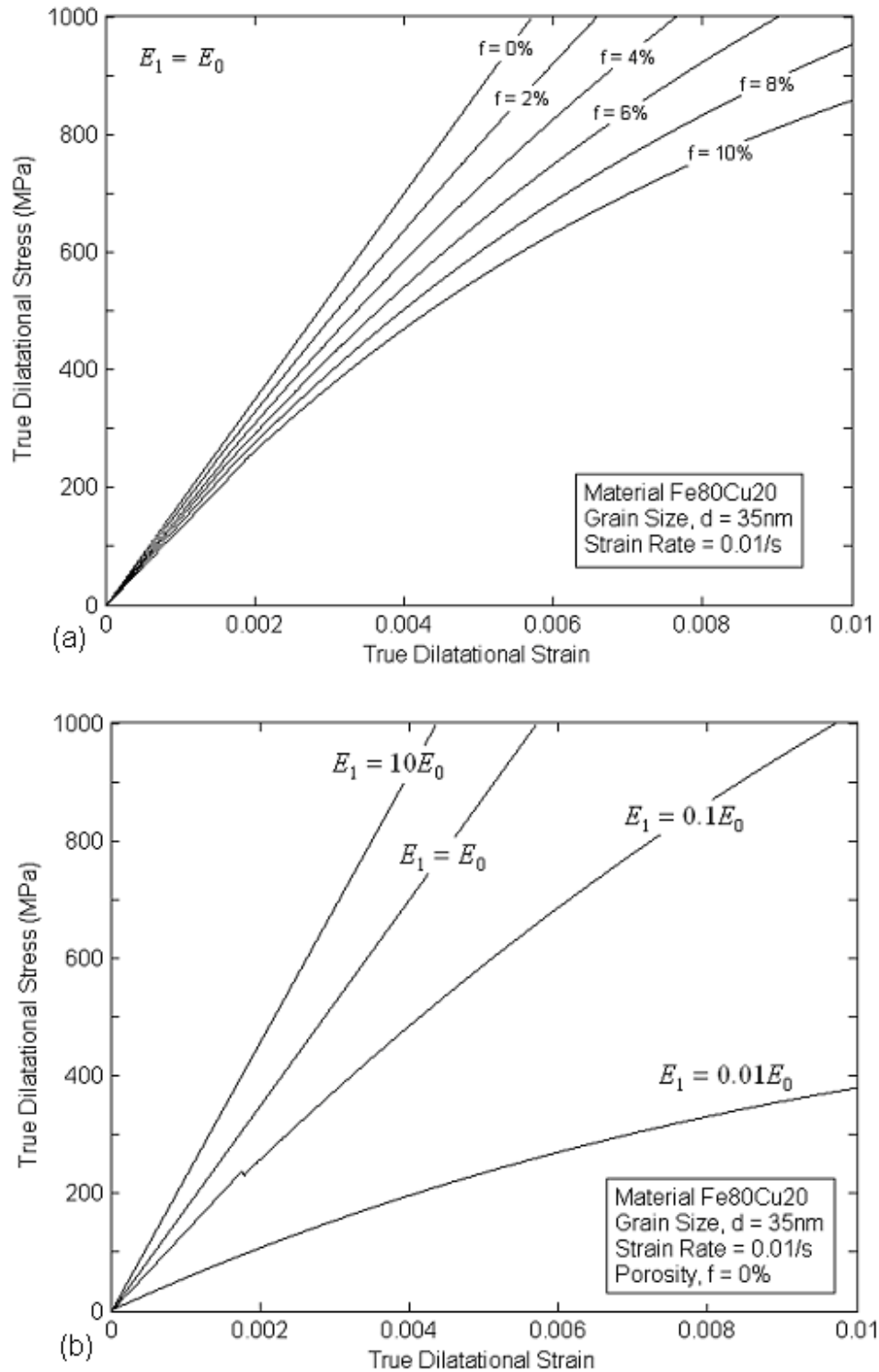


Fig 5.8: (a) Plot of true dilatational stress vs. strain under dilatational constant strain rate (0.01/s) loading for nanocrystalline Fe80Cu20 with a constant grain size of 35nm and different porosities. (b) Plot of true dilatational stress vs. true dilatational strain for Fe80Cu20 alloy with different elastic modulus for grain interior and GBAZ for a 35nm grain size and 0.01/s strain rate but no porosity.

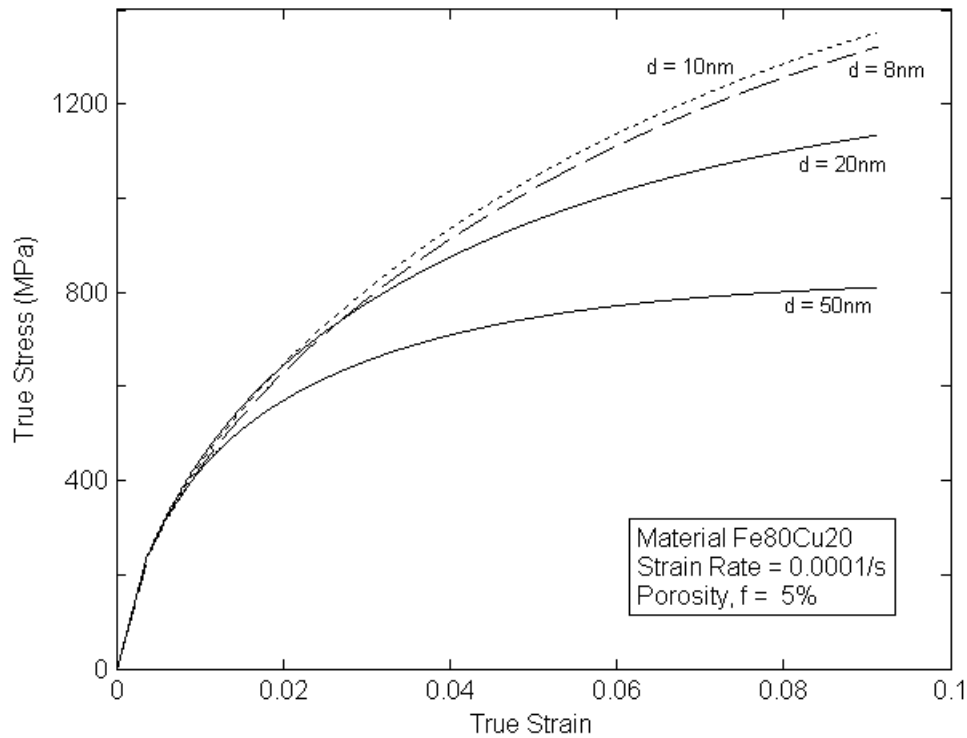


Fig. 5.9 True stress-strain plot of nanocrystalline Fe<sub>80</sub>Cu<sub>20</sub> under compressive constant strain rate loading of 0.0001/s with a porosity of 5% at different grain size (diameter, d) to demonstrate its potential softening at very small grain size due to increased contribution from the GBAZ.

Fe<sub>80</sub>Cu<sub>20</sub> at the porosity of 5% under the strain rate of 0.0001/s as the grain size decreases from 50 nm to 8 nm. For the four selected grain sizes, the nanocrystalline metal is seen to continue to strength as the grain size decreases from 50 nm to 10 nm, but from 10 nm to 8 nm, there is an apparent dip in the overall response. These calculations were made assuming that the grain interior continues to obey the Hall-Petch equation, but it is possible that dislocations have ceased to operate before the grain size decreases to 8 nm, and, in that case, the softening behavior would have appeared even earlier. For copper, such a critical grain size was estimated to be about 8.2 nm and for palladium, it was about 11.6 nm according to Wang et al. [26]. The 2% yield stresses are shown in the Hall-Petch plot in Fig. 5.10, this time with several levels of porosity. While porosity does cause the yield strength to decrease, it does not alter the fundamental nature of

transition for the yield stress. These plots all point to the continuous increase, level off, and eventual decline of the yield strength, with the maximum occurring at about 16 nm.

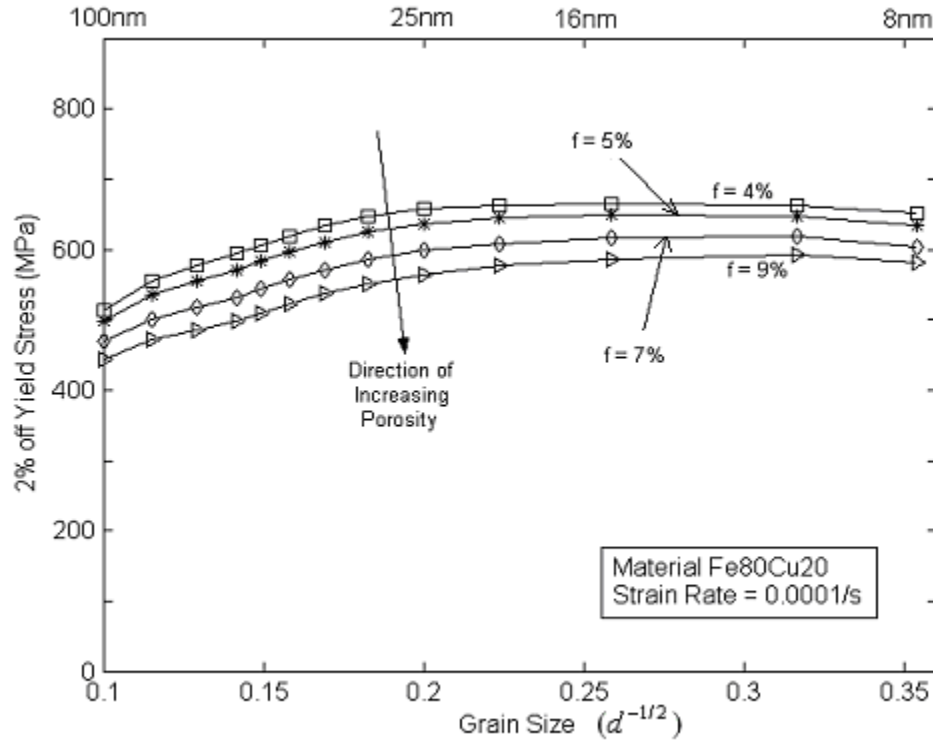


Fig. 5.10 Hall-Petch plot of nanocrystalline Fe<sub>80</sub>Cu<sub>20</sub> at a constant strain rate loading of 0.0001/s with different porosities of 4%, 5%, 7% and 9%.

The sensitivity of the GBAZ parameters on the nature of Hall-Petch transition is an important issue, and this is investigated in two ways here. We first changed its Young's modulus while maintaining its viscoplastic constants, and then changed its saturation stress while keeping its Young's modulus unaltered. The corresponding results are shown in Fig. 5.11(a) and 5.11(b), respectively, with the middle curve representing the original state. Both figures suggest that, as the GBAZ becomes softer, the critical grain size at which the material attains its highest yield strength moves to the left; conversely when it becomes harder, it moves to the right. The underlying reason for such kind of shift is due to the competition between the deformation of grain interior and GBAZ. When the slope of the Hall-Petch plot is positive, the overall

deformation is mainly contributed by the grain interior and when it is negative, the GBAZ dominates the overall deformation (Jiang and Weng [27]). Capolungo et al. [30, 31] have argued a transition from dislocation glide to grain boundary mediated mechanisms (e.g. dislocation nucleation and absorption from grain boundary surface and ledges) during this change. Their arguments are consistent with this observation, both indicating a more dominant role played by the latter as grain size decreases to the nano-meter scale. So if the properties of GBAZ becomes softer, such a critical state can be reached without having to reduce the grain size to the same small value, leading to a shift to the left in the Hall-Petch plot. The precise amount of shift, however, has to be calculated.

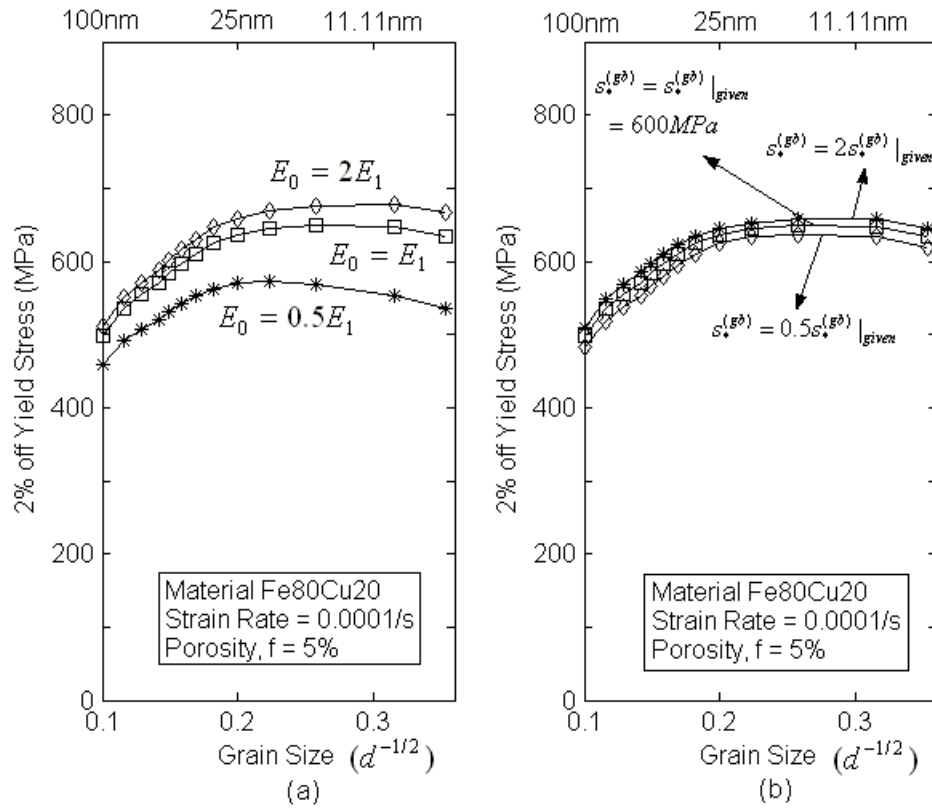


Fig 5.11: Hall-Petch plot for Fe80Cu20 alloy with different elastic modulus for grain interior and GBAZ. Here  $E_0$  signifies the Young's modulus of the GBAZ and  $E_1$  signifies the Young's modulus of the grain interior region. From the plot it is very clear that the grain size at which the reverse Hall-Petch effect start depends on the difference in the elastic modulus of grain interior and the GBAZ.

In order to show the influence of porosity on the behavior of Fe and Fe80Cu20 more fully, in Fig. 5.12 the corresponding curves to Figs. 5.2, 5.4 and 5.5, assuming no porosity has been plotted. Both Figs. 5.12(a) and (b) show a clear increase of flow stress, and the increase in Fig. 5.12(c) is more pronounced for the initial porosities in Fig. 5.5 are substantially higher.

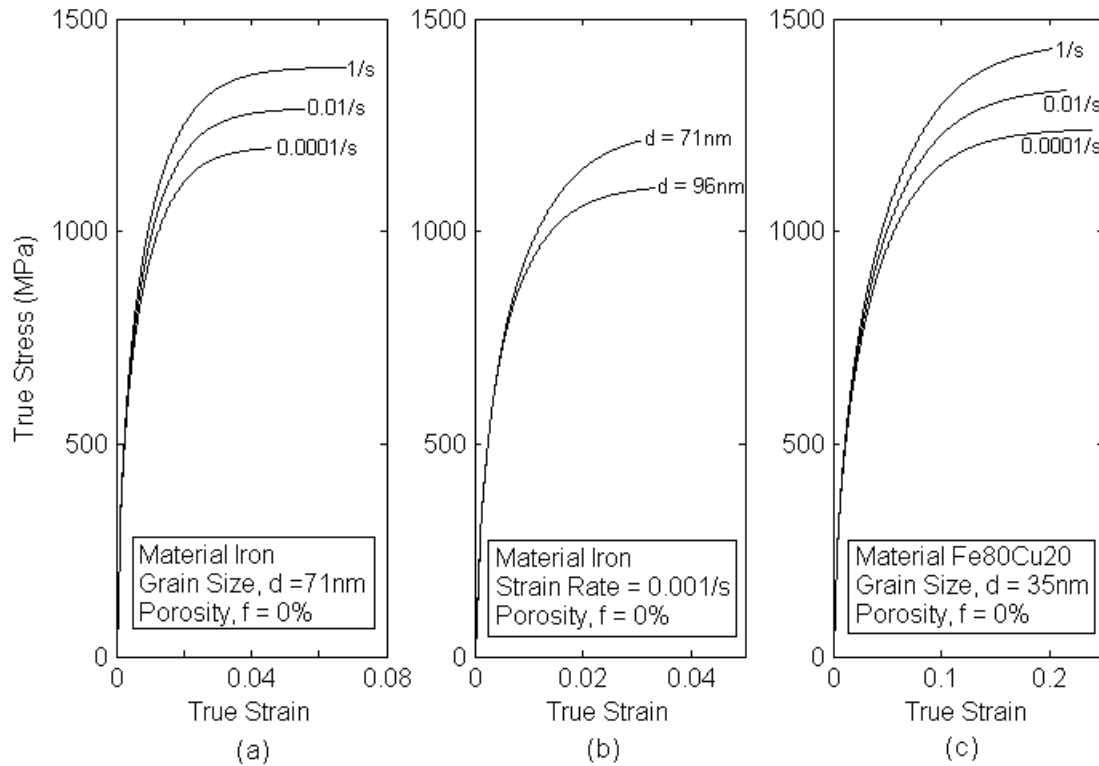


Fig. 5.12 Three corresponding plots to Fig. 5.2, 5.4, and 5.5 with zero porosity.

While the above results have shown the effects of grain size and porosity, their competition perhaps can be best illustrated in Figs. 5.13 and 5.14, calculated for Fe80Cu20 and iron, respectively. In the case of Fe80Cu20, increasing the initial porosity from 2% to 10% would give an almost opposite trend to decreasing the grain size from 70 nm to 30 nm. Similar trend is observed for Fe from the initial porosity of 4% to 8%, as opposed to the grain size of 110 nm to 55 nm.

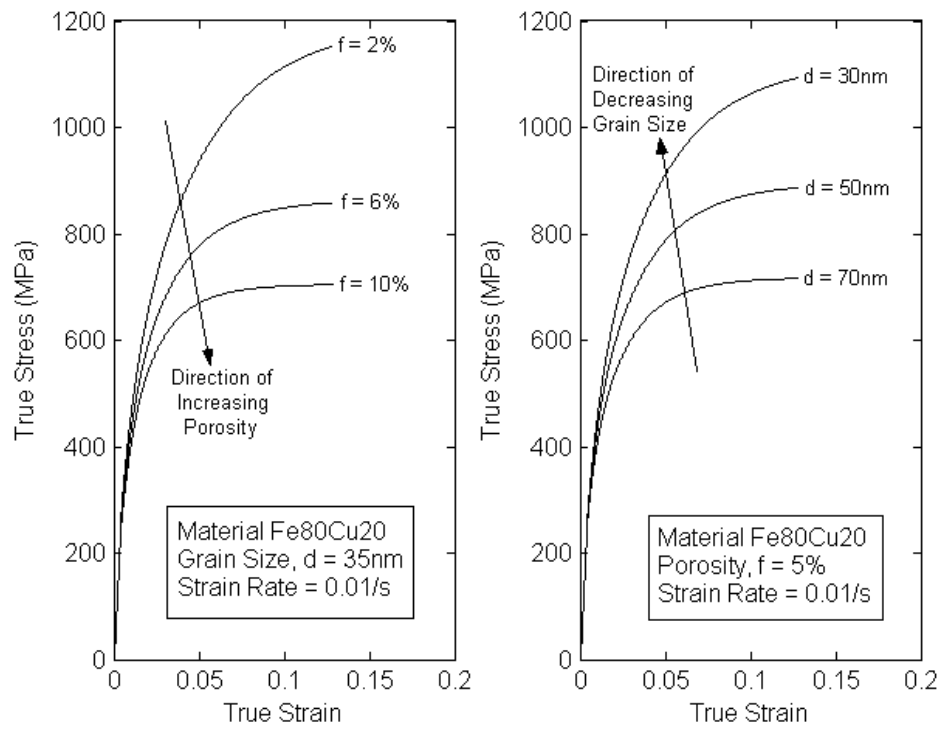


Fig 5.13: Competition between the grain size and porosity for a Fe<sub>80</sub>Cu<sub>20</sub> alloy at a strain rate of 0.01/s.

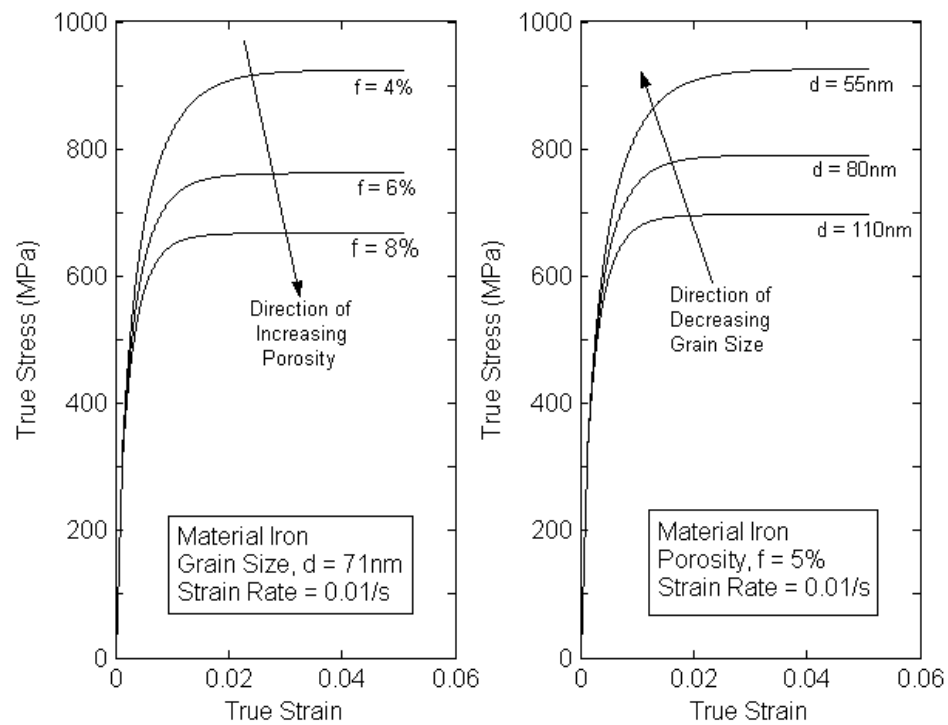


Fig 5.14: Competition between the grain size and porosity for iron at a strain rate of 0.01/s.

This completes our examination on the issues of grain size versus porosity in the viscoplastic response of porous, nanocrystalline solids. However, the noticeable discrepancy between the theory and experiment in the initial elastic response of Fig. 5.4 for the porosity of 7% remains a concern. While the effect of porosity on the reduction of elastic moduli has been examined in Weng [10] (Fig. 6) for a void/epoxy and a 3-phase quartz sand/void/epoxy with reasonable agreement with experiments, we decided to test it again for the metallic systems. Fig. 5.15 (a) and 5.15(b) are comparisons with the test data of Spitzig et al. [52] for iron compacts, and Khan and Zhang's [49] data for Fe80Cu20, respectively. The agreement in the former case is about the same as in the epoxy systems, but the large difference in the latter case apparently requires further study.

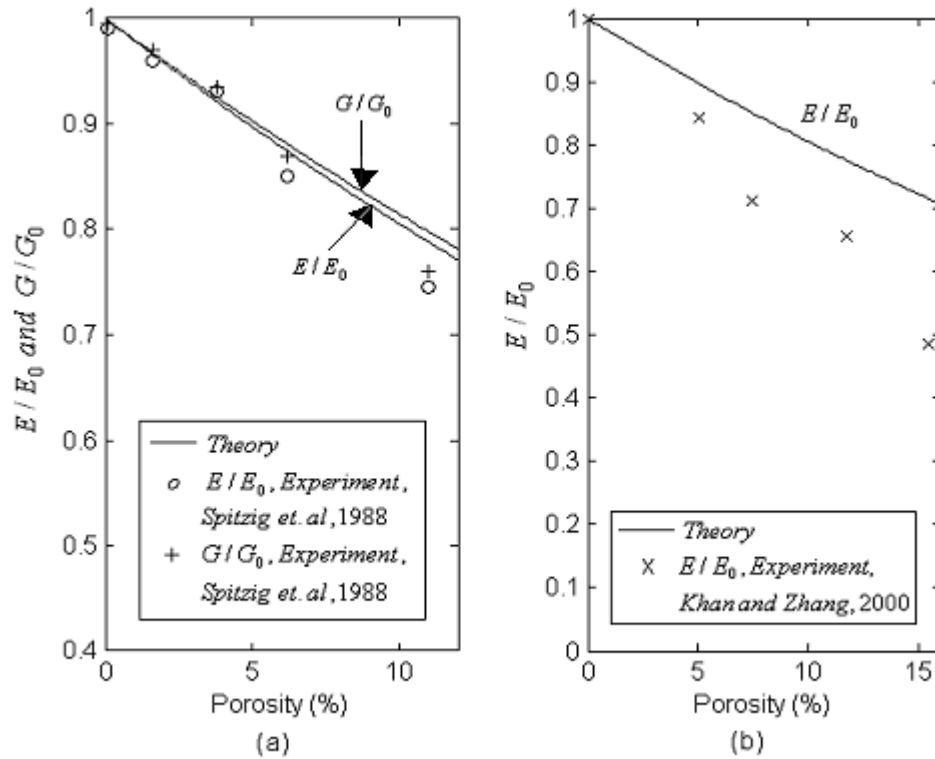


Fig. 5.15 Reduction in elastic moduli with increasing porosity. A comparison with the experimental data of Fe compacts (Spitzig et. al. [52]) and Fe80Cu20 (Khan and Zhang, [49]).

Finally to place the present approach in perspective in relation to the recent one of Li and Weng [32], we made a last comparison between the two for a two-phase composite. In the previous model developed by Li and Weng [32], to determine the viscoplastic response, the elastic moduli of the individual phases were replaced by the secant viscosity of each phase in the expression of the overall elastic moduli of the composite. No Laplace transform was used to derive the viscoelastic response. Keeping in mind that this earlier model was intended only for the case of  $E_1 \geq E_0$  (or slightly less than  $E_0$ , but certainly not for voids), the comparison was done here for a fully compact nanocrystalline iron using the properties listed in Table 5.1. The results, shown in Fig. 5.16, have been calculated to a fairly large strain in order to reveal a full range of deformation. It is seen that the initial transition from elastic to viscoplastic response takes place earlier in the previous model, but the subsequent flow follows an essentially identical path.

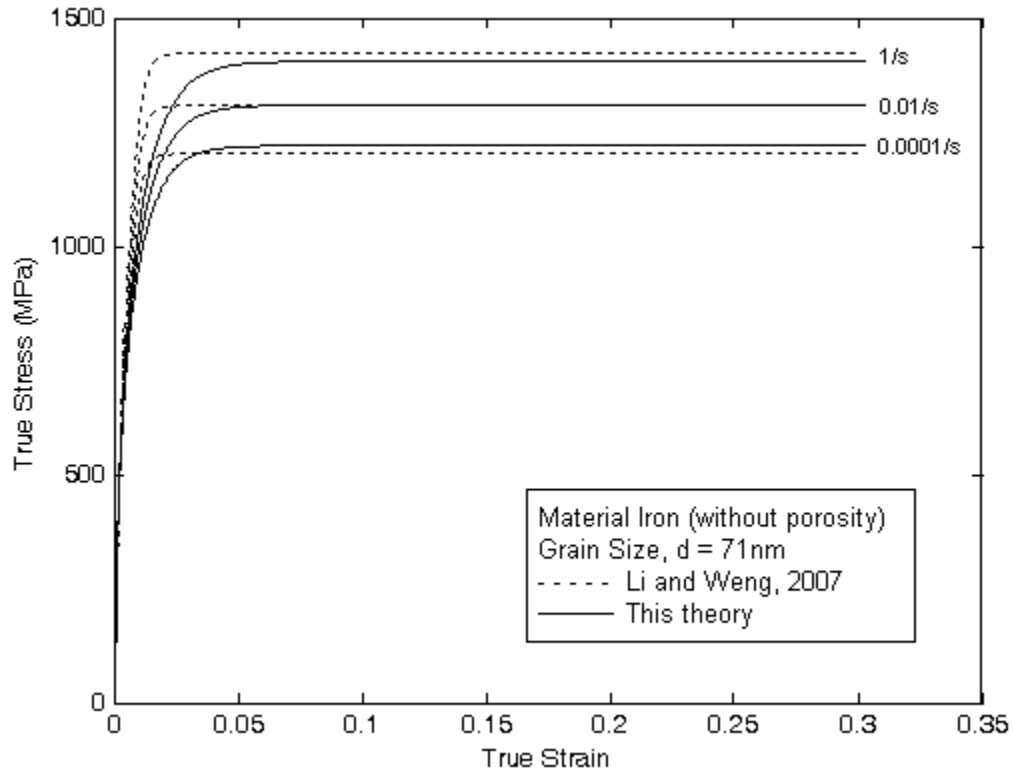


Fig. 5.16 Comparison of the two theories for a grain size of 71nm without porosity under different strain rates.

**Table 5.1: Material parameters used in calculations for iron**

|                                       | Grain Interior | Grain Boundary Affected Zone (GBAZ) |
|---------------------------------------|----------------|-------------------------------------|
| $E$ (GPa)                             | 210.0          | 210.0                               |
| $\nu$                                 | 0.3            | 0.3                                 |
| $s_0^\infty$ (MPa)                    | 5.03           | -----                               |
| $k$ (GPa $\sqrt{nm}$ )                | 4.25           | -----                               |
| $a$                                   | 1.1            | -----                               |
| $s_0$ (MPa)                           | -----          | 320                                 |
| $s_*$ (MPa)                           | -----          | 600                                 |
| $h$ (MPa)                             | 1              | 1.5                                 |
| $n$                                   | 220            | 120                                 |
| $\dot{\epsilon}_0$ ( $10^{-4} / hr$ ) | 1.0            | 1.0                                 |

**Table 5.2: Material parameters used in calculations for Fe80Cu20 material**

|                                      | Grain Interior | Grain Boundary Affected Zone (GBAZ) |
|--------------------------------------|----------------|-------------------------------------|
| $E$ (GPa)                            | 70.0           | 70.0                                |
| $\nu$                                | 0.3            | 0.3                                 |
| $s_0^\infty$ (MPa)                   | 5.1            | -----                               |
| $k$ (GPa $\sqrt{nm}$ )               | 1.8            | -----                               |
| $a$                                  | 1.5            | -----                               |
| $s_0$ (MPa)                          | -----          | 255                                 |
| $s_*$ (MPa)                          | -----          | 600                                 |
| $h$ (MPa)                            | 10             | 9                                   |
| $n$                                  | 120            | 60                                  |
| $\dot{\epsilon}_0$ ( $10^{-4}$ / hr) | 1.0            | 1.0                                 |

## Chapter 6

### Conclusions and future work

#### 6.1 Conclusion

Investigation of the creep response and strain-rate sensitivity of nanocrystalline materials has been conducted. A two phase composite model has been developed to analyze the creep resistance and a three phase (the third phase acts as voids/pores within the solid) composite for the strain-rate sensitivity of the porous nanocrystalline material. In both models the inclusions represent the plastically harder grain interior and the matrix represents the plastically softer grain boundary affected zone (GBAZ). For the three phase model the third phase represents the voids. The drag stress of the grain interior is considered to be grain-size dependent whereas the properties of the grain boundary affected zone is completely independent of the grain size. The pores/voids (in the three phase composite) do not have any elastic or secant modulus.

For the two phase model developed to characterize the creep resistance, the creep rate of each phase is described by a unified constitutive equation that can account for the effect of stress, strain-hardening and temperature. A homogenization method based on the concept of secant viscosity and field fluctuation is finally developed to evaluate the evolution of overall creep strain. In this work, the focus has been to study the transition of creep resistance of nanocrystalline materials as the grain size decreases to the nanometer range. The critical grain size,  $d_{crit}$ , at which the material has maximum creep resistance has also been determined in this study. The increase of creep resistance is attributed to the decrease of grain size through the Hall-Petch effect, but continuous decrease of grain size would increase the presence of the softer grain boundary affected zone and this in turn could result in the softening effect of the nanocrystalline solid. There is a subtle balance between the grain size and GBAZ that must be dealt with

carefully. When creep resistance is plotted against the inverse of the square root of grain size,  $d^{-1/2}$ , the transition starts with a positive slope, then zero, and finally to a negative slope. The variation reflects the intricate competition of the grain interior and GBAZ toward the overall creep strength of the material. It turns out that the optimal grain size of the high-temperature creep resistance always occurs at the nanometer range, but the precise size for a given material needs to be calculated.

In case of the three phase model developed to investigate the strain-rate sensitivity of the porous nanocrystalline material, both the grain interior and the GBAZ are described by a unified constitutive law which takes into account the effect of stress and strain hardening. The viscoplastic state of both constituent phases is characterized by its secant-viscosity, which continues to evolve in the course of plastic deformation. To develop the homogenization scheme for the nonlinear viscoplastic response, the secant-viscosities are implemented into a linear viscoelastic one to replace the corresponding linear viscosities of the constituent phases. The required secant-viscosities of the constituent phases are in turn evaluated from their viscoplastic strain rates derived from a field-fluctuation approach. The developed theory has been applied to obtain the viscoplastic response of nanocrystalline materials under various concentrations of porosities at different grain sizes under different strain rates. The predicted results were compared with the experimental data developed by Khan et al. [48 – 50]. These calculations display the intricate nature of competition among the grain size, porosity and loading rate. The evolution of porosity during the plastic flow has been revealed, and the plastic compressibility of the nanocrystalline solid, with as well as without porosity has been examined. The calculation has also been pushed to smaller grain sizes that were not studied by Khan et al. [48 – 50]. The results over a wide range of grain size suggest an initial strengthening by the reduction of grain size, which levels off and, eventually shows, a softening response. This in turn brings about an important result that, for each metal, there exists a maximum yield strength that occurs at a grain

size that is in the nanometer range. Moreover, this critical grain size moves to the left in the Hall-Petch plot as the GBAZ becomes softer.

The novelty of the two described models is the fact that they are analytical in nature. For a nonlinear time dependent heterogeneous problem, such an analytical expression is not always attainable. But with the idealization of spherical inclusions and a transition scheme from linear viscoelastic to nonlinear creep/viscoplastic, the theory has been developed in an explicit way. The outcome is a simple model which can be easily implemented.

## **6.2 Future work**

Research on the field of nanocrystalline material is in its infancy. Large amount of opportunities are open for researchers working with this kind of nanocrystalline solids. To investigate into several properties of materials with very small grain size, a sufficiently good theoretical model has to be developed that can capture most of the features of this class of materials. Understanding the response of nanocrystalline materials under different boundary (or loading) conditions is also a challenging job. To accomplish such goals modifications can be made in the theory to simulate the exact behavior of the nanocrystalline materials. A good example is the incorporation of the grain boundary sliding within modeling procedure which is considered to have the largest amount of contribution in the grain softening (reverse Hall-Petch effect) at very small grain sizes, typically less than 10 nm.

If the grain interior of some nanocrystalline material shows different properties for different grains, the two phase composite model can be modified to three or more phases of material to account for the different properties of the grain interior. In this work the shape of the grain is considered to be equi-axial and idealized as spherical. This assumption can be relaxed and composite models for ellipsoidal shaped grains can be developed. Even the grain size in nanocrystalline material is not constant. Modification in the theory can be made to incorporate the

grain size distribution. Much work has not been done with the failure of nanocrystalline materials. Modeling the crack propagation and fracture for this type of material can always be an important challenge. Phase transformation related problems (e.g. nanocrystalline shape memory alloy) can also be solved in the future as a continuation to this line of study.

## Appendix

In this appendix, we give the constants that appear in eqs. (4.22a and 4.22b) in A1, the explicit form of the four partial derivatives in the field fluctuation approach in A2, and the procedure to calculate the evolution of creep strain of the grain interior in A3.

### A1. Constants in Eq. (4.22)

For the hydrostatic viscosity, we have

$$\frac{1}{\eta_{\kappa}^s(t)} = \frac{1}{\kappa_0} \cdot \frac{y_3 b_1}{y_1^2} \left[ \exp\left(-\frac{y_2}{y_1} t\right) \right], \quad (\text{A.1})$$

where

$$y_1 = c_1(3\kappa_0 + 4\mu_0)(\kappa_1 - \kappa_0) + (3\kappa_0 + 4\mu_0)\kappa_0, \quad y_2 = 3\kappa_0\kappa_1 T_0,$$

$$y_3 = 3\kappa_0 c_0(\kappa_1 - \kappa_0) + (3\kappa_0 + 4\mu_0)\kappa_0, \quad y_4 = 3\kappa_0 T_0(c_0(\kappa_1 - \kappa_0) + \kappa_0),$$

$$b_1 = \frac{[c_1(3\kappa_0 + 4\mu_0)(\kappa_1 - \kappa_0) + (3\kappa_0 + 4\mu_0)\kappa_0][3\kappa_0 T_0(c_0(\kappa_1 - \kappa_0) + \kappa_0)]}{[3\kappa_0 c_0(\kappa_1 - \kappa_0) + (3\kappa_0 + 4\mu_0)\kappa_0]} - 3\kappa_0\kappa_1 T_0.$$

Note that viscosities  $\eta_1$  and  $\eta_0$  appear in  $T_1$  and  $T_0$  through  $T_r = \mu_r / \eta_r$ . Likewise for the deviatoric viscosity, we write

$$\begin{aligned} \frac{1}{\eta_{\mu}^s(t)} = \frac{1}{\mu_0} [ & D + p(-r) \exp(-rt) \left( \cos(wt) + \frac{q-r}{w} \sin(wt) \right) + \\ & + p \exp(-rt) \{ -w \sin(wt) + (q-r) \cos(wt) \} ] \end{aligned} \quad (\text{A.2})$$

with

$$D = \frac{[c_0(6\kappa_0 T_0)(\mu_1 T_0 - \mu_0 T_1) + \mu_0 T_1(15\kappa_0 T_0)] T_0}{[(c_1(15\kappa_0 T_0) + c_0(6\kappa_0 T_0))(\mu_1 T_0 - \mu_0 T_1)] + \mu_0 T_1(15\kappa_0 T_0)},$$

$$p = \frac{d_1}{d_5} - \frac{d_3 d_7 - d_4 d_6}{d_7^2}, \quad q = \frac{d_2 d_7^2 - (d_5 d_4 + d_6 d_3) d_7 + d_4 d_6^2}{d_1 d_7^2 - d_5 (d_3 d_7 - d_4 d_6)},$$

$$r = \frac{1}{2} \cdot \frac{d_6}{d_5}, \quad w = \sqrt{\frac{d_7}{d_5} - \left( \frac{1}{2} \cdot \frac{d_6}{d_5} \right)^2}.$$

Furthermore,

$$d_1 = c_0 (6\kappa_0 + 12\mu_0)(\mu_1 - \mu_0) + \mu_0 (15\kappa_0 + 20\mu_0),$$

$$\begin{aligned} d_2 = & [c_0 (6\kappa_0 + 12\mu_0)(\mu_1 - \mu_0) + \mu_0 (15\kappa_0 + 20\mu_0)] T_0 + \\ & + c_0 [(6\kappa_0 T_0)(\mu_1 - \mu_0) + (\mu_1 T_0 - \mu_0 T_1)(6\kappa_0 + 12\mu_0)] + \\ & + \mu_0 ((15\kappa_0 + 20\mu_0) T_1 + (15\kappa_0 T_0)) \end{aligned}$$

$$\begin{aligned} d_3 = & \{c_0 [(6\kappa_0 T_0)(\mu_1 - \mu_0) + (\mu_1 T_0 - \mu_0 T_1)(6\kappa_0 + 12\mu_0)] + \\ & + \mu_0 ((15\kappa_0 + 20\mu_0) T_1 + (15\kappa_0 T_0))\} T_0 + \\ & + [c_0 (6\kappa_0 T_0)(\mu_1 T_0 - \mu_0 T_1) + \mu_0 T_1 (15\kappa_0 T_0)] \end{aligned}$$

$$d_4 = [c_0 (6\kappa_0 T_0)(\mu_1 T_0 - \mu_0 T_1) + \mu_0 T_1 (15\kappa_0 T_0)] T_0$$

$$d_5 = c_1 (\mu_1 - \mu_0) (15\kappa_0 + 20\mu_0) + c_0 (6\kappa_0 + 12\mu_0)(\mu_1 - \mu_0) + \mu_0 (15\kappa_0 + 20\mu_0)$$

$$\begin{aligned} d_6 = & c_0 [(6\kappa_0 T_0)(\mu_1 - \mu_0) + (\mu_1 T_0 - \mu_0 T_1)(6\kappa_0 + 12\mu_0)] + [\mu_0 ((15\kappa_0 + 20\mu_0) T_1 + \\ & + (15\kappa_0 T_0))] + c_1 [(\mu_1 T_0 - \mu_0 T_1)(15\kappa_0 + 20\mu_0) + (15\kappa_0 T_0)(\mu_1 - \mu_0)] \end{aligned}$$

$$d_7 = [c_1 (\mu_1 T_0 - \mu_0 T_1)(15\kappa_0 T_0)] + [c_0 (6\kappa_0 T_0)(\mu_1 T_0 - \mu_0 T_1) + \mu_0 T_1 (15\kappa_0 T_0)].$$

## A2. Evaluation of the four partial derivatives in the field fluctuation approach

From the field fluctuation theory the effective stress of an individual phase is given by

$$\sigma_e^{(r)2} = \frac{\mu_r}{c_r} \left[ \frac{\partial}{\partial T_r} \left( \frac{1}{\eta_\mu} \right) \bar{\sigma}_e^2 + \frac{\partial}{\partial T_r} \left( \frac{1}{\eta_\kappa} \right) \frac{\bar{\sigma}_{kk}^2}{3} \right].$$

For the hydrostatic derivatives, we have

$$\frac{\partial}{\partial T_1} \left( \frac{1}{\eta_\kappa} \right) = 0. \quad (\text{A.3})$$

$$\frac{\partial}{\partial T_0} \left( \frac{1}{\eta_\kappa} \right) = \frac{1}{\kappa_0} \left\{ \left( \frac{y_3}{y_1^2} \cdot \frac{\partial b_1}{\partial T_0} \exp \left( -\frac{y_2 t}{y_1} \right) \right) - \left( \left( \frac{y_3 d_1 t}{y_1^3} \right) \cdot \frac{\partial y_2}{\partial T_0} \cdot \exp \left( -\frac{y_2 t}{y_1} \right) \right) \right\}, \quad (\text{A.4})$$

where

$$\partial y_2 / \partial T_0 = 3\kappa_0 \kappa_1, \quad \partial y_4 / \partial T_0 = 3\kappa_0 [\kappa_0 + c_0 (\kappa_1 - \kappa_0)], \quad \partial b_1 / \partial T_0 = (y_1 / y_3) \cdot (\partial y_4 / \partial T_0) - \partial y_2 / \partial T_0.$$

For the deviatoric derivatives, we find

$$\begin{aligned} \frac{\partial}{\partial T_j} \left( \frac{1}{\eta_\mu} \right) &= \frac{1}{\mu_0} \left\{ \frac{\partial X_2}{\partial T_j} - \frac{\partial p}{\partial T_j} r \exp(-rt) [\cos(wt) + \frac{q-r}{w} \sin(wt)] - \right. \\ &\quad - p \frac{\partial r}{\partial T_j} \exp(-rt) [\cos(wt) + \frac{q-r}{w} \sin(wt)] - pr \exp(-rt) [-t \frac{\partial w}{\partial T_j} \sin(wt) + \\ &\quad + \frac{w \frac{\partial(q-r)}{\partial T_j} - (q-r) \frac{\partial w}{\partial T_j}}{w^2} \sin(wt) + \frac{q-r}{w} t \frac{\partial w}{\partial T_j} \cos(wt)] + \\ &\quad + prt \exp(-rt) \frac{\partial r}{\partial T_j} [\cos(wt) + \frac{q-r}{w} \sin(wt)] + \\ &\quad + \frac{\partial p}{\partial T_j} \exp(-rt) [-w \sin(wt) + (q-r) \cos(wt)] - \\ &\quad \left. - pt \frac{\partial r}{\partial T_j} \exp(-rt) [-w \sin(wt) + (q-r) \cos(wt)] + \right\} \end{aligned}$$

$$\begin{aligned}
& + p \exp(-rt) \left[ -\frac{\partial w}{\partial T_j} \sin(wt) - wt \frac{\partial w}{\partial T_j} \cos(wt) + \right. \\
& \left. + \frac{\partial(q-r)}{\partial T_j} \cos(wt) - (q-r)t \frac{\partial w}{\partial T_j} \sin(wt) \right] \}, \tag{A.5}
\end{aligned}$$

with  $j = 1, 2$ , and

$$\begin{aligned}
\frac{\partial X_2}{\partial T_j} &= \frac{d_7 \frac{\partial d_4}{\partial T_j} - d_4 \frac{\partial d_7}{\partial T_j}}{d_7^2}, \quad \frac{\partial p}{\partial T_j} = -\frac{d_7 \frac{\partial}{\partial T_j} (d_3 - X_2 d_6) - (d_3 - X_2 d_6) \frac{\partial d_7}{\partial T_j}}{d_7^2}, \\
\frac{\partial q}{\partial T_j} &= \frac{\left( d_1 - d_5 \cdot \frac{d_3 d_7 - d_4 d_6}{d_7^2} \right) \left[ \frac{\partial d_2}{\partial T_j} - d_5 \frac{\partial X_2}{\partial T_j} - \left( \frac{d_3 d_7 - d_4 d_6}{d_7^2} \right) \frac{\partial d_6}{\partial T_j} + d_6 \frac{\partial p}{\partial T_j} \right] - \left[ \left( d_2 - d_5 \cdot \frac{d_4}{d_7} - d_6 \cdot \frac{d_3 d_7 - d_4 d_6}{d_7^2} \right) d_5 \frac{\partial p}{\partial T_j} \right]}{\left( d_1 - d_5 \cdot \frac{d_3 d_7 - d_4 d_6}{d_7^2} \right)^2},
\end{aligned}$$

$$\frac{\partial r}{\partial T_j} = \frac{1}{2d_5} \cdot \frac{\partial d_6}{\partial T_j}, \quad \frac{\partial w}{\partial T_j} = \frac{1}{2w} \left[ \frac{1}{d_5} \cdot \frac{\partial d_7}{\partial T_j} - \frac{d_6}{2d_5^2} \frac{\partial d_6}{\partial T_j} \right],$$

also with  $j = 1, 2$ , and  $d_1, d_2 \dots d_7$  are taken from Appendix A1. The derivatives of these  $d_i$ 's

with respect to  $T_0$  are

$$\frac{\partial d_1}{\partial T_0} = \frac{\partial d_5}{\partial T_0} = 0,$$

$$\begin{aligned}
\frac{\partial d_2}{\partial T_0} &= c_0(6\kappa_0 + 12\mu_0)(\mu_1 - \mu_0) + \mu_0(15\kappa_0 + 20\mu_0) + \\
&+ 6\kappa_0 c_0(\mu_1 - \mu_0) + c_0 \mu_1(6\kappa_0 + 12\mu_0) + 15\kappa_0 \mu_0
\end{aligned}$$

$$\begin{aligned}\frac{\partial d_3}{\partial T_0} = & c_0[(6\kappa_0 T_0)(\mu_1 - \mu_0) + (\mu_1 T_0 - \mu_0 T_1)(6\kappa_0 + 12\mu_0)] + \\ & + [\mu_0((15\kappa_0 + 20\mu_0)T_1 + (15\kappa_0 T_0))] + \\ & + T_0[6\kappa_0 c_0(\mu_1 - \mu_0) + c_0(6\kappa_0 + 12\mu_0)\mu_1 + 15\kappa_0 \mu_0] + \\ & + 6\kappa_0 c_0(\mu_1 T_0 - \mu_0 T_1) + 6\kappa_0 c_0 T_0 \mu_1 + 15\kappa_0 \mu_0 T_1\end{aligned}$$

$$\begin{aligned}\frac{\partial d_4}{\partial T_0} = & c_0(6\kappa_0 T_0)(\mu_1 T_0 - \mu_0 T_1) + \mu_0 T_1(15\kappa_0 T_0) + \\ & + T_0[12c_0 \kappa_0 T_0 \mu_1 + 15\kappa_0 \mu_0 T_1 - 6c_0 \kappa_0 \mu_0 T_1]\end{aligned}$$

$$\begin{aligned}\frac{\partial d_6}{\partial T_0} = & 6\kappa_0 c_0(\mu_1 - \mu_0) + c_0(6\kappa_0 + 12\mu_0)\mu_1 + 15\kappa_0 \mu_0 + \\ & + c_1 \mu_1(15\kappa_0 + 20\mu_0) + 15\kappa_0(\mu_1 - \mu_0)\end{aligned}$$

$$\frac{\partial d_7}{\partial T_0} = 30c_1 \kappa_0 T_0 \mu_1 + 12\kappa_0 \mu_1 T_0 c_0 + 9c_0 \kappa_0 \mu_0 T_1.$$

With respect to  $T_1$  we have

$$\frac{\partial d_1}{\partial T_1} = \frac{\partial d_5}{\partial T_1} = 0,$$

$$\frac{\partial d_2}{\partial T_1} = \mu_0[(15\kappa_0 + 20\mu_0) - c_0(6\kappa_0 + 12\mu_0)],$$

$$\frac{\partial d_3}{\partial T_1} = T_0 \mu_0[(15\kappa_0 + 20\mu_0) - c_0(6\kappa_0 + 12\mu_0)] + \mu_0[(15\kappa_0 T_0) - c_0(6\kappa_0 T_0)],$$

$$\frac{\partial d_4}{\partial T_1} = T_0[(15\kappa_0 T_0) - c_0(6\kappa_0 T_0)]\mu_0,$$

$$\frac{\partial d_6}{\partial T_1} = c_0 \mu_0(9\kappa_0 + 8\mu_0),$$

$$\frac{\partial d_7}{\partial T_1} = 9c_0\kappa_0\mu_0T_0.$$

### A3. Creep strain evolution for the grain interior $\bar{\varepsilon}_{ij}^{(1)}(t)$

We compute the total strain of the grain interior through its deviatoric and dilatational components as

$$\bar{\varepsilon}_{ij}^{(1)} = \bar{\varepsilon}_{ij}'^{(1)} + \frac{1}{3}\bar{\varepsilon}_{kk}^{(1)}. \quad (\text{A.6})$$

In the elastic context, these components under an external stress  $\bar{\sigma}_{ij}$  follow from Eq. (4.13).

Through the Laplace transform and inversion, it can be shown that

$$\bar{\varepsilon}_{kk}^{(1)}(t) = \frac{1}{3\kappa_1} \left[ 1 + \frac{4c_0\mu_0(\kappa_1 - \kappa_0)}{x_1} \exp\left(-\frac{3\kappa_1\kappa_0T_0}{x_1}t\right) \right] \bar{\sigma}_{kk},$$

where  $x_1 = 3c_0\kappa_0(\kappa_1 - \kappa_0) + (3\kappa_0 + 4\mu_0)(c_1\kappa_1 + c_0\kappa_0)$ . At  $t = 0$ , it represents the initial elastic strain of the inclusions. To cast this in the incremental form for the continuous change of secant viscosity (i.e.  $T_0$  to be replaced by  $T_0^s$ ), we have

$$\dot{\bar{\varepsilon}}_{kk}^{(1)}(t) = -\frac{1}{3\kappa_1} \left[ \frac{12c_0\kappa_1\kappa_0\mu_0T_0(\kappa_1 - \kappa_0)}{x_1^2} \cdot \exp\left(-\frac{3\kappa_1\kappa_0T_0}{x_1}t\right) \right] \bar{\sigma}_{kk}. \quad (\text{A.7})$$

This rate is positive if  $\kappa_1 < \kappa_0$  (for voids it leads to creep cavitation), but is negative if  $\kappa_1 > \kappa_0$  due to the matrix constraint. For the deviatoric part, we have

$$\bar{\varepsilon}_{ij}'^{(1)}(t) = \frac{1}{2} \left[ P + Qt + p \exp(-rt) \left( \cos(wt) + \frac{q-r}{w} \sin(wt) \right) \right] \bar{\sigma}_{ij}',$$

and this results in the rate

$$\dot{\bar{\varepsilon}}_{ij}^{(1)}(t) = \frac{1}{2} \left\{ Q + p \exp(-rt) \left[ -r \left( \cos(wt) + \frac{q-r}{w} \sin(wt) \right) + (-w \sin(wt) + (q-r) \cos(wt)) \right] \right\} \bar{\sigma}_{ij}',$$

(A.8)

this is always positive, where

$$P = (y_3 y_7 - y_4 y_6) / y_7^2, \quad Q = y_4 / y_7, \quad p = y_1 / y_5 - P,$$

$$q = (y_7 y_2 - y_3 y_5) / (y_3 y_7 - y_4 y_6) - y_6 / y_7, \quad r = (1/2) \cdot y_6 / y_5, \quad w = (y_7 / y_5 - r^2)^{1/2}.$$

In addition

$$y_1 = 15\kappa_0 + 20\mu_0,$$

$$y_2 = (T_1 + T_0)(15\kappa_0 + 20\mu_0) + 15\kappa_0 T_0,$$

$$y_3 = (T_1 + T_0)(15\kappa_0 T_0) + (T_1 T_0)(15\kappa_0 + 20\mu_0),$$

$$y_4 = (T_1 T_0)(15\kappa_0 T_0),$$

$$y_5 = (\mu_1 - \mu_0)[c_1(15\kappa_0 + 20\mu_0) + c_0(6\kappa_0 + 12\mu_0)] + \mu_0(15\kappa_0 + 20\mu_0),$$

$$y_6 = (\mu_1 - \mu_0)[c_1(15\kappa_0 T_0) + c_0(6\kappa_0 T_0)] + [c_1(15\kappa_0 + 20\mu_0) + c_0(6\kappa_0 + 12\mu_0)] \cdot (\mu_1 T_0 - \mu_0 T_1) + \mu_0[(15\kappa_0 + 20\mu_0)T_1 + 15\kappa_0 T_0]$$

$$y_7 = [c_1(15\kappa_0 T_0) + c_0(6\kappa_0 T_0)](\mu_1 T_0 - \mu_0 T_1) + \mu_0(15\kappa_0 T_0)T_1.$$

In the second part of the appendix, the detailed derivation of the Eq. (5.21) is outlined in A4. The explicit derivation of the partial derivatives involved in Eq. (5.27) is described in A5. The detailed derivation and the constants involved in Eq. (5.32) are given in A6.

#### A4. Derivation of the effective secant viscosities $\eta_\kappa$ and $\eta_\mu$

The hydrostatic and deviatoric viscosities of the 3-phase porous medium in the transformed domain (Laplace domain) are given as,

$$\begin{aligned}\kappa^{TD} &= \kappa_0 \left\{ 1 + \frac{[(c_1 + c_2)\alpha_0^{TD} - c_1](\kappa_1 - \kappa_0) + c_2\kappa_0}{[(1 - c_2)\alpha_0^{TD} - 1]\kappa_0 + (\kappa_1 - \kappa_0)[c_0(\alpha_0^{TD})^2 - (1 - c_1)\alpha_0^{TD}]} \right\}, \\ \mu^{TD} &= \mu_0^{TD} \left\{ 1 + \frac{[(c_1 + c_2)\beta_0^{TD} - c_1](\mu_1^{TD} - \mu_0^{TD}) + c_2\mu_0^{TD}}{[(1 - c_2)\beta_0^{TD} - 1]\mu_0^{TD} + (\mu_1^{TD} - \mu_0^{TD})[c_0(\beta_0^{TD})^2 - (1 - c_1)\beta_0^{TD}]} \right\}.\end{aligned}\quad (\text{A.9})$$

To express  $\kappa^{TD}$  and  $\mu^{TD}$  in terms of the Laplace parameter  $s$ , we note that  $\alpha_0^{TD}$ ,  $\beta_0^{TD}$ ,  $\mu_0^{TD}$  and  $\mu_1^{TD}$  can be written as

$$\alpha_0^{TD} = \frac{3\kappa_0}{3\kappa_0 + 4\mu_0 s / (T_0 + s)} = \frac{as + b}{cs + b}, \quad \beta_0^{TD} = \frac{6\kappa_0 + 12\mu_0^{TD}}{15\kappa_0 + 20\mu_0^{TD}} = \frac{es + f}{gs + h},$$

where  $a = 3\kappa_0$ ,  $b = 3\kappa_0 T_0$ ,  $c = 3\kappa_0 + 4\mu_0$ ,  $e = 6\kappa_0 + 12\mu_0$ ,  $f = 6\kappa_0 T_0$ ,  $g = 15\kappa_0 + 20\mu_0$ , and

$h = 15\kappa_0 T_0$ . Some other parameters can be combined as

$$(c_1 + c_2)\alpha_0^{TD} - c_1 = \frac{u_1 s + u_2}{cs + b}, \text{ where } u_1 = a(c_1 + c_2) - cc_1, u_2 = bc_2;$$

$$(1 - c_2)\alpha_0^{TD} - 1 = \frac{u_3 s + u_4}{cs + b}, \text{ where } u_3 = a(1 - c_2) - c, u_4 = -bc_2;$$

$$c_0(\alpha_0^{TD})^2 - (1 - c_1)\alpha_0^{TD} = \frac{u_5 s^2 + u_6 s + u_7}{(cs + b)^2},$$

where  $u_5 = a(c_0a - (1 - c_1)c)$ ,  $u_6 = b(c_0a - (1 - c_1)c) - abc_2$ ,  $u_7 = -b^2c_2$ ;

$$(c_1 + c_2)\beta_0^{TD} - c_1 = \frac{y_1s + y_2}{gs + h}, \text{ where } y_1 = e(c_1 + c_2) - c_1g, \ y_2 = f(c_1 + c_2) - c_1h;$$

$$(1 - c_2)\beta_0^{TD} - 1 = \frac{y_3s + y_4}{gs + h}, \text{ where } y_3 = e(1 - c_2) - g, \ y_4 = f(1 - c_2) - h;$$

$$c_0(\beta_0^{TD})^2 - (1 - c_1)\beta_0^{TD} = \frac{y_5s^2 + y_6s + y_7}{(gs + h)^2},$$

where  $y_5 = c_0e^2 - (1 - c_1)eg$ ,  $y_6 = 2efc_0 - (1 - c_1)(eh + fg)$ ,  $y_7 = c_0f^2 - (1 - c_1)fh$ .

The effective hydrostatic and deviatoric stress-strain rate relations in the transformed domain under a constant strain-rate loading are derived from

$$\hat{\hat{\sigma}}_{kk} = 3\kappa^{TD} \hat{\hat{\varepsilon}}_{kk} = 3\kappa^{TD} \frac{\dot{\hat{\varepsilon}}_{kk}}{s^2}, \quad \hat{\hat{\sigma}}_{ij} = 2\mu^{TD} \hat{\hat{\varepsilon}}_{ij} = 2\frac{\mu^{TD}}{s^2} \dot{\hat{\varepsilon}}_{ij}. \quad (\text{A.10})$$

It follows from (A.9) that

$$\frac{\kappa^{TD}}{s^2} = \kappa_0 \left[ \frac{1}{s^2} + \frac{B_1s^2 + B_2s + B_3}{(B_4s^2 + B_5s + B_6)s^2} \right],$$

$$\frac{\mu^{TD}}{s^2} = \mu_0 \left[ \frac{1}{s(T_0 + s)} + \frac{(x_1s^3 + x_2s^2 + x_3s + x_4)}{s(T_0 + s)(x_5s^3 + x_6s^2 + x_7s + x_8)} \right], \quad (\text{A.11})$$

where

$$B_1 = c_2\kappa_0c^2 + (\kappa_1 - \kappa_0)u_1c,$$

$$B_2 = 2cbc_2\kappa_0 + (\kappa_1 - \kappa_0)(u_1b + u_2c),$$

$$B_3 = c_2 \kappa_0 b^2 + (\kappa_1 - \kappa_0) u_2 b,$$

$$B_4 = \kappa_0 u_3 c + (\kappa_1 - \kappa_0) u_5,$$

$$B_5 = \kappa_0 (u_3 b + u_4 c) + (\kappa_1 - \kappa_0) u_6,$$

$$B_6 = \kappa_0 u_4 b + (\kappa_1 - \kappa_0) u_7,$$

$$x = \mu_1 T_0 - \mu_0 T_1,$$

$$y = \mu_1 - \mu_0,$$

$$x_1 = c_2 \mu_0 g^2 + yy_1 g,$$

$$x_2 = c_2 \mu_0 (2gh + T_1 g^2) + y(y_2 g + y_1 h) + xy_1 g,$$

$$x_3 = c_2 \mu_0 (2ghT_1 + h^2) + yy_2 h + x(y_2 g + y_1 h),$$

$$x_4 = c_2 \mu_0 T_1 h^2 + xy_2 h,$$

$$x_5 = \mu_0 y_3 g + yy_5,$$

$$x_6 = \mu_0 (y_3 g T_1 + y_3 h + y_4 g) + yy_6 + xy_5,$$

$$x_7 = \mu_0 [(y_3 h + y_4 g) T_1 + y_4 h] + yy_7 + xy_6,$$

$$x_8 = \mu_0 T_1 y_4 h + xy_7.$$

Since  $\eta_\kappa = L^{-1}(\kappa^{TD} / s^2)$ , we have

$$\eta_\kappa = \kappa_0 \left\{ t + L^{-1} \left[ \frac{B_1 s^2 + B_2 s + B_3}{(B_4 s^2 + B_5 s + B_6) s^2} \right] \right\}.$$

After carrying out the Laplace inverse, we have

$$\eta_\kappa = \kappa_0 \left\{ A + p e^{-rt} \left[ \cos(wt) + \frac{q-r}{w} \sin(wt) \right] \right\}, \quad (\text{A.12})$$

where

$$A = \frac{B_2 + B_5}{B_6}, p = \frac{C}{B_4}, q = \frac{D}{C}, r = \frac{1}{2} \frac{B_5}{B_4}, w = \sqrt{\frac{B_6}{B_4} - \frac{1}{4} \frac{B_5^2}{B_4^2}};$$

$$C = -AB_4, D = B_1 + B_4 - AB_5.$$

Likewise from  $\eta_\mu = L^{-1}(\mu^{TD} / s^2)$ , the deviatoric term can be cast into

$$\eta_\mu = \eta_0 (1 - e^{-T_0 t}) + L^{-1} \left[ \frac{\gamma}{s} + \frac{\delta}{T_0 + s} + \frac{D_1 s^2 + D_2 s + D_3}{x_5 s^3 + x_6 s^2 + x_7 s + x_8} \right],$$

where  $\gamma = (x_4 / x_8) \eta_0$ ,  $\delta = (\varphi_1 - D_1) / x_5$ ,  $D_1 = \frac{\psi_1}{\psi_2}$ ,  $D_2 = \varphi_2 - \frac{x_6}{x_5} \varphi_1 + D_1 \left( \frac{x_6}{x_5} - T_0 \right)$ ,

$$D_3 = \frac{1}{T_0} \left[ \varphi_4 - \frac{x_8}{x_5} (\varphi_1 - D_1) \right],$$

with

$$\varphi_1 = -\gamma x_5, \varphi_2 = \mu_0 x_1 - \gamma (x_5 T_0 + x_6), \varphi_3 = \mu_0 x_2 - \gamma (x_6 T_0 + x_7), \varphi_4 = \mu_0 x_3 - \gamma (x_7 T_0 + x_8),$$

$$\psi_1 = \varphi_3 - \frac{x_7}{x_5} \varphi_1 - T_0 \left( \varphi_2 - \frac{x_6}{x_5} \varphi_1 \right) - \frac{\varphi_4}{T_0} + \frac{1}{T_0} \frac{x_8}{x_5} \varphi_1, \psi_2 = \frac{1}{T_0} \frac{x_8}{x_5} - \frac{x_7}{x_5} + T_0 \left( \frac{x_6}{x_5} - T_0 \right).$$

The final expression for the effective deviatoric viscosity in the time domain is

$$\eta_\mu = \left(1 + \frac{x_4}{x_8}\right) \eta_0 - (\eta_0 - \delta) e^{-T_0 t} + E \left\{ F_1 e^{\lambda_1 t} + e^{a_1 t} \left[ (F_2 + F_3) \cos(b_1 t) + (F_2 - F_3) \sin(b_1 t) \right] \right\}, \quad (\text{A.13})$$

where

$$F_1 = \frac{(\lambda_1)^2 + \lambda_1 E_1 + E_2}{(\lambda_1 - \lambda_2)(\lambda_1 - \lambda_3)}, \quad F_2 = \frac{(\lambda_2)^2 + \lambda_2 E_1 + E_2}{(\lambda_2 - \lambda_1)(\lambda_2 - \lambda_3)}, \quad F_3 = \frac{(\lambda_3)^2 + \lambda_3 E_1 + E_2}{(\lambda_3 - \lambda_1)(\lambda_3 - \lambda_2)},$$

and

$$\lambda_1 = t_1 + t_2 - \frac{b}{3}, \quad \lambda_2 = a_1 + ib_1, \quad \lambda_3 = a_1 - ib_1; \quad a_1 = -\frac{1}{2}(t_1 + t_2) - \frac{b}{3}, \quad b_1 = \frac{\sqrt{3}}{2}(t_1 - t_2),$$

with

$$t_1 = \sqrt[3]{q_1 + r_1}, \quad t_2 = \sqrt[3]{q_1 - r_1}, \quad q_1 = \frac{9E_3 E_4 - 27E_5 - 2(E_3)^3}{54}, \quad r_1 = \sqrt{\left(\frac{3E_4 - (E_3)^2}{9}\right)^3 + q^2}.$$

Furthermore,

$$E = \frac{D_1}{x_5}, \quad E_1 = \frac{D_2}{D_1}, \quad E_2 = \frac{D_3}{D_1}, \quad E_3 = \frac{x_6}{x_5}, \quad E_4 = \frac{x_7}{x_5}, \quad E_5 = \frac{x_8}{x_5}.$$

This completes the expressions of  $\eta_\kappa$  and  $\eta_\mu$  in Eq. (5.21).

## A5. Evaluation of the four partial derivatives in the field fluctuation approach

To use these viscosities in the field fluctuation theory, their derivatives with respect to the constituent shear viscosity have to be obtained. We shall first consider the hydrostatic derivatives and then the deviatoric ones.

i) *The  $\partial\eta_\kappa / \partial\eta_0$  term:*

$$\frac{\partial \eta_\kappa}{\partial \eta_0} = \kappa_0 \left\{ \frac{\partial A}{\partial \eta_0} + \frac{\partial}{\partial \eta_0} \left[ p e^{-\pi} \left( \cos(wt) + \frac{q-r}{w} \sin(wt) \right) \right] \right\}, \quad (\text{A.14})$$

where

$$\frac{\partial A}{\partial \eta_0} = \frac{4}{3} \frac{1-c_2}{\kappa_0 c_2};$$

$$\frac{\partial}{\partial \eta_0} \left[ p e^{-\pi} \left( \cos(wt) + \frac{q-r}{w} \sin(wt) \right) \right] =$$

$$\frac{\partial p}{\partial \eta_0} e^{-\pi} \left[ \cos(wt) + \frac{q-r}{w} \sin(wt) \right] - p t e^{-\pi} \frac{\partial r}{\partial \eta_0} \left[ \cos(wt) + \frac{q-r}{w} \sin(wt) \right] +$$

$$p e^{-\pi} \left[ -t \frac{\partial w}{\partial \eta_0} \sin(wt) + \left( w \frac{\partial(q-r)}{\partial \eta_0} - (q-r) \frac{\partial w}{\partial \eta_0} \right) \cdot \frac{1}{w^2} \cdot \sin(wt) + \frac{q-r}{w} t \frac{\partial w}{\partial \eta_0} \cos(wt) \right],$$

with

$$\frac{\partial p}{\partial \eta_0} = -\frac{\partial A}{\partial \eta_0}; \quad \frac{\partial r}{\partial \eta_0} = -\frac{3 \kappa_0^2 [-4\mu_0 - 2c_5(3\kappa_0 + 2\mu_0)]}{2 B_4} \cdot \frac{\mu_0}{(\eta_0)^2};$$

$$\frac{\partial w}{\partial \eta_0} = -\frac{\mu_0}{(\eta_0)^2} \cdot \sqrt{\frac{\bar{B}_6}{B_4} - \frac{1}{4} \frac{\bar{B}_5^2}{B_4^2}}, \quad \bar{B}_6 = -9\kappa_0^3 c_2, \quad \bar{B}_5 = 3\kappa_0^2 [-4\mu_0 - 2c_2(3\kappa_0 + 2\mu_0)];$$

$$\frac{\partial q}{\partial \eta_0} = \bar{A} \left( \frac{\mu_0}{(\eta_0)^2} \right), \quad \bar{A} = \frac{3Dc_2\kappa_0}{4\mu_0 B_4(1-c_2)}, \quad \frac{\partial(q-r)}{\partial \eta_0} = \frac{\partial q}{\partial \eta_0} - \frac{\partial r}{\partial \eta_0}.$$

ii) The  $\partial \eta_\kappa / \partial \eta_1$  term:

$$\frac{\partial \eta_\kappa}{\partial \eta_1^s} = 0, \text{ for } \eta_\kappa \neq \eta_\kappa(\eta_1). \quad (\text{A.15})$$

iii) The  $\partial\eta_\mu / \partial\eta_0$  term:

For this derivative, we write

$$\begin{aligned}
\frac{\partial\eta_\mu}{\partial\eta_0} = & 1 + \frac{x_4}{x_8} + \eta_0 \cdot \left[ x_8 \cdot \frac{\partial x_4}{\partial\eta_0} - x_4 \cdot \frac{\partial x_8}{\partial\eta_0} \right] \frac{1}{(x_8)^2} - \left[ 1 - \frac{\partial\delta}{\partial\eta_0} \right] e^{-T_0 t} - (\eta_0 - \delta) t e^{-T_0 t} \frac{\mu_0}{(\eta_0)^2} + \\
& + \frac{\partial E}{\partial\eta_0} \{ F_1 e^{\lambda_1 t} + e^{a_1 t} [(F_2 + F_3) \cos(b_1 t) + (F_2 - F_3) \sin(b_1 t)] \} + E \left\{ \frac{\partial F_1}{\partial\eta_0} e^{\lambda_1 t} + \right. \\
& + F_1 t e^{\lambda_1 t} \frac{\partial\lambda_1}{\partial\eta_0} + t e^{a_1 t} \frac{\partial a_1}{\partial\eta_0} [(F_2 + F_3) \cos(b_1 t) + (F_2 - F_3) \sin(b_1 t)] + e^{a_1 t} \left[ \left( \frac{\partial F_2}{\partial\eta_0} + \right. \right. \\
& + \left. \left. \frac{\partial F_3}{\partial\eta_0} \right) \cos(b_1 t) - (F_2 + F_3) t \frac{\partial b_1}{\partial\eta_0} \sin(b_1 t) + \left( \frac{\partial F_2}{\partial\eta_0} - \frac{\partial F_3}{\partial\eta_0} \right) \sin(b_1 t) + \right. \\
& \left. \left. + (F_2 - F_3) t \frac{\partial b_1}{\partial\eta_0} \cos(b_1 t) \right] \right\}, \tag{A.16}
\end{aligned}$$

where

$$\begin{aligned}
\frac{\partial x_4}{\partial\eta_0} = & - \frac{\mu_0}{(\eta_0)^2} \{ 450 c_2 \mu_0 T_0 T_1 \kappa_0^2 + 15 \kappa_0^2 \mu_1 [6 T_0^2 (c_1 + c_2) - 15 T_0^2 c_1] + \\
& + 15 \kappa_0^2 (\mu_1 T_0 - \mu_0 T_1) T_0 [12 (c_1 + c_2) - 30 c_1] \}, \\
\frac{\partial x_8}{\partial\eta_0} = & - \frac{\mu_0}{(\eta_0)^2} \{ 15 \kappa_0^2 T_1 T_0 [12 (1 - c_2) - 30] + \mu_1 \kappa_0^2 T_0^2 [36 c_0 - 90 (1 - c_1)] + \\
& + (\mu_1 T_0 - \mu_0 T_1) \kappa_0^2 T_0 [72 c_0 - 180 (1 - c_1)] \}.
\end{aligned}$$

The remaining terms are evaluated numerically as

$$\frac{\partial(*)}{\partial\eta_0} = \frac{(*) (t-1) - (*) (t-2)}{\eta_0 (t-1) - \eta_0 (t-2)}.$$

iv) The  $\partial\eta_\mu / \partial\eta_1$  term:

For this term we write

$$\frac{\partial\eta_\mu}{\partial\eta_1} = \eta_0 \cdot \left( x_8 \cdot \frac{\partial x_4}{\partial\eta_1} - x_4 \cdot \frac{\partial x_8}{\partial\eta_1} \right) \frac{1}{(x_8)^2} + \frac{\partial\delta}{\partial\eta_1} e^{-T_0 t} + \frac{\partial E}{\partial\eta_1} \{ F_1 e^{\lambda_1 t} + e^{a_1 t} [(F_2 + F_3) \cos(b_1 t) +$$

$$\begin{aligned}
& + (F_2 - F_3) \sin(b_1 t)] \} + E \left\{ \frac{\partial F_1}{\partial \eta_1} e^{\lambda_1 t} + F_1 t e^{\lambda_1 t} \frac{\partial \lambda_1}{\partial \eta_1} + t e^{a_1 t} \frac{\partial a_1}{\partial \eta_1} [(F_2 + \right. \\
& + F_3) \cos(b_1 t) + (F_2 - F_3) \sin(b_1 t)] + e^{a_1 t} [(\frac{\partial F_2}{\partial \eta_1} + \frac{\partial F_3}{\partial \eta_1}) \cos(b_1 t) - \\
& \left. - (F_2 + F_3) t \frac{\partial b_1}{\partial \eta_1} \sin(b_1 t) + (\frac{\partial F_2}{\partial \eta_1} - \frac{\partial F_3}{\partial \eta_1}) \sin(b_1 t) + (F_2 - F_3) t \frac{\partial b_1}{\partial \eta_1} \cos(b_1 t)] \right\}, \quad (\text{A.17})
\end{aligned}$$

where

$$\begin{aligned}
\frac{\partial x_4}{\partial \eta_1} &= -\frac{\mu_1}{(\eta_1)^2} (7\mu_0 h \kappa_0 T_0) (c_1 + c_2), \\
\frac{\partial x_8}{\partial \eta_1^s} &= -\frac{\mu_1}{(\eta_1)^2} (\mu_0 y_4 h - \mu_0 y_7),
\end{aligned}$$

and the remaining terms are evaluated numerically also.

#### A6. Evaluation of the porosity evolution

From Eq. (5.28),  $\dot{c}_2 = c_2 (\dot{\bar{\varepsilon}}_{kk}^{(2)} - \dot{\bar{\varepsilon}}_{kk})$ , it is evident that the key is to evaluate  $\dot{\bar{\varepsilon}}_{kk}^{(2)}$  of phase 2, the voids. In the elastic context, the dilatational strain can be written as (Weng [9])

$$\bar{\varepsilon}_{kk}^{(2)} = \frac{\kappa_0}{[\alpha_0 (\kappa_2 - \kappa_0) + \kappa_0] (1 - \alpha_0 a)} \bar{\varepsilon}_{kk}, \quad (\text{A.18})$$

where the value of  $a$  is given in (5.14). In the Laplace domain this translates into

$$\hat{\bar{\varepsilon}}_{kk}^{(2)} = \frac{\kappa_0}{[\alpha_0^{TD} (\kappa_2 - \kappa_0) + \kappa_0] (1 - \alpha_0^{TD} a^{TD})} \hat{\bar{\varepsilon}}_{kk}.$$

After casting  $\alpha_0^{TD}$  and  $a^{TD}$  in terms of the Laplace parameter  $s$ , this gives rise to

$$\hat{\bar{\varepsilon}}_{kk}^{(2)} = \frac{p_1 s^2 + p_2 s + p_3}{p_4 s^2 + p_5 s + p_6} \hat{\bar{\varepsilon}}_{kk}, \quad (\text{A.19})$$

where

$$p_1 = l_1 a_1 c_1 + l_2 c_1^2, \quad p_2 = l_1 (a_1 + c_1) b_1 + 2b_1 c_1 l_2, \quad p_3 = b_1^2 (l_1 + l_2),$$

$$p_4 = l_3 a_1^2 + l_4 a_1 c_1 + l_5 c_1^2, \quad p_5 = 2l_3 a_1 b_1 + l_4 b_1 (a_1 + c_1) + 2l_5 b_1 c_1,$$

$$p_6 = (l_3 + l_4 + l_5) b_1^2,$$

and  $l_1 = \kappa_1 - \kappa_0$ ,  $l_2 = \kappa_0$ ,  $l_3 = -c_0(\kappa_1 - \kappa_0)$ ,  $l_4 = (\kappa_1 - \kappa_0) - (c_1 \kappa_1 + c_0 \kappa_0)$ ,  $l_5 = \kappa_0 = l_2$ ;

$$a_1 = 3\kappa_0, \quad b_1 = 3\kappa_0 T_0, \quad c_1 = 3\kappa_0 + 4\mu_0.$$

Taking the Laplace inverse of (A.19), and noting that, under a constant strain-rate loading,

$\hat{\bar{\varepsilon}}_{kk} = (1/s^2) \cdot \dot{\bar{\varepsilon}}_{kk}$ , we arrive at

$$\bar{\varepsilon}_{kk}^{(2)}(t) = \left\{ A + Bt + p e^{-rt} \left( \cos wt + \frac{q-r}{w} \sin wt \right) \right\} \dot{\bar{\varepsilon}}_{kk},$$

where  $B = p_3 / p_6 = -1/(1 - c_2)$ ,  $A = (p_2 - Bp_5) / p_6$ ,  $C = -Ap_4$ ,  $D = p_1 - (Ap_5 + Bp_4)$ ,

$p = C / p_4$ ,  $q = D / C$ ,  $r = p_5 / (2p_4)$ , and  $w = (p_6 / p_4 - r^2)^{1/2}$ . In the rate form, it is

$$\dot{\bar{\varepsilon}}_{kk}^{(2)} = \left\{ B - p r e^{-rt} \left[ \cos wt + \frac{q-r}{w} \sin wt \right] + p e^{-rt} \left[ -w \sin wt + (q-r) \cos wt \right] \right\} \dot{\bar{\varepsilon}}_{kk}. \quad (\text{A.20})$$

## References

- [1] Gleiter, H., Nanostructured Materials: Basic Concepts and Microstructure. *Acta Materialia*, 48: 1-29, 2000.
- [2] Mura, T., *Micromechanics of Defects in Solids*. Martinus Nijhoff Publishers. Second, Revised Edition, 1987.
- [3] Nemat-Nasser, S., Hori, M., *Micromechanics: Overall Properties of Heterogeneous Materials*. North-Holland. Second, Revised Edition, 1999.
- [4] Qu, J., Cherkaoui, M., *Fundamentals of Micromechanics of Solids*. John Wiley and Sons Inc. 2006.
- [5] Eshelby, J. D., The determination of the elastic field of an ellipsoidal inclusion, and related problems. *Proceedings of the Royal Society of London*. A241, 376-396, 1957.
- [6] Eshelby, J. D., Elastic field outside an ellipsoidal inclusion. *Proceedings of the Royal Society of London*. A252, 561-569, 1959.
- [7] Hill, R., Continuum micromechanics of elastoplastic polycrystals. *Journal of the Mechanics and Physics of Solids*. 13, 89-101, 1965.
- [8] Hill, R., The essential structure of constitutive laws for metal composites and polycrystals. *Journal of the Mechanics and Physics of Solids*. 15, 79-95, 1967.
- [9] Hashin, Z., Viscoelastic behavior of the heterogeneous media. *Journal of Applied Mechanics*. 32, 630-636, 1965.

- [10] Weng, G. J., Some elastic properties of reinforced solids, with special reference to isotropic ones containing spherical inclusion. *Internal Journal of Engineering and Science*. 22, 845-856, 1984.
- [11] Talbot, D. R. S., Willis, J. R., Variational principles for inhomogeneous nonlinear media. *IMA Journal of Applied Mathematics*. 35, 39-54, 1985.
- [12] Hashin, Z., Shtrikman, S., A variational approach to the theory of elastic behavior of multiphase materials. *Journal of Mechanics and Physics of Solids*. 11, 127-140, 1963.
- [13] Tandon, G. P., Weng, G. J., A theory of particle reinforced plasticity. *Journal of Applied Mechanics*. 55, 126-135, 1988.
- [14] Qiu, Y. P., Weng, G. J., A theory of plasticity for porous materials and particle reinforced composites. *Journal of Applied Mechanics*. 59, 261-268, 1992.
- [15] Li, J., Weng, G. J., A secant viscosity approach to the time dependent creep of an elastic viscoplastic composite. *Journal of Mechanics and Physics of Solids*. 45, 1069-1083, 1997.
- [16] Li, J., Weng, G. J., A homogenization theory for the overall creep of isotropic viscoplastic composites. *Acta Mechanica*. 125, 141-153, 1997.
- [17] Li, J., Weng, G. J., A unified approach from elasticity to viscoelasticity to viscoplasticity of particle reinforced solids. *International Journal of Plasticity*. 14, 193-208, 1998.
- [18] Hall, E. O., The deformation and ageing of mild steel: III Discussion of results. *Proceedings of the Physical Society*. B64, 747-753, 1951.
- [19] Petch, N. J., The cleavage strength of polycrystals. *Journal of Iron and Steel Institute*. 174, 25-28, 1953.

- [20] Chokshi, A. H., Rosen, A., Karch, J., Gleiter, H., On the validity of the Hall-Petch relationship in nanocrystalline materials. *Scripta Metallurgica*. 23, 1679-1684, 1989.
- [21] Sanders, D. G., Youngdhal, C. J., Weertman, J. R., The strength of nanocrystalline metals with and without flaws. *Material Science and Engineering*. A234-A236, 77-82, 1997.
- [22] Sanders, D. G., Eastman, J. A., Weertman, J. R., Elastic and tensile behavior of nanocrystalline copper and palladium. *Acta Materialia*. 45, 4019-4025, 1997.
- [23] Schiøtz, J., Di Tolla, F. D., Jacobsen, K. W., Softening of nanocrystalline metals at very small grain sizes. *Nature*. 39, 561-563, 1998.
- [24] Lund, A. C., Schuh C. A., Strength asymmetry in nanocrystalline metals under multiaxial loading. *Acta Materialia*. 53, 3193-3205, 2005.
- [25] Carsley, J. E., Ning, J., Milligan, W. M., Hackney, S. A., Aifantis, E. C., A simple mixture based model for the grain size dependence of strength of nanophase metals. *Nanostructured Materials*. 5, 441-448, 1995.
- [26] Wang, N., Wang, Z., Aust, K. T., Erb, U., Effect of grain size on mechanical properties of nanocrystalline materials. *Acta Metallurgica et Materialia*. 43, 519-528, 1995.
- [27] Jiang, B., Weng, G. J., A composite model for the grain size dependence of yield stress of nanograined materials. *Metallurgical and Materials Transactions*. 34A, 765-772, 2003.
- [28] Jiang, B., Weng, G. J., A theory of compressive yield strength of nanograined ceramics. *International Journal of Plasticity*. 20, 2007-2026, 2004.
- [29] Jiang, B., Weng, G. J., A generalized self consistent polycrystal model for the yield strength of nanocrystalline materials. *Journal of Mechanics and Physics of Solids*. 52, 1125-1149, 2004.

- [30] Capolungo, L., Cherkaoui, M., Qiu, J., A self consistent model for the inelastic deformation of nanocrystalline materials. *Journal of Engineering and Materials Technology*. 127, 400-407, 2005.
- [31] Capolungo, L., Joachim, C., Cherkaoui, M., Qiu, J., Homogenization method for strength and inelastic behavior of nanocrystalline materials. *International Journal of Plasticity*. 21, 67-82, 2005.
- [32] Li, J., Weng, G. J., A secant-viscosity composite model for the strain rate sensitivity of nanocrystalline materials. *International Journal of Plasticity*. 23, 2115-2133, 2007.
- [33] Schwaiger, R., Moser, B., Dao, M., Chollacoop, N., Suresh, S., Some critical experiments on the strain-rate sensitivity of the nanocrystalline nickel. *Acta Materialia*. 51, 5159-5172, 2003.
- [34] Frost, H. J., Ashby, M. F., Deformation-Mechanism Maps – The Plasticity and creep of metals and ceramics. *Pergamon. Oxford*. 11, 1982.
- [35] Ashby, M. F., The deformation of plastically non-homogeneous materials. *Philosophical Magazine*. 21, 399–424 (1970).
- [36] Eshelby, J. D., Frank, F. C., Nabarro, F. R. N., The equilibrium of linear arrays of dislocations. *Philosophical Magazine*. 42, 351-364 (1951).
- [37] Christensen, R. M., Lo, K. H., Solutions for effective shear properties in three phase sphere and cylinder models. *Journal of Mechanics and Physics of Solids*. 27, 315-330, 1979.
- [38] Bobeth, M., Diener, G., Field fluctuation on multicomponent mixtures. *Journal of Mechanics and Physics of Solids*. 34, 1-17, 1986.
- [39] Kreher, W., Pompe, W., *Internal Stress in Heterogeneous solids*. Akademie. Berlin, 1989.
- [40] Suquet, P., Overall properties of nonlinear composites: a modified secant moduli theory and its link with Ponte Castaneda's nonlinear variational procedure. *C. R. Acad. Des. Sci.* 320 (Ser. Lib.), 563-571, 1995.

- [41] Hu, G. K., A method of plasticity for general aligned spheroidal void or fiber-reinforced composites. *Internal Journal of Plasticity*. 12, 439-449, 1996.
- [42] Sanders, P. G., Rittner, M., Kiedaish, E., Weertman, J. R., Kung, H., Lu, Y. C., Creep of nanocrystalline Cu, Pd, Al-Zr. *Nanostructured Material*. 9, 433-440, 1997.
- [43] Wang, D. L., Kong, Q. P., Shui, J. P., Creep of nanocrystalline Ni-P alloy. *Scripta Metallurgica et Materialia*. 31, 47-51, 1994.
- [44] Wang, N., Wang, Z., Aust, K. T., Erb, U., Room temperature creep behavior of nanocrystalline nickel produced by an electro deposition technique. *Material Science and Engineering*. A237, 150-158, 1997.
- [45] Carlton, C. E., Ferreira, P. J., What is behind the inverse Hall-Petch effect of the nanocrystalline materials? *Acta Materialia*. 55, 3749-3756, 2007.
- [46] Weng, G. J., A micromechanical theory of grain size dependence in metal plasticity. *Journal of Mechanics and Physics of Solids*. 31, 193-203, 1983.
- [47] Tan, H., Huang, Y., Liu, C., Geubelle, P. H., The Mori-Tanaka method for composite materials with nonlinear interface debonding. *International Journal of Plasticity*. 21, 1890-1918, 2005.
- [48] Khan, A. S., Zhang, H., Takacs, L., Mechanical response and modeling of fully compacted nanocrystalline iron and copper. *International Journal of Plasticity*. 16, 1459-1476, 2000.
- [49] Khan, A. S., Zhang, H., Mechanically alloyed nanocrystalline iron and copper mixture: behavior and constitutive modeling over a wide range of strain rates. *International Journal of Plasticity*. 16, 1477-1492, 2000.
- [50] Khan, A. S., Suh, Y. S., Chen, X., Takacs, L., Zhang, H., Nanocrystalline aluminum and iron: mechanical behavior at quasi static and high strain rates, and constitutive modeling. *International Journal of Plasticity*. 22, 195-209, 2006.
- [51] Kumar, K. S., Suresh, S., Chisholm, M. F., Horton, J. A., Wang, P., Deformation of electrodeposited nanocrystalline nickel. *Acta Materialia*. 51, 387-405, 2003a.
- [52] Spitzig, W. A., Smelser, R. E., Richmond, O., The evolution of damage and fracture in iron compacts with various initial porosities. *Acta Metallurgica*. 36, 1201-1211, 1988.

## Vita

### Pallab Barai

- 2007 Barai, P., Weng, G.J., 2007. The competition of grain size and porosity in the viscoplastic response of nanocrystalline solids. *International Journal of Plasticity* (2008), doi:10.1016/j.ijplas.2007.09.010 (in press).
- 2008 Barai, P., Weng, G.J., 2008. Mechanics of creep resistance in nanocrystalline solids. *Acta Mechanica*. Vol. 195, p 327-348.
- 2008 Barai, P., Weng, G. J., 2008, “The competition of grain size and porosity in the viscoplastic response of nanocrystalline solids.” presented at NSF CMMI Conference, University of Tennessee, Knoxville, TN, Jan 8 – Jan 10, 2008.
- 2002-06 B. Tech in Aerospace Engineering, Indian Institute of Technology, Kharagpur, India.
- 1998-02 Kalyani University Experimental High School, Kalyani, Nadia, India.